

Fourier-Based 3D Multistage Transformer for Aberration Correction in Multicellular Specimens

Thayer Alshaabi^{1,2*}, Daniel E. Milkie¹, Gaoxiang Liu², Cyna Shirazinejad², Jason L. Hong², Kemal Achour², Frederik Görlitz², Ana Milunovic-Jevtic², Cat Simmons², Ibrahim S. Abuzahriyeh², Erin Hong², Samara Erin Williams², Nathanael Harrison², Evan Huang², Eun Seok Bae², Alison N. Killilea², David G. Drubin², Ian A. Swinburne², Srigokul Upadhyayula^{2,3,4*}, Eric Betzig^{1,2,5,6*}

¹Howard Hughes Medical Institute, Ashburn, VA

²Department of Molecular and Cell Biology, University of California Berkeley, Berkeley, CA

³Lawrence Berkeley National Laboratory, Berkeley, CA

⁴Chan Zuckerberg Biohub, San Francisco, CA

⁵Department of Physics, University of California, Berkeley, CA

⁶Helen Wills Neuroscience Institute, Berkeley, CA

ABSTRACT

High-resolution tissue imaging is often compromised by sample-induced optical aberrations that degrade resolution and contrast. While wavefront sensor-based adaptive optics (AO) can measure these aberrations, such hardware solutions are typically complex, expensive to implement, and slow when serially mapping spatially varying aberrations across large fields of view. Here, we introduce AOVIFT (Adaptive Optical Vision Fourier Transformer)—a machine learning-based aberration sensing framework built around a 3D multistage Vision Transformer that operates on Fourier domain embeddings. AOVIFT infers aberrations and restores diffraction-limited performance in puncta-labeled specimens with substantially reduced computational cost, training time, and memory footprint compared to conventional architectures or real-space networks. We validated AOVIFT on live gene-edited zebrafish embryos, demonstrating its ability to correct spatially varying aberrations using either a deformable mirror or post-acquisition deconvolution. By eliminating the need for the guide star and wavefront sensing hardware and simplifying the experimental workflow, AOVIFT lowers technical barriers for high-resolution volumetric microscopy across diverse biological samples.

Model code. Source code for training and evaluation (and all pretrained models) are available at <https://github.com/cell-observatory/aovift>.

Synthetic data generator. Code for simulating beads is available at https://github.com/cell-observatory/beads_simulator.

Package. Docker image is available at <https://github.com/cell-observatory/aovift/pkgs/container/aovift>.

Contributions. T.A. designed models, developed training pipelines and evaluation benchmarks. D.E.M. designed the preprocessing algorithms and developed the microscope software for the imaging experiments. T.A. and D.E.M. designed Fourier embedding, and developed the synthetic data generator for training and validation. C. Shirazinejad, C. Simmons, I.S.A., S.E.W., N.H., E. Hong, E. Huang, E.S.B., A.N.K., D.G.D., and I.A.S. generated the zebrafish reagents. A.N.K., prepared the cultured SUM159 cells. C. Shirazinejad, J.L.H., K.A., and A.M.J. prepared samples. G.L. and J.L.H. performed the imaging experiments with zebrafish. J.L.H. and K.A. performed the imaging experiments with cells. G.L., K.A. and F.G. performed the imaging experiments with beads. T.A., D.E.M., and S.U. performed analysis and prepared figures. T.A. wrote the manuscript with input from all co-authors. D.E.M., E.B. and S.U. edited the manuscript. T.A., E.B. and S.U. supervised the project.

* Corresponding authors: alshaabit@hhmi.org, sup@berkeley.edu, betzige@hhmi.org.

1 INTRODUCTION

As we peer deeper into living organisms to reveal their inner workings, our view is increasingly compromised by sample-induced optical aberrations. Numerous AO methods exist to compensate for these by using a wavefront shaping device that responds to a measurement of sample-induced aberration [1]. These methods differ in their complexity, generality, robustness, and practicality. In our lab, dependable success was had using a Shack-Hartmann (SH) sensor to measure the aberrations imparted on a guide star (GS) created by two-photon excitation (TPE) fluorescence within the specimen [2], and we have used this approach extensively in adaptive optical lattice light sheet microscopy (AO-LLSM) to study four dimensional (4D) subcellular dynamic processes within the native environment of whole multicellular organisms [3].

Several recent approaches dispense with the cost and complexity of hardware-based wavefront measurement in favor of directly inferring aberrations from the microscope images themselves via machine learning (ML) [4–8] (Supplementary Table S1). Based on our experience with a variety of specimens, any ML-AO approach suitable for AO-LLSM must meet the following specifications:

Speed: To maximize the range of spatiotemporal events that can be visualized, the time for the ML model to infer the aberrations across any volume should be less than the time needed to image it—typically a few seconds in LLSM for a volume that encompasses a handful of cells.

Robustness: The model must accurately predict the vast majority of aberrations encountered in practice—for AO-LLSM in zebrafish embryos, typically up to 5λ peak-to-valley (P-V) in any combination of the first 15 Zernike modes (Z_0^0 through $Z_4^{\pm 4}$ Supplementary Fig. S1).

Accuracy: The method should be able to recover close to the theoretical 3D resolution limits of the microscope, regardless of the distribution of spatial frequencies within the specimen.

Noninvasiveness: The method should provide accurate correction without unduly depleting the fluorescence photon budget within the specimen or perturbing its native physiology.

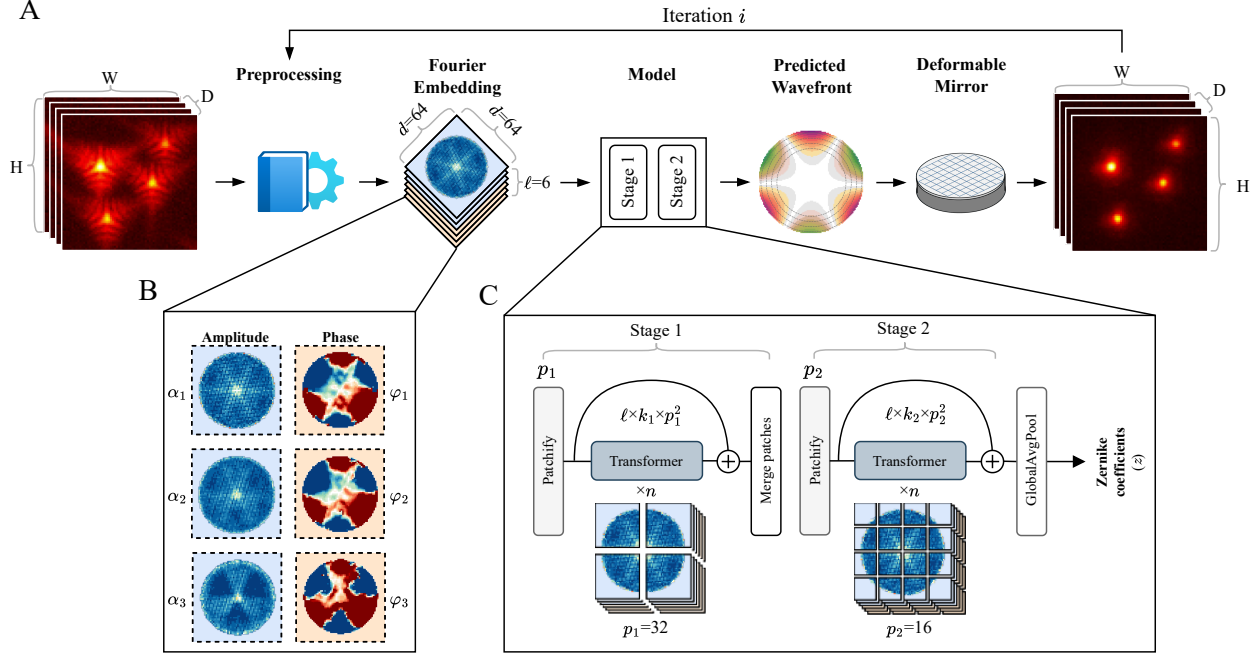


Figure 1: AOVIFT workflow. **A.** AOVIFT correction. An aberrated 3D volume is preprocessed and cast into a Fourier Embedding, which is passed to a 3D vision transformer model to predict the detection wavefront. A deformable mirror (DM) compensates for this aberration, enabling acquisition of a corrected volume. **B.** The Fourier embedding, \mathcal{E} . The Fourier Transform of the 3D volume is embedded into a lower space ($\mathcal{E} \in \mathbb{R}^{\ell \times d \times d}$), consisting of 3 amplitude planes ($\alpha_1, \alpha_2, \alpha_3$) and 3 phase planes ($\varphi_1, \varphi_2, \varphi_3$). **C.** AOVIFT model. The Fourier embedding is input to a dual-stage 3D vision transformer model. At each stage, the ℓ Fourier planes are tiled into k patches (Patchify), applying a radially encoded positional embedding to each patch. These patches are passed through n Transformer layers. At the end of each stage, a residual connection is added, and the patches are merged back to the shape matching the stage input (Merge patches). After all stages, the resulting patches are pooled (GlobalAvgPool) and connected with a dense layer to output the z Zernike coefficients.

As none of the aforementioned ML-AO methods meet all these specifications, we endeavored to create one better suited to the needs of AO-LLSM. Our baseline model architecture, selected from an ablation study (Appendix A, Supplementary Fig. S2–S4), contains two transformer stages with patches of 32 and 16 pixels, respectively (Fig. 1c).

Priors can greatly improve the performance of any ML approach. For our method, we depend on the prior that each isoplanatic sub-volume (i.e., having the same aberration) within the larger volume of interest contains one or more fluorescent puncta of true sub-diffractive size. Here, we introduce these by using genome-edited specimens expressing fluorescent protein-fused versions of AP2—an adaptor protein that targets clathrin-coated pits (CCPs) ubiquitously present at CCPs located on the plasma membrane of all cells (Methods). While this entails a one-time upfront cost for each specimen type, it noninvasively produces a robust signal for AO correction that does not preclude simultaneously imaging another subcellular target that occupies the same fluorescence channel, provided they are computationally separable [9].

2 RESULTS

2.1 Benchmark comparisons of AOVIFT to other architectures

We created five variants of AOVIFT by varying the numbers of layers and heads in each stage (Supplementary Table S2) to explore the tradeoffs between model size (number of parameters and memory footprint), speed (floating-point operations (FLOPs) required, training time, and latency), and prediction accuracy (Supplementary Fig. S3). To compare these to existing state-of-the-art architectures, we developed 3D versions of ViT and ConvNeXt for AO inference in three and four different size variants, respectively (Appendix B). We trained all models with the same set of 2×10^6 synthetic image volumes chosen to capture the full diversity of aberrations and imaging conditions likely to be encountered in AO-LLSM (Methods) and tested AOVIFT on a separate set of 10^5 image volumes created to find the limits of its accuracy when presented with an even larger range of aberration magnitudes, SNR, and number of fluorescent puncta (Appendix C). We also tested the performance of all models and variants on 10^4 image volumes from a test set that contained only a single punctum in each (Fig. 2, Supplementary Fig. S8–S9, and Supplementary Table S3).

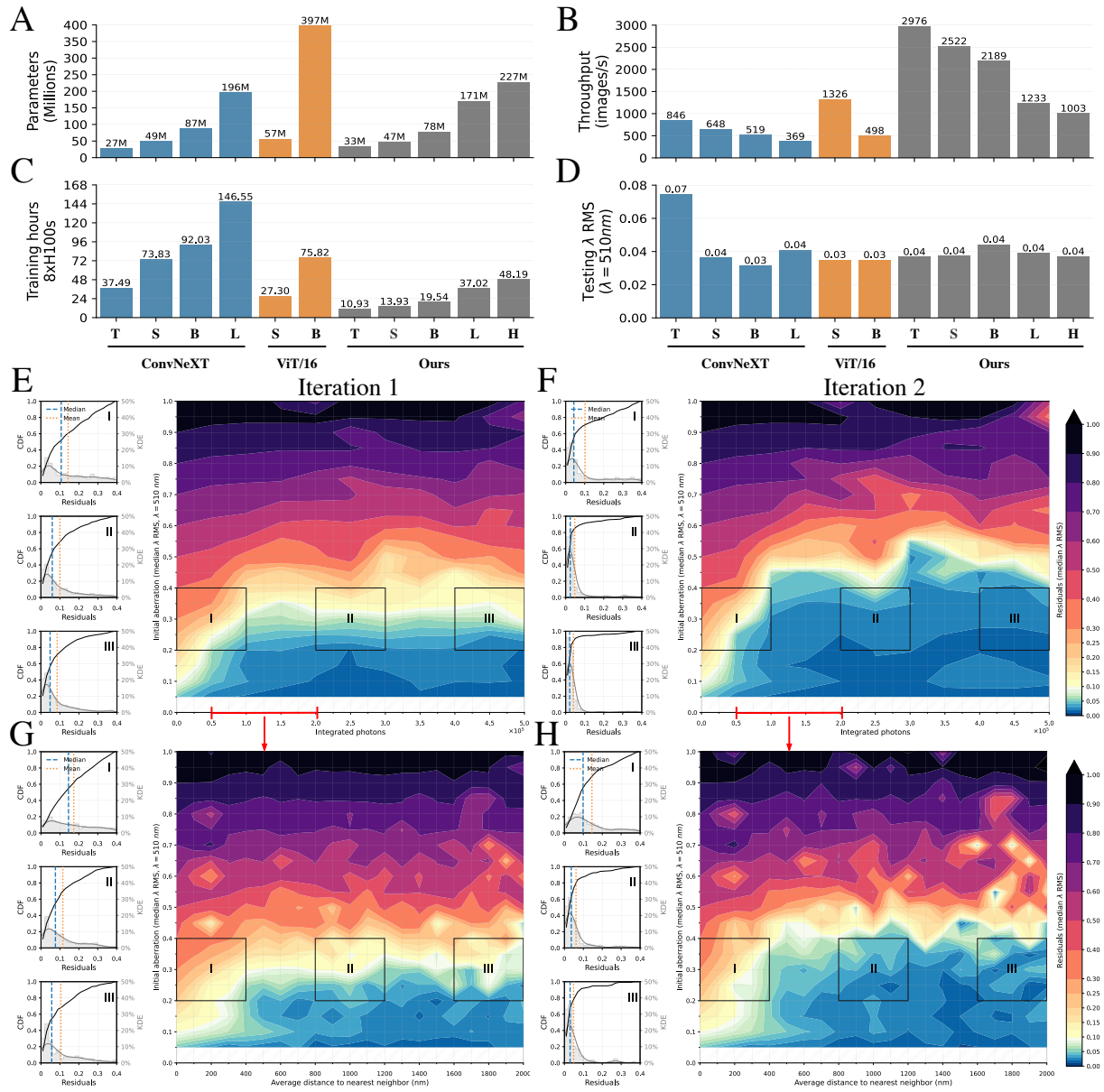


Figure 2: Comparison of different state-of-the-art architectures when applied to 3D aberration sensing. **A.** Total number of trainable parameters. **B.** Maximum predictions per second, using a batch size of 1024 on a single A100 GPU. Higher values are better. **C.** Training time on eight H100 GPUs. **D.** Median λ RMS residuals over 10K test samples after one correction, with aberrations ranging between 0.2 λ to 0.4 λ , simulated with 50K to 200K integrated-photons. **E–F.** Median λ RMS residuals using our Small model for a single bead over a wide range of SNR. **G–H.** Median λ RMS residuals using our Small model for several beads (up to 150 beads), simulated at photon levels from 50K to 200K per bead. Lower values are better for all performance indicators listed here, except for **B**.

While all models but the smallest variant of ConvNeXt were able to reduce the median residual error in a single iteration of aberration prediction to less than the diffraction limit (Fig. 2d), AOVIFT excelled in its parsimonious use of compute resources: training time using a node with eight NVIDIA H100 GPUs (Fig. 2c); training FLOPs (Supplementary Fig. S8c); and memory footprint (Supplementary Fig. S8f). This reflects the benefits of our multi-stage architecture: faster convergence by learning features across different scales, accurate prediction even at comparatively modest model size (Fig. 2a), highest inference rate among the models tested (Fig. 2b), and fastest single-shot inference time (“latency”, Supplementary Fig. S8h). Given its small size and low latency, we chose the Small variant of AOVIFT as our primary model for evaluation.

2.2 In silico evaluations of AOVIFT

Diffraction-limited performance is conventionally defined by wavefront distortions below $\approx 0.075\lambda$ RMS or $\lambda/4$ peak-to-valley, corresponding to a Strehl ratio of 0.8 under the Rayleigh quarter-wave criterion [10, 11]. In silico evaluation using the 10^4 single punctum test images show AOVIFT recovers diffraction-limited performance in a single iteration in nearly all trials where the initial aberration is $< 0.30\lambda$ RMS and the integrated signal is $> 5 \times 10^4$ photons (Fig. 2e). The corrective range increases to 0.40, 0.50, 0.55, and 0.6λ RMS for 2-5 iterations, respectively, although $\sim 5 \times 10^4$ photons remains the floor of required signal (Fig. 2f, Supplementary Fig. S10). This is comparable to the signal needed for SH wavefront sensing [2, 3] and at least 3x lower than that needed for PhaseRetrieval. In comparison, PhaseNet [4] and PhaseRetrieval [12] extend the diffraction limited range only slightly (initial aberration $< 0.15\lambda$ RMS) after a single iteration on the same test data (Supplementary Fig. S11a, b) and, in contrast to AOVIFT, do not appreciably increase this range after multiple iterations (Supplementary Fig. S12a-f). PhaseRetrieval does advantageously reduce residuals after a single iteration over a much broader range of initial aberration than AOVIFT, and this trend continues with further iteration, albeit never back to the diffraction limit (Supplementary Fig. S12a-c). However, this advantage is lost if the fiducial bead is not centered in the field of view (FOV), and the predictive power of PhaseNet is lost completely under the same circumstances (Supplementary Fig. S11d, e), because the widefield 3D image of the bead is then clipped. Furthermore, PhaseRetrieval and PhaseNet assume *a priori* the existence of only a single bead. AOVIFT is trained on 1–5 puncta falling anywhere within the FOV but, thanks to the normalization step to eliminate phase fringes from multiple puncta (Supplementary Fig. S4d), produces inferences comparably accurate to a single punctum for up to 150 puncta, provided their mean nearest neighbor distance is $> 400\text{nm}$ (Fig. 2g, h, Supplementary Fig. S13). Indeed, AOVIFT relies on the combined signal of multiple native but dim sub-diffractive biological assemblies such as CCPs to achieve accurate inferences.

2.3 Experimental characterization on fiducial beads

We performed all experiments using the AO-LLSM microscope schematized in Supplementary Fig. S14. For initial characterization of AOVIFT’s ability to correct a wide range of possible aberrations, we performed 66 separate experiments wherein we:

- introduced aberration by applying to the deformable mirror (DM) one of the 66 possible combinations of one or two Zernike modes (from the first 15, excluding piston, tip/tilt, and defocus), with each mode set to 0.2λ RMS amplitude;
- used AO-LLSM with the *MBSq-35* LLS excitation profile of Supplementary Table S6 to image a field of 100 nm diameter fluorescent beads with this aberration;
- used AOVIFT to predict the aberration;
- applied the corrective pattern to the DM;
- repeated b-d for 5 iterations.

In 45 cases, we recovered diffraction-limited performance in two iterations (Fig. 3), and in 5 iterations for 11 more (Supplementary Fig. S15). In the remaining 10 cases, aberrations were reduced by at least 50% after 5 iterations.

2.4 Correction of aberrations on live cultured cells

We next tested the ability of AOVIFT to correct aberrations during live cell imaging under biologically relevant conditions of limited signal, dense puncta, and specimen motion. To this end, we applied aberrations to the DM and imaged cultured SUM 159 human breast cancer-derived cells gene edited to produce endogenous levels of the clathrin adapter protein AP-2 tagged with eGFP. This yielded numerous membrane-bound CCPs at various stages of maturation that were suitable for aberration measurement. In one example (Fig. 4a), we applied a 2.9λ peak-to-valley (P-V) aberration to the DM consisting of a mix of horizontal coma and oblique trefoil (Z_3^1 and Z_3^3), and recovered near diffraction-limited performance after two iterations (Supplementary Table S4). Peak signal at the CCPs increased 2-3 fold post-correction, and the spatial frequency content as seen in orthoslices through the 3D FFT (insets at bottom) increased in every iteration. In another case (Fig. 4b), we reduced a 3.1λ P-V aberration composed of a combination of horizontal coma and primary spherical (Z_3^1 and Z_4^0) to 0.069λ RMS after two iterations, increasing CCP signal by 3-4 fold (Supplementary Table S4). Four more examples of correction on cells and fiducial beads after applying single modes of 1λ P-V aberration are given in Supplementary Fig. S16, and five more examples of two mode correction are shown in Supplementary Fig. S17.

2.5 In vivo correction of native aberration within a zebrafish embryo

As a transparent vertebrate, zebrafish are a popular model organism for imaging studies. However, the spatially heterogeneous refractive index within multicellular organisms and the discontinuity of refractive index at their surfaces with respect to the imaging medium result in aberrations that vary throughout their interiors (Fig. 5a). We corrected $\sim 2\lambda$ P-V aberration in one such region (Fig. 5b, top) with AOVIFT (Fig. 5b, bottom) near the notochord of a transgenic zebrafish embryo 72 hours post fertilization expressing AP2-mNeonGreen in CCPs at the membranes of all cells (*ap2s1:ap2s1-mNeonGreen^{k800}*, Methods) and recovered spatial frequencies across the corrected volume (FFTs at right) comparable to SH correction over the same region (Fig. 5b, middle).

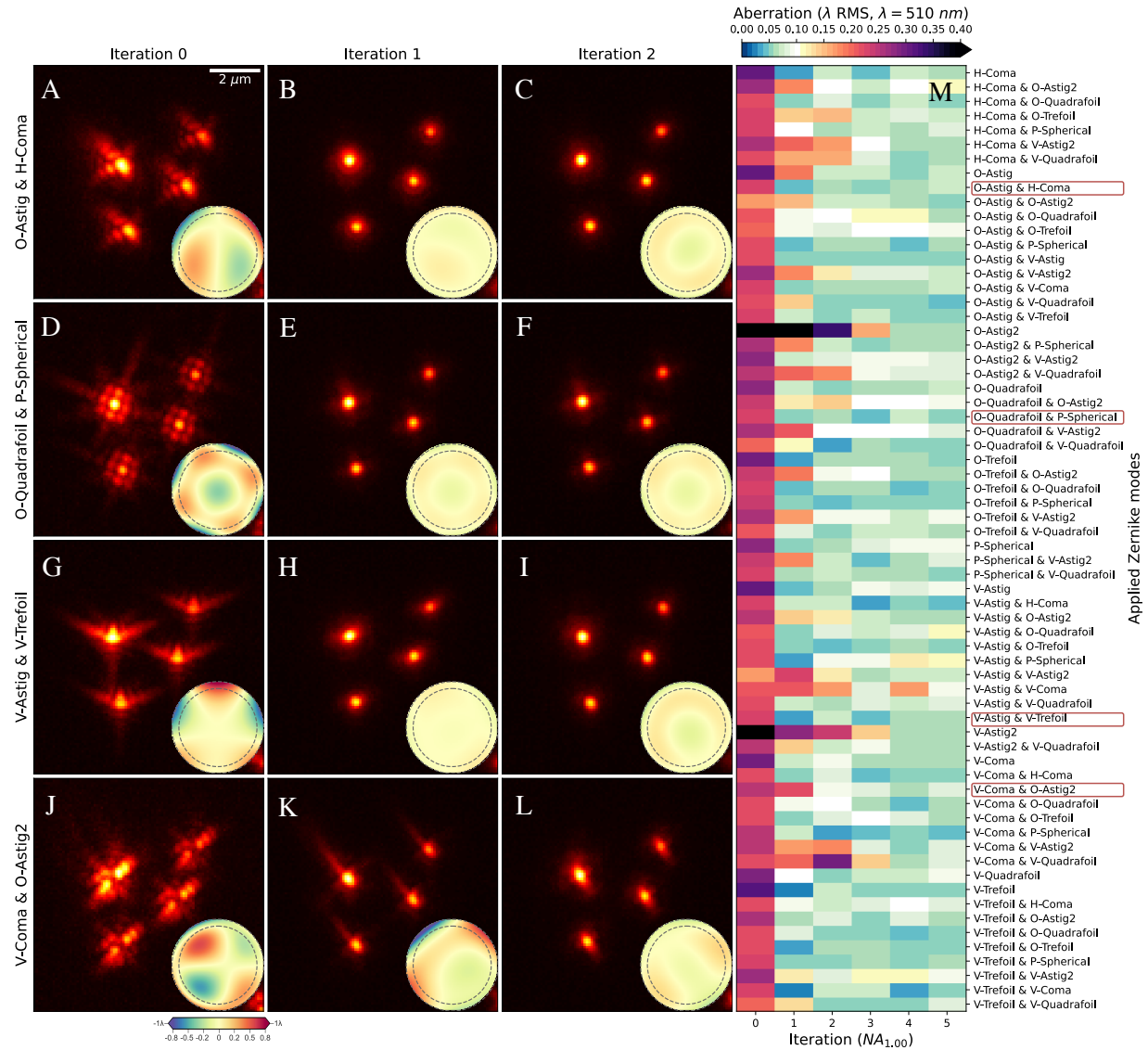


Figure 3: Experimental correction of beads with initial artificial aberrations. A–L. Four examples, O-Astig & H-Coma ($Z_{n=2}^{m=-2} + Z_{n=3}^{m=1}$), O-Quadrafoil & P-Spherical ($Z_{n=4}^{m=-4} + Z_{n=4}^{m=0}$), V-Astig & V-Trefoil ($Z_{n=2}^{m=2} + Z_{n=3}^{m=-3}$), V-Coma & O-Astig2 ($Z_{n=3}^{m=-1} + Z_{n=4}^{m=-2}$), where the initial aberration was artificially applied by the DM. *Iteration 0* shows XY maximum projection of four beads with initial aberration imaged using LLS, providing initial conditions for AOViFT predictions. *Iteration 1* shows the resulting field of beads after applying AOViFT prediction to the DM. *Iteration 2* shows the results after applying the AOViFT prediction measured from *Iteration 1*. Insets show the AOViFT predicted wavefront over the NA = 1.0 pupil with a dashed line at NA = 0.85 M. Heatmap of the residual aberrations (measured via PhaseRetrieval on isolated bead) after applying AOViFT predictions, starting with a single Zernike mode up to Mode 14 ($Z_{n=4}^{m=4}$) across up to 5 iterations.

In a second embryo expressing AP2-mNeonGreen in CCPs and mChilada-Cox8a in mitochondria (Fig. 5c), we used the mNeonGreen signal to correct $\sim 1.5\lambda$ P-V aberration (top row) in one region, which provided an aberration-corrected view of both CCPs and

mitochondria (second row). Deconvolution of the aberrated images using an assumed ideal PSF only amplified high frequency artifacts (third row), but provided a more accurate representation of sample

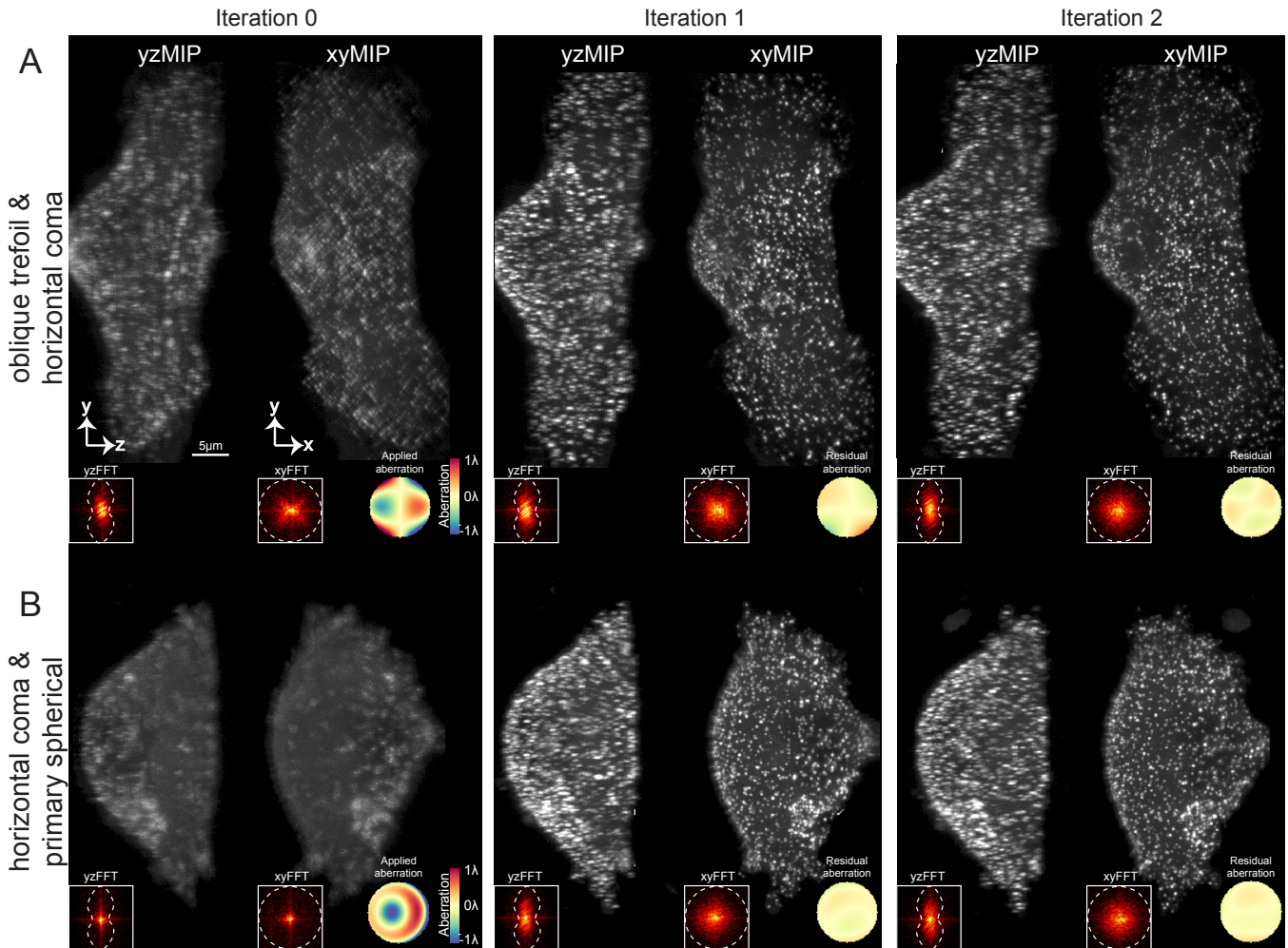


Figure 4: Correction of aberrations in live SUM159-AP-2 cells expressing $\sigma 2$ -eGFP. A. 3D volume SUM159-AP2 cells represented as XY and YZ MIPs covering a $15.7 \times 55.6 \times 25.6 \mu\text{m}^3$ FOV after applying a 2.9λ peak-to-valley (P-V) aberration to the DM. This aberration combines horizontal coma Z_3^1 and oblique trefoil Z_3^3 . B. XY and YZ MIPs of a similar FOV with 3.1λ P-V aberration composed of horizontal coma (Z_3^1) and primary spherical (Z_4^0). In both cases, near diffraction-limited performance was recovered after two iterations. The insets show FFTs and corresponding wavefronts for each iteration. Scale bar, $5\mu\text{m}$

structure (bottom row) for the aberration-corrected ones by compensating for known attenuation of high spatial frequencies in the ideal optical transfer function (OTF).

2.6 Correction of spatially varying aberrations in vivo

With guide star illuminated SH sensors, aberration measurement is not accurate unless it is confined to a single isoplanatic region. However, these are often much smaller than the volume of interest, and their boundaries are not generally known *a priori*. Consequently, microscopists are often forced to map aberrations by serial SH measurement over many small, tiled subregions whose dimensions are a matter of educated guesswork. On the other hand, with AOVIFT we generated a complete map of 204 aberrations (Fig. 6a) at $6.3 \mu\text{m}$ intervals over $37 \times 211 \times 12.8 \mu\text{m}^3$ in a live zebrafish embryo 48 hpf

(Fig. 6b, d) in ~ 1.5 minutes on a single node of four A100 GPUs. Unfortunately, it is not possible to apply a corrective pattern to a single pupil conjugate DM and thereby correct this spatially varying aberration across the entire FOV. One option would be to apply each aberration in turn and image the tiles one by one, or together in groups of similar aberration. Although slow, this would recover the full information of which the microscope is capable. However, a much faster and simpler alternative is to deconvolve each raw image tile with its own unique aberrated PSF (Fig. 6c, e). This does not recover full diffraction-limited performance, but it does suppress aberration-induced artifacts and provides a more faithful representation of the underlying sample structure (Figs. 6f–h).

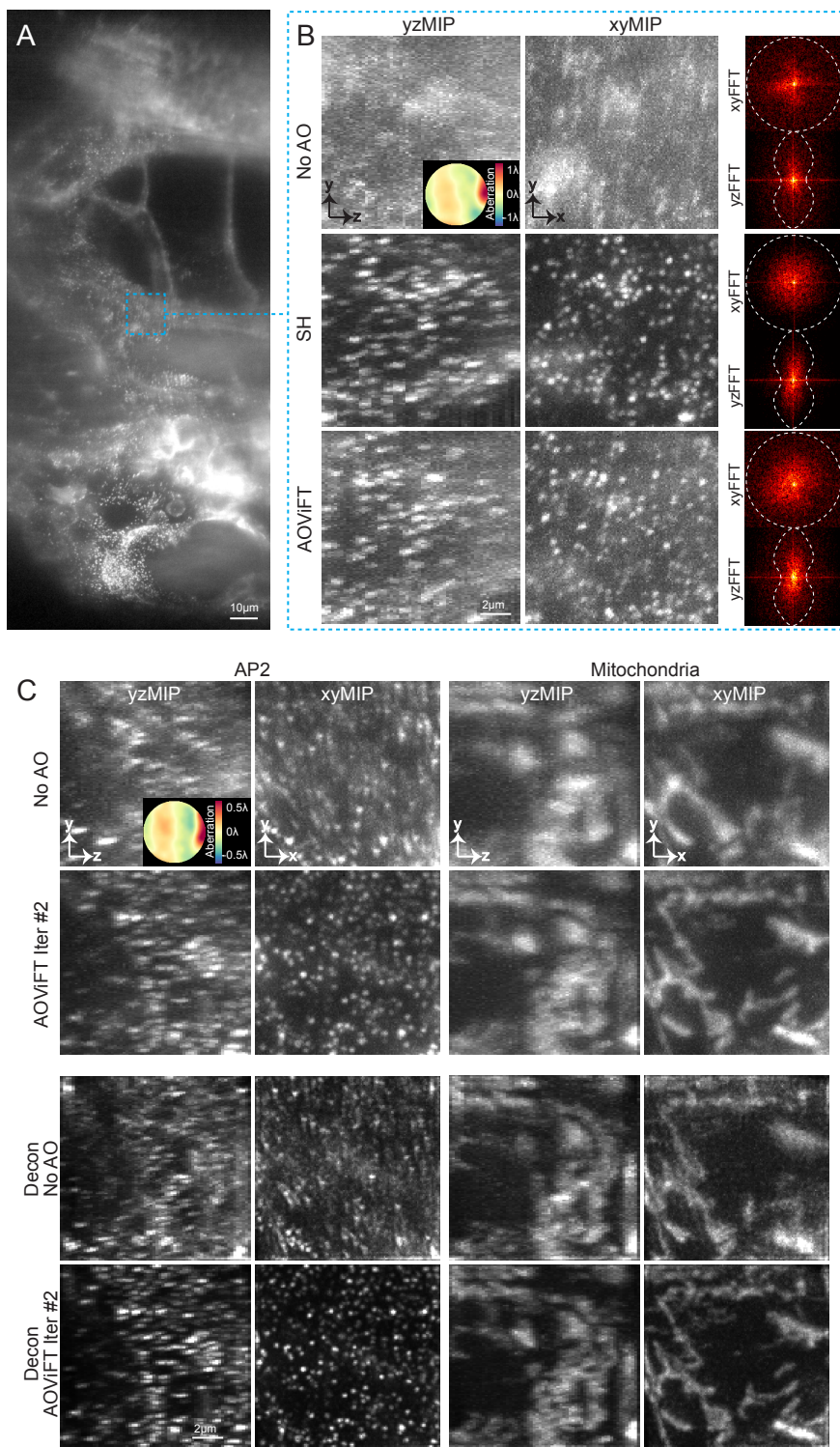


Figure 5: In vivo, in situ correction of native aberrations in zebrafish embryos. **A.** XY MIP of a 72 hpf gene-edited zebrafish embryo expressing endogenous AP2-mNeonGreen, exhibiting native and spatially varying aberrations near the notochord. Scale bar, $10\mu\text{m}$. **B.** Enlarged view of the dashed blue box in (A). The XY and YZ MIPs, along with the corresponding FFTs of a $12.5 \times 12.5 \times 12.8\mu\text{m}^3$ FOV, show $\sim 2\lambda$ P-V of sample-induced aberration without AO (top row), corrected by SH (middle row), and corrected by AOVIFT (bottom row). The contrast for each volume was scaled to its 1st and 99.99th percentile intensity values. Scale bar, $2\mu\text{m}$. **C.** XY and YZ MIPs of a different gene-edited zebrafish embryo expressing exogenous AP2-mNeonGreen and injected mRNA for mChilada-Cox8a (to visualize mitochondria). The AP2 signal was used to infer the underlying aberration, and the same correction was applied to both channels. The top row shows $\sim 1.5\lambda$ P-V aberration; the second row shows AOVIFT correction after two iterations. The third and fourth rows present the results of OTF masked Wiener (OMW) deconvolution without and with AOVIFT corrected volumes, respectively. Scale bar, $2\mu\text{m}$.

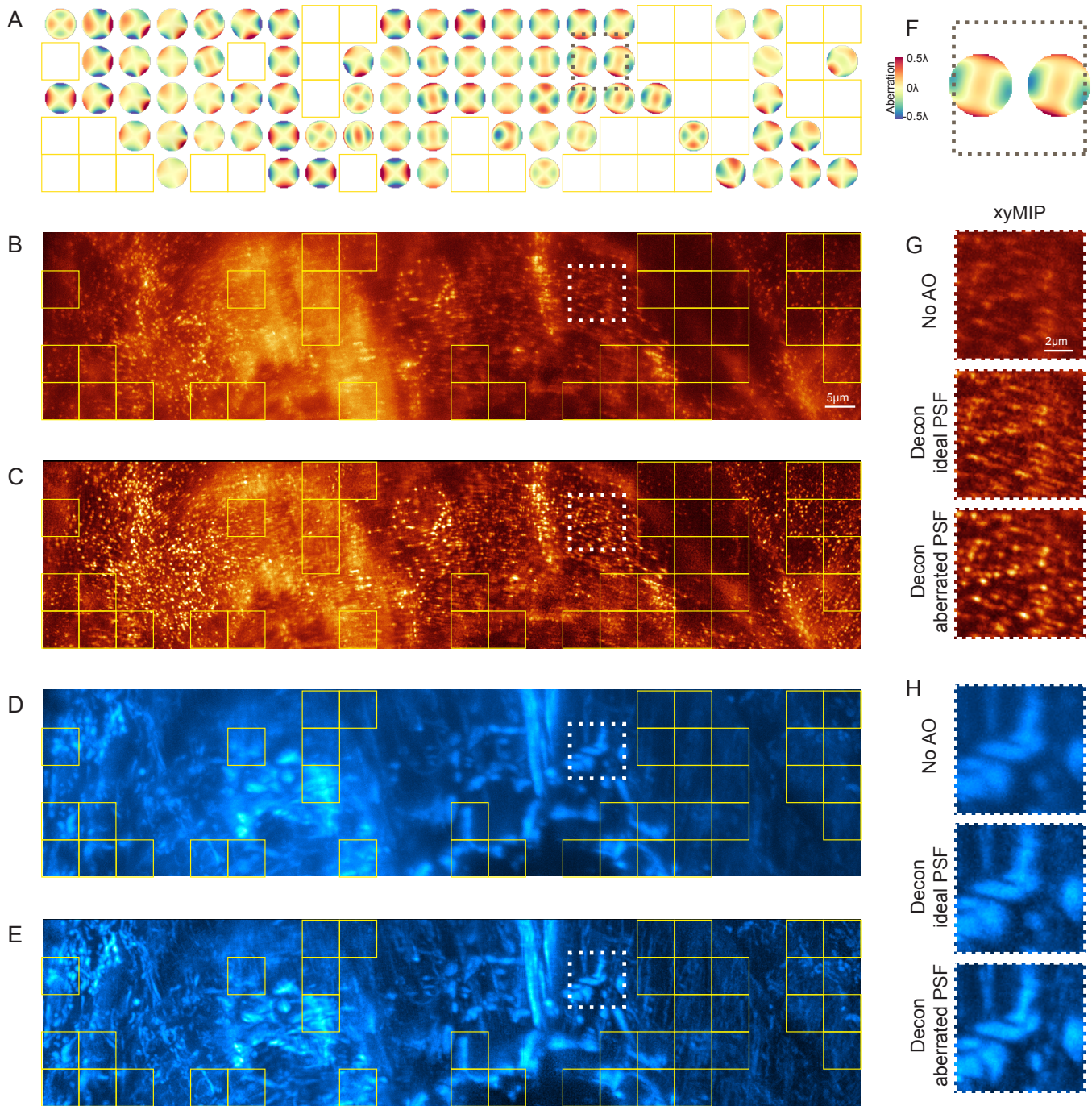


Figure 6: Correcting aberrations post acquisition using spatially varying deconvolution in a zebrafish embryo. **A.** Isoplanatic patch map determined by AOVIFT for 204 tiles ($6.3 \times 6.3 \times 12.8 \mu\text{m}^3$ each), spanning $37 \times 211 \times 12.8 \mu\text{m}^3$ FOV in a live, gene-edited zebrafish embryo expressing endogenous AP2-mNeonGreen. The yellow box marks areas with insufficient spatial features to accurately determine aberrations; an ideal PSF was used for OMW deconvolution in these regions. **B.** XY MIP of the AP2 signal without AO. Scale bar, $5 \mu\text{m}$. **C.** XY MIP of each tile after deconvolution with spatially varying PSFs predicted by AOVIFT. **D–E.** Raw (D), and deconvolved (E) XY MIPs of the mitochondria channel for the same region. **F.** Enlarged view of the wavefronts within the black dashed box in (A). **G–H.** Zoomed views of AP2 (G), and mitochondria (H) structures from (B–E), comparing No AO to OMW deconvolution using either an ideal PSF or spatially varying tile-specific aberrated PSFs predicted by AOVIFT. Scale bar, $2 \mu\text{m}$.

3 DISCUSSION

AOViFT provides accurate mapping of spatially varying sample-induced aberrations in specimens having sub-diffractive puncta. Although AOVIFT can be slower than using SH for a single ROI, it gains a substantial net speed advantage when mapping multiple ROIs across a large field of view (FOV) due to its parallelizable inference framework (Supplementary Table S5). Moreover, its throughput can be further accelerated via distributed GPU processing across multiple nodes and by compiling the model with TensorRT¹ for optimized inference. Unlike AOVIFT, SH measurement with a TPE guide star has the key advantage of being agnostic to the fluorescence distribution within each isoplanatic region, but requires additional hardware (TPE laser, galvos, SH sensor) and the TPE power level must be carefully monitored to minimize photodamage. In addition, since the isoplanatic regions are not known *a priori*, the initial measurement grid for SH sensing must be very dense to accurately map aberrations and their rate of change across the FOV, requiring additional time at an additional cost to the photon budget. Conversely, AOVIFT determines the aberration map from a single large 3D image volume, and can therefore iteratively adjust tile sizes or positions *in silico* as needed until the map converges to an accurate solution.

Although trained for a specific LLS type (Supplementary Table S6), AOVIFT retained predictive capability when tested *in silico* with other light sheets as well (Supplementary Fig. S20). While training specifically for such light sheets might increase the predictive range even further, a more fruitful path might be to augment the synthetic training data with light sheets axially offset from the detection focal plane to replace the closed-loop hardware based mitigation of such offsets needed now [3]. Future models might leverage ubiquitous subcellular markers, such as plasma membranes or organelles, rather than genetically-expressed diffraction-limited puncta, provided these markers contain sufficient high spatial frequency content for accurate inference of aberrations. Finally, to enhance generalizability of AOVIFT and reduce overfitting to narrowly defined imaging scenarios, future models should incorporate a more diverse range of light-sheets, specimen types, and labeling strategies.

Development of AOVIFT highlighted the challenges of constructing a 3D transformer-based architecture for AO correction. Each iteration of model design, training, and testing required specialized simulated data pipelines, large GPU resources, and extensive hyperparameter tuning—leading to lengthy model development cycles. A key bottleneck is the absence of universally applicable, large pre-trained models for volumetric imaging data—a limitation that extends beyond adaptive optics applications.

Unlike the natural image domain, where ViT benefited from extensive training on standardized 2D datasets, a comparable “foundation model” for 3D microscopy is pending the collection of similar datasets. This gap severely limits how far and how quickly new methods like AOVIFT can be generalized. While our work highlights the feasibility of building a solution for a given task (e.g., AO corrections under specific imaging conditions), adapting to new scenarios such as new sample types, microscope geometries, or

aberration ranges typically requires substantial retraining and additional data curation.

These limitations highlight the need for pre-trained foundation models in volumetric microscopy. We consider AOVIFT, a 3D vision transformer model, as a stepping stone towards the more ambitious goal of creating a 4D model pre-trained on massive volumetric microscopy datasets. Such a model could be fine-tuned for tasks across spatial scales (from molecules to organisms), and temporal scales (from stochastic molecular kinetics to embryonic development) [13]. Realizing this vision would require petabytes of high-quality curated 4D datasets and significant computational resources. However, successful implementation would dramatically shorten development timelines, improve generalization, and reduce the overhead of custom training for varied experimental setups or microscope configurations.

4 METHODS

4.1 AO-LLS microscope

Imaging was performed using an adaptive optical lattice light-sheet (AO-LLS) microscope similar to one described previously [3] (Supplementary Fig. S14, Supplementary Table S7). Briefly, 488-nm and 560nm lasers (500 mW 2RU-VFL-P-500-488-B1R and 1000mW 2RU-VFL-P-1000-560-B1R, MPB Communications Inc.) were modulated via an acousto-optical tunable filter (AOTF; Quanta-Tech, AA OptoElectronic, AOTFnc-400.650-CPCh-TN) and shaped into a stripe by a Powell lens (Laserline Optics Canada, LOCP-8.9R20-2.0) and a pair of 50- and 250-mm cylindrical lenses (25 mm diameter; Thorlabs, ACY254-050, LJ1267RM-A). The stripe illuminated a reflective, phase-only, gray-scale spatial light modulator (SLM; Meadowlark Optics, AVR Optics, P1920-0635-HDMI, 1920 × 1152 pixels) located at a sample conjugate plane. An 8-bit phase pattern written to the SLM generated the desired light-sheet pattern in the sample, and an annular mask (Thorlabs Imaging) at a pupil conjugate plane blocked unwanted diffraction orders before the light passed through the excitation objective (Thorlabs, TL20X-MPL). A pair of pupil conjugate galvanometer mirrors (Cambridge Technology, Novanta Photonics, 6SD11226 and 6SD11587) scanned the light sheet at the sample plane. The sample was positioned at the common foci of the excitation and detection objectives by a three axis XYZ stage (Smaract; MLS-3252-S, SLS-5252-S, SLS-5252-S). Fluorescence emission from the sample was collected by a detection objective (Zeiss, 20×, 1.0 NA, 421452-9800-000), reflected off a pupil conjugate deformable mirror (DM; ALPAO, DM69) that applied aberration corrections, and then recorded on two sample conjugate cameras (Hamamatsu ORCA Fusion).

Shack Hartmann measurements (Supplementary Fig. S18) were performed on the same microscope by localizing the intensity maxima (on a Hamamatsu ORCA Fusion) formed by the emitted light after passage through a pupil conjugate lenslet array (Edmund Optics, 64-479). The positional shifts of these maxima relative to those seen with no specimen present encode the pupil wavefront phase [2], which can then be reconstructed.

4.2 Integration with microscope

AOViFT inference is routinely performed on the microscope acquisition PC (Intel Xeon, W5-3425, Windows 11, 512GB RAM, NVIDIA

¹<https://docs.nvidia.com/deeplearning/tensorrt/pdf/TensorRT-Developer-Guide.pdf>

A6000 with 48GB VRAM). Inferences are made in an Ubuntu Docker container based on the TensorFlow NGC Container (24.02-tf2-py3) running in parallel with the microscope control software. Data communication between AOVIFT and the microscope control software is handled through the computer's file system. Image files and command-line parameters are passed to the model, and an output text file reports the resultant DM actuator values (Fig. S19). When a volume is large enough to require tiling and dozens of volumes need to be processed, model inferences are parallelized and run using a SLURM compute cluster consisting of 4 nodes, each node containing four NVIDIA A100 80GB.

4.3 Fluorescent beads and cells expressing fluorescent endocytic adaptor AP2

The 25 mm coverslips (Thorlabs, CG15XH) used for imaging beads, cells and zebrafish embryos were first cleaned by sonication in 70% ethanol followed by Milli-Q water, each for at least 30 minutes. They were then stored in Milli-Q water until use. Gene-edited SUM159 AP2-eGFP cells [14] were grown in Dulbecco's modified Eagle's medium (DMEM)/F12 with GlutaMAX (Gibco, 10565018) supplemented with 5% fetal bovine serum (FBS; Avantor Seradigm 89510-186), 10mM HEPES (Gibco 15630080), 1 μ g/ml hydrocortisone (Sigma H0888), 5 μ g/ml insulin (Sigma I9278). Fluorescent beads (0.2 μ m diameter, Invitrogen FluoSpheres Carboxylate-Modified Microspheres, 505/515 nm, F8811 or 0.2 μ m diameter Tetraspeck, Thermo Fisher Scientific Invitrogen T7280) alone or with cells at 30-50% confluency were deposited onto plasma-treated and poly-D-lysine (Sigma-Aldrich, P0899) treated 25mm coverslips. Cells were cultured under standard conditions (37°C, 5% CO₂, 100% humidity) with twice weekly passaging. The SUM159 AP2-eGFP cells were imaged in Leibovitz's L-15 medium without phenol red (Gibco, 21083027), with 5% FBS (American Type Culture Collection, SCRR-30-2020), 100 μ M Trolox (Tocris, 6002), and 100 μ g/ml Primocin (InvivoGen, ant-pm-1) at 37°C. Aberrations of approximately 1 λ P-V were induced using a deformable mirror in 10 configurations of Zernike modes (Z_2^2 , Z_3^{-3} , Z_3^{-1} , Z_4^0 , and their pairwise combinations). Widefield point spread functions were collected from 0.2 μ m fluorescent beads to confirm the aberrations applied and residual aberrations after correction (Supplementary Table S7).

4.4 Zebrafish embryos expressing fluorescent AP2 and mitochondria

Genome edited *ap2s1* expressing zebrafish (Genome editing of *ap2s1*, *ap2s1:ap2s1-mNeonGreen^{bk800}*, Appendix D) were injected with *cox8-mChilada* mRNA for two color experiments. The N-terminal 34 amino acids of *Cox8a* was cloned into a pMTB backbone with a linker and *mChilada* coding sequence on the c-terminus (unpublished, gift from Nathan Shaner). The plasmid was linearized, and mRNA was synthesized using a SP6 mMessage mMachine transcription kit (Thermo Fisher). RNA was purified using an RNeasy kit (Qiagen) and embryos were injected with 2 nl of 10 ng/ μ l *Cox8a-mChilada*, 100 mM KCl, 0.1% phenol red, 0.1 mM EDTA, and 1 mM Tris, pH 7.5. Zebrafish embryos were first nano-injected with 3 nL of a solution containing 0.86 ng/ μ l α -bungarotoxin protein, 1.43 \times PBS, and 0.14% phenol red. The injected embryos were mounted for imaging using a custom, volcano-shaped agarose mount. Each

mount was constructed by solidifying a few drops of 1.2% (wt/wt) high-melting agarose (Invitrogen UltraPure Agarose, 16500-100, in 1 \times Danieau buffer) between a 25 mm glass coverslip and a 3D-printed mold (Formlabs Form 3+, printed in clear v4 resin). This created ridges that formed a narrow groove. A hair-loop was used to orient the embryo within the agarose groove, positioning the left lateral side upward. Subsequently, 10-20 μ L of 0.5% (wt/wt) low-melt agarose (Invitrogen UltraPure LMP Agarose, 16520-100, in 1 \times Danieau buffer) preheated to 40°C, containing 0.2 μ m Tetraspeck microspheres, was added on top of the embryo. This layer solidified around the embryo to secure it while providing fiducial beads for sample finding. Once the low-melt agarose solidified, the volcano-shaped mount was held by a custom sample holder for imaging. The embryo was oriented so that its anterior-posterior axis lay parallel to the sample x-axis, with the anterior end facing the excitation objective and the posterior end facing the detection objective. The microscope objectives and the sample was immersed in a \sim 50 mL bath of 1 \times Danieau buffer were fully submerged, ensuring the embryo remained in buffered media. Measurements for AOVIFT and Shack Hartmann were done serially on the same FOV to compare the aberration corrections of both methods (Supplementary Table S7).

4.5 Spatially varying deconvolution

To compensate for sample-induced aberrations post-acquisition, we performed a tile-based spatially varying deconvolution on each 3D volume. Each volume was first subdivided into multiple 3D tiles approximating isoplanatic patches. A AOVIFT predicted PSF (for compensation) or an ideal PSF (for no compensation) was assigned to each tile, and aberrations were corrected using OTF masked Wiener (OMW) deconvolution [15]. To minimize boundary artifacts during deconvolution, the tile size was extended by half the PSF width at each boundary (32 pixels); after deconvolution, these overlaps were removed and the deconvolved core regions were stitched together to form the final corrected volume. All computations were done in MATLAB 2024a (Mathworks).

4.6 Synthetic training/testing datasets

To train a model for predicting optical aberrations from images of sub-diffractive objects in biological samples, we generated synthetic datasets encompassing a range of relevant variables (e.g., aberration modes and amplitudes, number and density of puncta, SNR). This synthetic dataset generation procedure is as follows:

For a single sub-diffractive punctum, the electric field in the rear pupil of the detection objective is given by:

$$E(k_x, k_y) = A(k_x, k_y) \exp(i\phi(k_x, k_y)) \quad (1)$$

where $A(k_x, k_y)$ is the pupil amplitude and $\phi(k_x, k_y)$ is the pupil phase. Under aberration-free conditions, $\phi(k_x, k_y)$ is a constant. We can empirically determine $A(k_x, k_y)$ by acquiring a widefield image of an isolated sub-diffractive object (100 nm fluorescent bead), performing phase retrieval [12, 16], and applying the opposite of the retrieved phase using a pupil conjugate DM so that $\phi(k_x, k_y)$ becomes a constant.

The electric field for the image of a single aberrated punctum is:

$$E_{abb}(k_x, k_y) = A(k_x, k_y) \exp(i\phi_{abb}(k_x, k_y)) \quad (2)$$

where the $\phi_{\text{abb}}(k_x, k_y)$ is described as a weighted sum of Zernike modes of unique amplitudes:

$$\phi_{\text{abb}}(k_x, k_y) = \sum_{m,n} \alpha_n^m Z_n^m(k_x, k_y) \quad (3)$$

Empirically, zebrafish induced aberrations for the microscopes used here are well described by combinations of 11 of the first 15 Zernike modes [17] (Supplementary Fig. S1), for which $n \leq 4$, excluding piston (Z_0^0), tip (Z_1^{-1}), tilt (Z_1^1), and defocus (Z_2^0) (as these represent phase offsets or sample translation). The distributions and amplitudes of the remainder are used to build the training set as discussed below.

The aberrated 3D detection PSF of a sub-diffractive punctum is approximated by:

$$\text{PSF}_{\text{abb}}^{\text{det}}(x, y, z) = \left| \iint_{\text{pupil}} E_{\text{abb}}(k_x, k_y) \exp[i(k_x x + k_y y + k_z z)] dk_x dk_y \right|^2 \quad (4)$$

where $k_z = \sqrt{\left(\frac{2\pi\eta}{\lambda}\right)^2 - k_x^2 - k_y^2}$, η is the refractive index of the imaging medium, and λ being the free-space wavelength of the fluorescence emission.

For light sheet microscopy, the aberrated 3D overall PSF is:

$$\text{PSF}_{\text{abb}}^{\text{overall}}(x, y, z) = \text{PSF}^{\text{exc}}(z) \cdot \text{PSF}_{\text{abb}}^{\text{det}}(x, y, z) \quad (5)$$

where $\text{PSF}^{\text{exc}}(z)$ is given by the cross-section of the swept light sheet used for imaging. Examples of these PSFs are shown in Supplementary Fig. S20I-V, with *MBSq-35* in Supplementary Table S6 used for training and imaging (see [18] for additional information on these light sheets).

Each synthetic training volume sample V is $64 \times 64 \times 64$ voxels in size spanning $8 \times 8 \times 12.8 \mu\text{m}^3$ (with $125 \times 125 \times 200 \text{ nm}^3$ voxels) and containing between $J = 1$ to 5 puncta chosen from a uniform distribution and located randomly at points (x_j, y_j, z_j) within the volume. Each punctum is modeled as a Gaussian of full width at half maximum w_j randomly chosen from the set [100, 200, 300, 400] nm, allowing for slightly larger than the diffraction-limit features. The image of each punctum is generated by its convolution with the aberrated PSF:

$$I_j^{\text{bead}}(x, y, z) = \text{PSF}_{\text{abb}}^{\text{overall}}(x, y, z) \otimes \exp \left[-4 \ln(2) \frac{x^2 + y^2 + z^2}{w_j^2} \right] \quad (6)$$

The integrated photons N_o per punctum were selected from a uniform distribution of 1 to 200,000 photons. The total intensity distribution is:

$$I_{\text{photon}}(x, y, z) = \Upsilon \cdot \sum_{j=1}^J I_j^{\text{bead}}(x - x_j, y - y_j, z - z_j) \quad (7)$$

where,

$$\Upsilon = \frac{N_o}{\iiint_{-\infty}^{\infty} I_j^{\text{bead}}(x, y, z) dx dy dz} \quad (8)$$

Since the signal from each aberrated punctum can exceed the boundary of V , total signal S_V within V is:

$$S_V = \iiint_V I(x, y, z) dx dy dz \leq JN_o \quad (9)$$

After accounting for partial signal contributions (S_V) the photons per voxel were converted to camera counts by applying the quantum efficiency QE, Poisson shot noise η , and camera read noise ϵ to arrive at the final synthetic training set example:

$$I_{\text{camera}}(x, y, z) = QE \cdot I_{\text{photon}}(x, y, z) + \eta[QE \cdot I_{\text{photon}}(x, y, z)] + \epsilon \quad (10)$$

4.6.1 Zernike distributions. To ensure diversity in the training set to cover potential aberrations, each training example was chosen from the amplitudes of the eleven included aberration modes shown in color in Supplementary Fig. S1 with equal probability from one of four different distributions:

Single mode (Supplementary Fig. S21b). One mode randomly chosen, with amplitude α randomly chosen from $0 \leq \alpha \leq 0.5\lambda$ RMS.

Bimodal (Supplementary Fig. S21c). An initial target for the total amplitude α_t is randomly chosen from $0 \leq \alpha_t \leq 0.5\lambda$ RMS. A second partitioning factor ϵ is randomly chosen from $0 \leq \epsilon \leq 1$. The amplitudes of the two modes are then $\alpha_1 = \epsilon\alpha_t$ and $\alpha_2 = (1 - \epsilon)\alpha_t$.

Powerlaw (Supplementary Fig. S21d). An initial target for the total amplitude α_t is randomly chosen from $0 \leq \alpha_t \leq 0.5\lambda$ RMS. The initial partitioning factors ϵ_n for the modes are randomly chosen from a Lomax (i.e., Pareto II) distribution [19]:

$$\epsilon_n = \frac{\gamma}{(x_n + 1)^{\gamma+1}} \quad \text{where } \gamma = 0.75 \quad (11)$$

where each x_n is randomly chosen from $0 \leq x_n \leq 1$. They are then re-normalized:

$$\epsilon'_n = \frac{\epsilon_n}{\sum_{n=1}^{11} \epsilon_n} \quad (12)$$

and the final amplitudes of the modes are $\alpha_n = \epsilon'_n \alpha_t$.

Dirichlet (Supplementary Fig. S21e). An initial target for the total amplitude α_t is randomly chosen from $0 \leq \alpha_t \leq 0.5\lambda$ RMS. The initial partitioning factors ϵ_n for the modes are randomly chosen from $0 \leq \epsilon_n \leq 1$. They are then re-normalized:

$$\epsilon'_n = \frac{\epsilon_n}{\sum_{n=1}^{11} \epsilon_n} \quad (13)$$

and the final amplitudes of the modes are $\alpha_n = \epsilon'_n \alpha_t$.

Together, the training examples from these four distributions create a diverse set of overall aberration amplitudes and number of significant modes in the training data, with all eleven modes contributing equally across the dataset (Supplementary Fig. S21a).

4.6.2 Training dataset. For the model training, a dataset of 2 million synthetic 3D volumes was created, with aberration magnitude uniform sampled from 0.0 to 0.5λ RMS (at wavelength $\lambda = 510$ nm), uniform distribution of the number of objects between 1 and 5, and photons ranging between 1 and 200,000 integrated photons per object.

4.6.3 Test dataset. To evaluate our models, we created a test dataset with 100,000 3D volumes. The parameter distribution was the same as training, but extended the aberration magnitude up to 1.0λ RMS, and up to 500,000 integrated photons. To test the operational limit of our models, this test dataset included up to 150 objects in any given volume.

4.7 Fourier embedding

Most ML vision models operate on real-space representations of the data, which lack clearly defined limits on image size or feature descriptors of their content. Instead, we used Fourier domain embeddings (Supplementary Fig. S4). These are bound by the microscope’s OTF. Aberrations within an isoplanatic patch globally effect all photons within that patch, producing a unique, learnable “fingerprint” pattern in the FFT amplitude and phase (Appendix A.1, Supplementary Figs. S5–S7).

4.7.1 Preprocessing. To create Fourier embeddings (Fig. 1b) for our model, we preprocess the input 3D image stack W of CCPs within an isoplanatic region to suppress noise and edge artifacts (Fig. 1a),

$$V = \Upsilon(W). \quad (14)$$

The preprocessing module (Υ) begins with a set of filters to extract sharp-edged objects which reveal the aberration signatures: a Gaussian high-pass filter to remove inhomogeneous background and a low-pass filter via a Fourier frequency filter, with cutoff set at the detection NA limit ($\sigma=3$ voxels). A Tukey window (Tukey cosine fraction=0.5, in $\hat{x}\hat{y}$ only) is applied to remove FFT edge artifacts from the volume borders. No windowing is applied along the axial direction, \hat{z} , because embeddings are constructed near $k_z = 0$ where aberration information is maximized.

4.7.2 Embedding. Once preprocessed, a ratio of the resultant 3D FFT amplitude, to the 3D FFT amplitude of the ideal PSF (undergoing identical preprocessing steps) is used to generate the amplitude embedding, $\alpha(k_z)$ at each k_z plane:

$$V_{ideal} = \Upsilon(PSF_{ideal}) \quad (15)$$

$$\alpha = \frac{|\mathcal{F}(V)|}{|\mathcal{F}(V_{ideal})|} \quad (16)$$

where \mathcal{F} denotes the 3D Fourier transform. The most useful information content is located at $k_z = 0$, the principal plane located at the midpoint of the \hat{k}_z -axis. Three 2D planes from α_1 , α_2 , and α_3 along \hat{k}_z -axis as are necessary to extract axial information for inputs to the model as follows:

$$\alpha_1 = \alpha_{k_z=0} \quad (17)$$

$$\alpha_2 = \frac{1}{5} \sum_{i=0}^4 \alpha_{k_z=i} \quad (18)$$

$$\alpha_3 = \frac{1}{5} \sum_{i=5}^9 \alpha_{k_z=i} \quad (19)$$

where α_1 is the principal plane along the k_x -axis and k_y -axis, α_2 is the mean of five consecutive 2D planes starting from the principal plane, and α_3 is the mean of five consecutive 2D planes starting from the $k_z = 5$ plane (Supplementary Fig. S4a,c and Supplementary Fig. S7).

For the phase embedding, φ , we first remove interference from multiple puncta in the FOV that may obscure the aberration signature in the phase image. The interference patterns are removed using: Peak local maxima (PLM)² for peak detection in real space using Normalized Cross-Correlation (NCC)³ with a kernel cropped from the highest peak in V . The neighboring voxels around the detected puncta peaks are masked off, creating a volume, S . The OTF with interference removed, τ' , can now be obtained as well as a real space reconstructed volume, V' , via inverse FFT,

$$M = \text{PLM}(\text{NCC}(V)) \quad (20)$$

$$S = V \times M \quad (21)$$

$$\tau = \frac{\mathcal{F}(V)}{\mathcal{F}(S)} \quad (22)$$

$$V' = \mathcal{F}^{-1}(\tau) \quad (23)$$

The phase $\varphi(k_z)$ at each k_z plane is then given by the unwrapped phase of τ at that plane (Supplementary Fig. S4b,d). We calculate the three phase embeddings in the same manner as our amplitude embedding such that:

$$\varphi_1 = \varphi_{k_z=0} \quad (24)$$

$$\varphi_2 = \frac{1}{5} \sum_{i=0}^4 \varphi_{k_z=i} \quad (25)$$

$$\varphi_3 = \frac{1}{5} \sum_{i=5}^9 \varphi_{k_z=i} \quad (26)$$

Combining the six planes together, we define the input to the model as a Fourier embedding,

$$\mathcal{E} = \{\alpha_1, \alpha_2, \alpha_3, \varphi_1, \varphi_2, \varphi_3\} \quad (27)$$

A notable advantage of this approach is that, although the signal from each individual CCP is weak, those in the same isoplanatic region contain near-identical spatial frequency distributions which add together to yield Fourier embeddings of high signal-to-noise ratio (SNR) suitable for accurate inference of the underlying aberration (Supplementary Fig. S6).

4.8 AOVIFT: Adaptive Optical Vision Fourier Transformer

Below, we outline the key components of AOVIFT, which uses a 3D multistage vision transformer architecture. This model efficiently captures Fourier-domain features at multiple spatial scales, enabling robust aberration prediction.

4.8.1 Multistage. Recent advances in attention-based transformers have demonstrated scalability, generalizability, and multi-modality for a range of computer vision applications [20–24].

Multiscale (or hierarchical) vision transformers such as Swin [25], and MViT [26] are designed with specialized modules (e.g., shifted-window partitioning [25], and hybrid window attention [27]) to excel at a variety of detection tasks for 2D natural images using supervised training on ImageNet [28]. Although these variants are

²https://scikit-image.org/docs/stable/auto_examples/segmentation/plot_peak_local_max.html

³https://scikit-image.org/docs/stable/auto_examples/registration/plot_masked_register_translation.html

more efficient than their ViT counterparts in terms of FLOPs and number of parameters, they often incorporate specialized modules as noted above. Hiera [29] showed that these designs can be streamlined without performance loss by leveraging large-scale self-supervised pretraining.

Current multi-scale architectures use a Feature Pyramid Network scheme [30]—downsampling the spatial resolution of the image for each stage while expanding the embedding size for deeper layers. Instead, in our work, we use Ω stages and do not downsample during any of the stages, but rather select different patch sizes for each stage (Fig. 1). This allows the embedding dimension within each stage to be fixed to the number of voxels in the patch of that stage, rather than expanding with increasing depth as in some hierarchical models.

4.8.2 Patch encoding. The input to the model is the Fourier Embedding, a 3D tensor $\mathcal{E} \in \mathbb{R}^{\ell \times d \times d}$, where $\ell=6$ is the number of 2D planes each with a height and width of d . For each model stage, i , patchifying begins by dividing the input tensor \mathcal{E} into non-overlapping 2D tiles (each $p_i \times p_i$) that are each flattened into a 1D patch for a total of k_i patches in a plane. After patchifying, the input tensor is transformed into $x_p \in \mathbb{R}^{\ell \times k_i \times p_i^2}$ (Fig. 1b).

The initial ViT model uses a set of consecutive transformer layers with a fixed patch size for all transformers, where each transformer layer can capture local and global dependencies between patches via self-attention [20]. The computation needed for the self-attention layers scales quadratically *w.r.t.* the number of patches (i.e., sequence length). While using a smaller patch size could be useful to capture visual patterns at a finer resolution, using a large patch size is computationally cheaper.

Our baseline model uses a two-stage design with patch sizes of 32 and 16 pixels, respectively (Fig. 1c). Appendix A shows an ablation study using several stages with patch sizes ranging between 8 and 32 pixels.

4.8.3 Positional encoding. Rather than adopting the Cartesian positional encoding of ViT [20], we use a polar coordinate system (r, θ) to encode the position of each patch. This choice is motivated by the radial symmetries of the Zernike polynomials and the efficiencies gained in NeRF [31], coordinate-based MLPs [32], and RoFormer [33]. For a given plane in \mathcal{E} (Eq. 27), the radial positional encoding vector (*RPE*) is calculated for every patch,

$$\text{RPE}(r, \theta) = [r, \sin \theta, \cos \theta, \dots, \sin m\theta, \cos m\theta] \quad (28)$$

where (r, θ) are the polar coordinates for the center of each patch, and $m = 16$. All patches and their positional encoding are then mapped into a sequence of learnable linear projections $\zeta \in \mathbb{R}^{\ell \times k_i \times p_i^2}$ that we use as our input to the transformer layers in the model.

4.8.4 Transformer building blocks. Each stage has n transformer layers, where each layer has h multi-head attention (MHA) layers that map the inter-dependencies between patches, followed by a multi-layer perceptron block (MLP) that learns the relationship between pixels within a patch. The stage’s embedding size, $\epsilon_i = p_i^2$, is set to match the number of voxels in a patch for that stage. The MLP block is four times wider than the embedding size (Fig. S2c). Layer normalization (LN) [34] is applied before each step, and a

skip/residual connection [35] is added after each step

$$\zeta_1 = \text{LN}(\text{MHA}(\zeta)) + \zeta \quad (29)$$

$$\zeta_2 = \text{LN}(\text{MLP}(\zeta_1)) + \zeta_1 \quad (30)$$

In addition to the skip connections in each transformer layer, we also add a skip connection between the input and output of each stage. We use a dropout rate of 0.1 for each dense layer [36], and stochastic depth rate of 0.1 [37]. The patches from the final stage are pooled using a global average along the last dimension and passed to a fully connected layer to output z Zernike coefficients.

4.8.5 Attention modules. We use self-attention [38] as our default attention module for all transformer layers in our model. Complementary to our approach, recent studies have looked into alternative attention methods to reduce the quadratic scaling of self-attention [23, 39, 40]. Our architecture is compatible with these attention mechanisms, which would further improve our model’s efficiency.

4.9 In-silico evaluations

Appendix A shows an ablation study of our synthetic data simulator (Appendix A.2), our multi-stage design (Appendix A.3), our training dataset size (Appendix A.4, Supplementary Fig. S22), and details of our training hyperparameters (Appendix A.5, Supplementary Table S2, Supplementary Table S8). We also introduce a novel way of measuring prediction confidence of our model using digital rotations in Appendix A.6 (Supplementary Fig. S23).

We present a detailed cost analysis benchmark comparing our architecture with other widely used models like ConvNeXt [41] and ViT [20] in Appendix B. To further diagnose our model’s performance, we carried out a series of experiments to understand our model’s sensitivity to SNR (Appendix C.1, Supplementary Fig. S24–S25), generalizability to other light-sheets (Appendix C.2), number of objects in the FOV (Appendix C.3), and object size (Appendix C.4, Supplementary Fig. S26).

ACKNOWLEDGMENTS

We thank X. Ruan, M. Mueller, P. Zwart, and H. York for helpful discussions and comments. SUM159 cells used in this study were a gift from Kirchhausen Lab. We thank N. Shaner for providing the mChlida fluorescent protein plasmid to I.A.S., which was used to generate reagents for this study. We gratefully acknowledge the support of this work by the Laboratory Directed Research and Development (LDRD) Program of Lawrence Berkeley National Laboratory under US Department of Energy contract No. DE-AC02-05CH11231. We thank J. White for managing our computing cluster. T.A., G.L., F.G., J.L.H. and S.U. are partially funded by the Philomathia Foundation (awarded to E.B. and S.U.). T.A. and G.L. are partially funded by the Chan Zuckerberg Initiative (awarded to S.U.). T.A. and S.U. are partially supported by Lawrence Berkeley National Laboratory’s LDRD program 7647437 and 7721359 (awarded to S.U.). T.A., D.E.M., and E.B. are funded by HHMI (awarded to E.B.). C. Shirazinnejad and D.G.D. are partially supported by NIH Grant R35GM118149 (awarded to D.G.D.). Cat Simmons, I.S.A., and I.A.S. are partially supported by NIH Grant 1R01DC021710 (awarded to I.A.S.). F.G. is partially funded by the Feodor Lynen Research Fellowship, Humboldt Foundation. S.U. is funded by the Chan Zuckerberg Initiative

Imaging Scientist program 2019-198142 and 2021-244163. E.B. is an HHMI Investigator. S.U. is a Chan Zuckerberg Biohub – San Francisco Investigator.

DECLARATIONS

Author contribution. T.A. designed models, developed training pipelines and evaluation benchmarks. D.E.M. designed the preprocessing algorithms and developed the microscope software for the imaging experiments. T.A. and D.E.M. designed Fourier embedding, and developed the synthetic data generator for training and validation. C. Shirazinnejad, C. Simmons, I.S.A., S.E.W., N.H., E. Hong, E. Huang, E.S.B., A.N.K., D.G.D., and I.A.S. generated the zebrafish reagents. A.N.K., prepared the cultured SUM159 cells. C. Shirazinnejad, J.L.H., K.A., and A.M.J. prepared samples. G.L. and J.L.H. performed the imaging experiments with zebrafish. J.L.H. and K.A. performed the imaging experiments with cells. G.L., K.A. and F.G. performed the imaging experiments with beads. T.A., D.E.M., and S.U. performed analysis and prepared figures. T.A. wrote the manuscript with input from all co-authors. D.E.M., E.B. and S.U. edited the manuscript. T.A., E.B. and S.U. supervised the project.

Data availability. Data for demos is available on our Github repository at <https://github.com/cell-observatory/aovift>. The full datasets for training and testing are too large to be hosted on public repositories, they can be shared upon reasonable request.

Code availability. Source code for training and evaluation (and all pretrained models) are available at <https://github.com/cell-observatory/aovift>. Docker image is available at <https://github.com/cell-observatory/aovift/pkgs/container/aovift>. Deconvolution was performed using PetaKit5D(<https://github.com/abcuberkeley/PetaKit5D>).

Ethics approval and consent to participate. All experiments with zebrafish were done in accordance with protocols approved by the University of California, Berkeley’s Animal Care and Use Committee and following standard protocols (animal use protocol number AUP-2019-09-12560-1). All zebrafish used in this study were embryos younger than 72hpf. Sex determination was not a factor in our experiments. All husbandry and experiments with zebrafish were done in accordance with protocols approved by the University of California, Berkeley’s Animal Care and Use Committee and following standard protocols (animal use protocol numbers AUP-2019-09-12560-1 (Upadhyayula Lab), AUP-2020-10-13737-1 (Swinburne Lab), and AUP-2021-05-14347-1 (Zebrafish Facility Core Protocol)).

Conflict of interest/Competing interests. None.

REFERENCES

- [1] Qinrong Zhang, Qi Hu, Caroline Berlage, Peter Kner, Benjamin Judkewitz, Martin Booth, and Na Ji. Adaptive optics for optical microscopy. *Biomed. Opt. Express*, 14(4):1732–1756, Apr 2023.
- [2] Kai Wang, Daniel E Milkie, Ankur Saxena, Peter Engerer, Thomas Misgeld, Marianne E Bronner, Jeff Mumm, and Eric Betzig. Rapid adaptive optical recovery of optimal resolution over large volumes. *nature methods*, 11(6):625–628, 2014.
- [3] Tsung-Li Liu, Srigokul Upadhyayula, Daniel E Milkie, Ved Singh, Kai Wang, Ian A Swinburne, Kishore R Mosaliganti, Zach M Collins, Tom W Hiscock, Jamien Shea, et al. Observing the cell in its native state: Imaging subcellular dynamics in multicellular organisms. *Science*, 360(6386):eaq1392, 2018.
- [4] Debayan Saha, Uwe Schmidt, Qinrong Zhang, Aurelien Barbotin, Qi Hu, Na Ji, Martin J Booth, Martin Weigert, and Eugene W Myers. Practical sensorless aberration estimation for 3d microscopy with deep learning. *Optics express*, 28(20):29044–29053, 2020.
- [5] Mani Ratnam Rai, Chen Li, H. Troy Ghashghaei, and Alon Greenbaum. Deep learning-based adaptive optics for light sheet fluorescence microscopy. *Biomed. Opt. Express*, 14(6):2905–2919, Jun 2023.
- [6] Peiyi Zhang, Donghan Ma, Xi Cheng, Andy Tsai, Yu Tang, Hao-Cheng Gao, Li Fang, Cheng Bi, Gary Landreth, Alexander Chubykin, and Fang Huang. Deep learning-driven adaptive optics for single-molecule localization microscopy. *Nature Methods*, 20(3), 2023.
- [7] Qi Hu, Martin Hailstone, Jingyu Wang, Matthew Wincott, Danail Stoychev, Huriye Atilgan, Dalia Gala, Tai Chaiamarit, Richard M. Parton, Jacopo Antonello, Adam M. Packer, Ilan Davis, and Martin J. Booth. Universal adaptive optics for microscopy through embedded neural network control. *Light: Science & Applications*, 12(1):270, 2023.
- [8] Iksung Kang, Qinrong Zhang, Stella X. Yu, and Na Ji. Coordinate-based neural representations for computational adaptive optics in widefield microscopy. *Nature Machine Intelligence*, 6(6):714–725, Jun 2024.
- [9] Ashesh Ashesh, Federico Carrara, Igor Zubarev, Vera Galinova, Melisande Croft, Melissa Pezzotti, Daozheng Gong, Francesca Casagrande, Elisa Colombo, Stefania Giussani, et al. Microsplit: Semantic unmixing of fluorescent microscopy data. *bioRxiv*, pages 2025–02, 2025.
- [10] Virendra N Mahajan. Strehl ratio for primary aberrations: some analytical results for circular and annular pupils. *Journal of the Optical Society of America*, 72(9):1258–1266, 1982.
- [11] Julie Bentley and Craig Olson. *Field Guide to Lens Design*. SPIE Press, 2012.
- [12] B. M. Hanser, M. G. L. Gustafsson, D. A. Agard, and J. W. Sedat. Phase-retrieved pupil functions in wide-field fluorescence microscopy. *Journal of Microscopy*, 216(1):32–48, 2004.
- [13] Eric Betzig. A cell observatory to reveal the subcellular foundations of life. *Nature methods*, pages 1–4, 2024.
- [14] François Aguet, Srigokul Upadhyayula, Raphaël Gaudin, Yi-ying Chou, Emanuele Cocucci, Kangmin He, Bi-Chang Chen, Kishore Mosaliganti, Mithun Pasham, Wesley Skillern, et al. Membrane dynamics of dividing cells imaged by lattice light-sheet microscopy. *Molecular biology of the cell*, 27(22):3418–3435, 2016.
- [15] Xiongtao Ruan, Matthew Mueller, Gaoxiang Liu, Frederik Görlitz, Tian-Ming Fu, Daniel E Milkie, Joshua L Lillvis, Alexander Kuhn, Johnny Gan Chong, Jason Li Hong, et al. Image processing tools for petabyte-scale light sheet microscopy data. *Nature Methods*, pages 1–11, 2024.
- [16] Heather I. Campbell, Sijiong Zhang, Alan H. Greenaway, and Sergio Restaino. Generalized phase diversity for wave-front sensing. *Opt. Lett.*, 29(23):2707–2709, Dec 2004.
- [17] Vasudevan Lakshminarayanan and Andre Fleck. Zernike polynomials: A guide. *Journal of Modern Optics*, 58(7):545–561, 2011.
- [18] Gaoxiang Liu, Xiongtao Ruan, Daniel E Milkie, Frederik Görlitz, Matthew Mueller, Wilmene Hercule, Alison Killilea, Eric Betzig, and Srigokul Upadhyayula. Characterization, comparison, and optimization of lattice light sheets. *Science Advances*, 9(13):ead6623, 2023.
- [19] Kenneth S Lomax. Business failures: Another example of the analysis of failure data. *Journal of the American statistical association*, 49(268):847–852, 1954.
- [20] Alexey Dosovitskiy, Lucas Beyer, Alexander Kolesnikov, Dirk Weissenborn, Xi-aohua Zhai, Thomas Unterthiner, Mostafa Dehghani, Matthias Minderer, Georg Heigold, Sylvain Gelly, Jakob Uszkoreit, and Neil Houlsby. An image is worth 16x16 words: Transformers for image recognition at scale. *International Conference on Learning Representations*, 2021.
- [21] Nicolas Carion, Francisco Massa, Gabriel Synnaeve, Nicolas Usunier, Alexander Kirillov, and Sergey Zagoruyko. End-to-end object detection with transformers. In *European conference on computer vision*, pages 213–229. Springer, 2020.
- [22] Anurag Arnab, Mostafa Dehghani, Georg Heigold, Chen Sun, Mario Lučić, and Cordelia Schmid. Vivit: A video vision transformer. In *Proceedings of the IEEE/CVF international conference on computer vision*, pages 6836–6846, 2021.
- [23] Bowen Cheng, Ishan Misra, Alexander G Schwing, Alexander Kirillov, and Rohit Girdhar. Masked-attention mask transformer for universal image segmentation. In *Proceedings of the IEEE/CVF conference on computer vision and pattern recognition*, pages 1290–1299, 2022.
- [24] Kaiming He, Xinlei Chen, Saining Xie, Yanghao Li, Piotr Dollár, and Ross Girshick. Masked autoencoders are scalable vision learners. In *Proceedings of the IEEE/CVF conference on computer vision and pattern recognition*, pages 16000–16009, 2022.
- [25] Ze Liu, Yutong Lin, Yue Cao, Han Hu, Yixuan Wei, Zheng Zhang, Stephen Lin, and Baining Guo. Swin transformer: Hierarchical vision transformer using shifted windows. In *Proceedings of the IEEE/CVF international conference on computer vision*, pages 10012–10022, 2021.

- [26] Haoqi Fan, Bo Xiong, Karttikeya Mangalam, Yanghao Li, Zhicheng Yan, Jitendra Malik, and Christoph Feichtenhofer. Multiscale vision transformers. In *Proceedings of the IEEE/CVF international conference on computer vision*, pages 6824–6835, 2021.
- [27] Yanghao Li, Chao-Yuan Wu, Haoqi Fan, Karttikeya Mangalam, Bo Xiong, Jitendra Malik, and Christoph Feichtenhofer. Mvnet2: Improved multiscale vision transformers for classification and detection. In *Proceedings of the IEEE/CVF Conference on Computer Vision and Pattern Recognition*, pages 4804–4814, 2022.
- [28] Jia Deng, Wei Dong, Richard Socher, Li-Jia Li, Kai Li, and Li Fei-Fei. Imagenet: A large-scale hierarchical image database. In *2009 IEEE Conference on Computer Vision and Pattern Recognition*, pages 248–255, 2009.
- [29] Chaitanya Ryali, Yuan-Ting Hu, Daniel Bolya, Chen Wei, Haoqi Fan, Po-Yao Huang, Vaibhav Aggarwal, Arkabandhu Chowdhury, Omid Poursaeed, Judy Hoffman, et al. Hiera: A hierarchical vision transformer without the bells-and-whistles. In *International Conference on Machine Learning*, pages 29441–29454. PMLR, 2023.
- [30] Tsung-Yi Lin, Piotr Dollár, Ross Girshick, Kaiming He, Bharath Hariharan, and Serge Belongie. Feature pyramid networks for object detection. In *Proceedings of the IEEE conference on computer vision and pattern recognition*, pages 2117–2125, 2017.
- [31] Ben Mildenhall, Pratul P. Srinivasan, Matthew Tancik, Jonathan T. Barron, Ravi Ramamoorthi, and Ren Ng. Nerf: representing scenes as neural radiance fields for view synthesis. *Commun. ACM*, 65(1):99–106, dec 2021.
- [32] Matthew Tancik, Pratul Srinivasan, Ben Mildenhall, Sara Fridovich-Keil, Nithin Raghavan, Utkarsh Singhal, Ravi Ramamoorthi, Jonathan Barron, and Ren Ng. Fourier features let networks learn high frequency functions in low dimensional domains. In H. Larochelle, M. Ranzato, R. Hadsell, M. F. Balcan, and H. Lin, editors, *Advances in Neural Information Processing Systems*, volume 33, pages 7537–7547. Curran Associates, Inc., 2020.
- [33] Jianlin Su, Murtadha Ahmed, Yu Lu, Shengfeng Pan, Wen Bo, and Yunfeng Liu. Roformer: Enhanced transformer with rotary position embedding. *Neurocomputing*, 568:127063, 2024.
- [34] Lei Jimmy Ba, Jamie Ryan Kiros, and Geoffrey E. Hinton. Layer normalization. *CoRR*, abs/1607.06450, 2016.
- [35] Kaiming He, Xiangyu Zhang, Shaoqing Ren, and Jian Sun. Deep residual learning for image recognition. In *Proceedings of the IEEE conference on computer vision and pattern recognition*, pages 770–778, 2016.
- [36] Nitish Srivastava, Geoffrey Hinton, Alex Krizhevsky, Ilya Sutskever, and Ruslan Salakhutdinov. Dropout: A simple way to prevent neural networks from overfitting. *Journal of Machine Learning Research*, 15(1):1929–1958, 2014.
- [37] Gao Huang, Yu Sun, Zhuang Liu, Daniel Sedra, and Kilian Q Weinberger. Deep networks with stochastic depth. In *Computer Vision—ECCV 2016: 14th European Conference, Amsterdam, The Netherlands, October 11–14, 2016, Proceedings, Part IV 14*, pages 646–661. Springer, 2016.
- [38] Ashish Vaswani, Noam Shazeer, Niki Parmar, Jakob Uszkoreit, Llion Jones, Aidan N Gomez, Łukasz Kaiser, and Illia Polosukhin. Attention is all you need. In I. Guyon, U. V. Luxburg, S. Bengio, H. Wallach, R. Fergus, S. Vishwanathan, and R. Garnett, editors, *Advances in Neural Information Processing Systems*, volume 30. Curran Associates, Inc., 2017.
- [39] Tri Dao, Dan Fu, Stefano Ermon, Atri Rudra, and Christopher Ré. Flashattention: Fast and memory-efficient exact attention with io-awareness. *Advances in Neural Information Processing Systems*, 35:16344–16359, 2022.
- [40] Jianwei Yang, Chunyuan Li, Xiyang Dai, and Jianfeng Gao. Focal modulation networks. *Advances in Neural Information Processing Systems*, 35:4203–4217, 2022.
- [41] Zhuang Liu, Hanzi Mao, Chao-Yuan Wu, Christoph Feichtenhofer, Trevor Darrell, and Saining Xie. A convnet for the 2020s. In *Proceedings of the IEEE/CVF conference on computer vision and pattern recognition*, pages 11976–11986, 2022.
- [42] Diederik P. Kingma and Jimmy Ba. Adam: A method for stochastic optimization. In Yoshua Bengio and Yann LeCun, editors, *3rd International Conference on Learning Representations, ICLR 2015, San Diego, CA, USA, May 7-9, 2015, Conference Track Proceedings*, 2015.
- [43] Ilya Loshchilov and Frank Hutter. Decoupled weight decay regularization. In *International Conference on Learning Representations*, 2019.
- [44] Yang You, Jing Li, Sashank Reddi, Jonathan Hseu, Sanjiv Kumar, Srinadh Bhojanapalli, Xiaodan Song, James Demmel, Kurt Keutzer, and Cho-Jui Hsieh. Large batch optimization for deep learning: Training bert in 76 minutes. *International Conference on Learning Representations*, 2020.
- [45] Ilya Loshchilov and Frank Hutter. SGDR: Stochastic gradient descent with warm restarts. In *International Conference on Learning Representations*, 2017.
- [46] Yarín Gal and Zoubin Ghahramani. Dropout as a bayesian approximation: Representing model uncertainty in deep learning. In Maria Florina Balcan and Kilian Q. Weinberger, editors, *Proceedings of The 33rd International Conference on Machine Learning*, volume 48 of *Proceedings of Machine Learning Research*, pages 1050–1059, New York, New York, USA, 20–22 Jun 2016. PMLR.
- [47] Martín Abadi, Paul Barham, Jianmin Chen, Zhifeng Chen, Andy Davis, Jeffrey Dean, Matthieu Devin, Sanjay Ghemawat, Geoffrey Irving, Michael Isard, Manjunath Kudlur, Josh Levenberg, Rajat Monga, Sherry Moore, Derek G. Murray, Benoit Steiner, Paul Tucker, Vijay Vasudevan, Pete Warden, Martin Wicke, Yuan Yu, and Xiaoqiang Zheng. Tensorflow: A system for large-scale machine learning. In *Proceedings of the 12th USENIX Conference on Operating Systems Design and Implementation*, OSDI 16, pages 265–283, USA, 2016. USENIX Association.
- [48] Xiaohua Zhai, Alexander Kolesnikov, Neil Houlsby, and Lucas Beyer. Scaling vision transformers. In *Proceedings of the IEEE/CVF conference on computer vision and pattern recognition*, pages 12104–12113, 2022.
- [49] Sanghyun Woo, Shoubhik Debnath, Ronghang Hu, Xinlei Chen, Zhuang Liu, In So Kweon, and Saining Xie. Convnext v2: Co-designing and scaling convnets with masked autoencoders. In *Proceedings of the IEEE/CVF Conference on Computer Vision and Pattern Recognition*, pages 16133–16142, 2023.
- [50] Mark Sandler, Andrew Howard, Menglong Zhu, Andrey Zhmoginov, and Liang-Chieh Chen. MobileNetV2: Inverted residuals and linear bottlenecks. In *Proceedings of the IEEE conference on computer vision and pattern recognition*, pages 4510–4520, 2018.
- [51] Mostafa Dehghani, Yi Tay, Anurag Arnab, Lucas Beyer, and Ashish Vaswani. The efficiency misnomer. In *International Conference on Learning Representations*, 2022.
- [52] K Hoshijima, MJ Juryneć, and DJ Grunwald. Precise genome editing by homologous recombination. In *Methods in cell biology*, volume 135, pages 121–147. Elsevier, 2016.
- [53] Kazuyuki Hoshijima, Michael J Juryneć, and David Jonah Grunwald. Precise editing of the zebrafish genome made simple and efficient. *Developmental cell*, 36(6):654–667, 2016.
- [54] Jose Arturo Gutierrez-Triana, Tinatini Tavhelidse, Thomas Thumberger, Isabelle Thomas, Beate Wittbrodt, Tanja Kellner, Kerim Anlas, Erika Tsingos, and Joachim Wittbrodt. Efficient single-copy HDR by 5′ modified long dsDNA donors. *Elife*, 7:e39468, 2018.
- [55] Miguel A Moreno-Mateos, Charles E Vejnar, Jean-Denis Beaudoin, Juan P Fernandez, Emily K Mis, Mustafa K Khokha, and Antonio J Giraldez. Crisprscan: designing highly efficient sgRNAs for CRISPR-Cas9 targeting in vivo. *Nature methods*, 12(10):982–988, 2015.
- [56] Magnus Wang and Antonio Marin. Characterization and prediction of alternative splice sites. *Gene*, 366(2):219–227, 2006.
- [57] Brian A Rabe and Constance Cepko. A simple enhancement for Gibson isothermal assembly. *bioRxiv*, pages 2020–06, 2020.
- [58] Allon M Klein, Linas Mazutis, Ilke Akartuna, Naren Tallapragada, Adrian Veres, Victor Li, Leonid Peshkin, David A Weitz, and Marc W Kirschner. Droplet barcoding for single-cell transcriptomics applied to embryonic stem cells. *Cell*, 161(5):1187–1201, 2015.
- [59] Richard Mark White, Anna Sessa, Christopher Burke, Teresa Bowman, Jocelyn LeBlanc, Craig Ceol, Caitlin Bourque, Michael Dovey, Wolfram Goessling, Caroline Erter Burns, et al. Transparent adult zebrafish as a tool for in vivo transplantation analysis. *Cell stem cell*, 2(2):183–189, 2008.

Appendices

APPENDICES

A	Ablation study	16
A.1	Fourier embedding design	16
A.2	Synthetic training and validation data	16
A.3	Multistage design	16
A.4	Training dataset size	17
A.5	Training hyperparameters	17
A.6	Measuring prediction confidence	17
B	Architecture benchmark	18
B.1	Baseline models	18
B.2	Cost analysis	18
C	In-silico evaluations	19
C.1	Sensitivity to SNR	19
C.2	Generalization to other light sheets	19
C.3	Sensitivity to the density of objects	19
C.4	Sensitivity to object size	20
D	Genome editing of ap2s1 for Zebrafish	20

A ABLATION STUDY

A.1 Fourier embedding design

Most ML approaches to AO rely on real-space representations of training data [4–8]. However, open-source AO training datasets remain scarce, and acquiring large, annotated 3D volumes that capture diverse biological features over a broad aberration space is prohibitively expensive. Training on small datasets leads to overfitting and poor generalization; scaling existing 2D models to 3D also comes at significant computational cost.

To address these challenges, we use synthetic data transformed to the Fourier domain. We embed diffraction-limited puncta (such as signal from sub-diffractive beads or fluorescent protein labeled AP2) into Fourier space using a pre-processing step (see Sec. 4.7). Within an isoplanatic patch, the aberration affects signal from all emitters, yielding a consistent Fourier ‘fingerprint’. As shown in Supplementary Fig. S4a,b, and demonstrated in noise-free Fourier principal planes (Supplementary Fig. S5), the amplitude and phase embedding planes contain unique signatures for each Zernike mode. To illustrate the similarity of aberration-specific patterns across a variety of real-space samples, we apply $0.1 \mu\text{m}$ RMS of coma Z_3^{-1} to three different examples: a single bead (Supplementary Fig. S6a), a volume with five synthetic beads resembling training data (spanning $9.3 \times 9.3 \times 12.8 \mu\text{m}^3$, Supplementary Fig. S6b), and a volume of 100 synthetic beads resembling an AP2-labeled zebrafish embryo (corresponding to density beyond the parameters of the training data, Supplementary Fig. S6c). Despite drastic differences in real-space appearance, the Fourier embeddings ($\alpha_1, \alpha_2, \alpha_3, \varphi_1, \varphi_2, \varphi_3$) remain consistent.

In contrast, real-space models trained on limited data (e.g., a few synthetic beads) did not generalize on dense puncta, where isolating individual features is difficult and aberrations are spatially variable. By moving to the Fourier domain, we leverage the OTF, which bounds the frequency space. Despite never seeing more than five beads during training, our model generalizes to volumes with

100+ resolvable puncta because each Zernike pattern persists in Fourier space (Appendix C.3) regardless of the real-space density.

Beyond generalization, Fourier embeddings reduces the inference cost by compressing the original isoplanatic patch from $D \times H \times W$ to $6 \times 64 \times 64$ voxels. A real-space model operating on 64^3 voxels requires more than ten times the computation. Further downsampling (to $6 \times 32 \times 32$) accelerates inference but loses sensitivity to discriminate subtle changes in aberrations. Conversely, scaling up to $6 \times 128 \times 128$ yields minimal gains for the first 15 Zernike modes, although may be necessary for higher-order modes.

During preprocessing, we also normalize phase embeddings to remove interference patterns introduced by sample structures (Supplementary Fig. S7d,e). Without phase information, the model cannot recover aberration signs, since amplitude alone lacks sign encoding (Supplementary Fig. S7f,g). While the principle amplitude (α_1) and phase (φ_1) planes capture lateral aberrations, additional planes (α_2, α_3 & φ_2, φ_3) are necessary for axial distortions (e.g., spherical aberrations Z_3^{-1} , Supplementary Fig. S7f). To capture such aberrations, we average a small set of planes along \hat{k}_z -axis, rather than using the orthogonal principal planes, to improve the model generalizability. A single model trained on the principal plane plus additional \hat{k}_z -axis planes then generalized across diverse lightsheet configurations with distinct axial support (Appendix C.2), enabling robust aberration prediction under varied imaging setups.

A.2 Synthetic training and validation data

We used the synthetic data generator described in Sec. 4.6 to create training and testing data for the first 15 Zernike modes, Z_0^0 through $Z_4^{\pm 4}$ (Supplementary Fig. S1). We show the λ RMS magnitude range for our training (blue) and testing (orange) distributions in Supplementary Fig. S21a. The panels show an example wavefront and a breakdown of each distribution: single (Supplementary Fig. S21b), bimodal (Supplementary Fig. S21c), Powerlaw—a heavy-tailed distribution with a few dominating modes (Supplementary Fig. S21d), and Dirichlet—uniform weighting across all modes (Supplementary Fig. S21e).

To train our models, we created two millions synthetic 3D volumes with aberrations ranging between 0.0 to 0.5λ RMS. Each volume can have up to five beads with a uniform distribution of photons ranging between 1 and 200,000 integrated photons per bead.

We created a separate dataset with 100,000 volumes for testing. This smaller dataset extended the aberration magnitude up to 1.0λ RMS, and the SNR range to 500,000 integrated photons. We also simulated samples with much higher object density (up to 150 objects in any given volume). We sample from this dataset to carry out individual test experiments described in Appendix C to stress test our models.

A.3 Multistage design

We used Fourier embedding ($\mathcal{E} \in \mathbb{R}^{\ell \times d \times d}$) as input to a vision transformer model with Ω stages (Supplementary Fig. S2a). For each stage, the ℓ Fourier planes are tiled into k patches (Supplementary Fig. S2b), applying the radial encoded Positional Embedding to each patch. These are passed through a sequence of n Transformer

(Supplementary Fig. S2c) layers, each consisting of h parallel multi-head attention layers (MHA), followed by a multi-layer perceptron block (MLP). At each stage end, a residual connection is added, and the patches are merged back into the shape matching the stage input (Merge patches). After all stages, the resulting patches are pooled (GlobalAvgPool) and connected with a dense layer to output the z Zernike coefficients.

To determine the optimal number of stages for our architecture, we designed several models by changing the number of transformer layers n used for each patch size p , while keeping the total number of transformer layers used in each model to 8, and choosing a patch size from $p_1 = 32$, $p_2 = 16$, or $p_3 = 8$.

Supplementary Fig. S3 shows our performance analysis of each model trained on the same dataset of 2 million synthetically generated samples. We created two models using a triple-stage design in Supplementary Fig. S3a, and three models using a dual-stage design in Supplementary Fig. S3b. We used 8 transformers for each model, but we vary the number of transformers used for each patch size.

The cost of running our triple-stage models is lower than our dual-stage models in terms of GFLOPs (Supplementary Fig. S3c), and both of our triple-stage models are smaller than the rest of the models we tested (Supplementary Fig. S3d). However, our dual-stage models converged to a better training loss, and were substantially faster in terms of training (Supplementary Fig. S3f), and inference (Supplementary Fig. S3h–k).

In general, using smaller patch sizes is more expensive, as the compute for self-attention layers scales quadratically *w.r.t.* the number of patches. Our analysis suggests that the smallest patch size $p_3 = 8$ is not necessary for our application, which is expected given that our starting input images are relatively small. Furthermore, the models that use more transformers for the biggest patch size ($p_1 = 32$) are faster, and perform better in terms of training loss. Given that most aberrations extend beyond (16×16) pixels in Fourier space, we chose a dual-stage layout with an equal number of transformers for each patch size ($p_1 = 32, p_2 = 16$) to balance between accuracy and training/inference time.

In all, we derived five variants—scaling the model size from 34 million up to 228 million parameters. Supplementary Table S2 shows the number of transformer layers n , number of heads h , embedding size ϵ , and MLP size x , highlighting the hyperparameters used to create each of our variants. Further evaluation for all variants of our model can be found in Appendix B—where they are also compared to other prominent architectures.

A.4 Training dataset size

In this section, we present a small case study to understand the scaling of our models in terms of model size, and training dataset size. For simplicity, we chose two models for this analysis: Tiny (T) and Small (S). We trained each model on a synthetic dataset that has up to eight million samples.

Supplementary Fig. S22 shows the cumulative distribution functions for our residuals after a single correction over 10,000 test samples with initial aberrations ranging from 0.2λ RMS up to 0.4λ RMS, simulated with 50,000 up to 200,000 integrated photons using a single bead. The colors indicate the number of training samples

used for each model: 500K (blue), 1M (orange), 2M (green), 4M (red), 6M (purple), and 8M (brown).

The performance of our Tiny model starts to plateau after four million training samples—indicating it saturated its learning capacity given the limited number of trainable parameters that it can adjust during training (Supplementary Fig. S22a). On the other hand, our Small model continued to improve with more training data (Supplementary Fig. S22b). We show an additional analysis, scaling our model size up to 227 million trainable parameters in Appendix B.

A.5 Training hyperparameters

We trained all models on a two million sample dataset of synthetically aberrated beads, described in Sec. 4.6.2. Training uses Adam [42], augmented with decoupled weight decay regularization [43] with weight decay of 0.001, $\beta_1 = 0.9$, $\beta_2 = 0.99$, and a layerwise adaptive rate scaling [44] for faster training using large batch sizes.

We trained all models using a node with eight NVIDIA H100 GPUs for a total of 500 epochs with a two-phase learning rate scheduler—linearly increasing our learning rate from 0 to $1e^{-3}$ over 25 epochs (warmup phase), followed by a cosine decay [45] for the remaining epochs (decay phase). We used mean squared error (MSE) as our loss function with a batch size of 4096 unless otherwise noted. Supplementary Table S8 shows the breakdown of our training configuration.

We applied dropout [36, 46] with probability 0.1 after all Dense layers except the patch encoder layer [20]. We also used stochastic depth regularization with linearly increasing dropout rates and a max dropout rate of 0.1 [37].

We used Tensorflow [47] to implement our models. We derived five variants—scaling the model size from 34 million up to 228 million parameters—to compare our model design with the architectures described below. Supplementary Table S2 highlights the hyperparameters used to create each of our variants.

A.6 Measuring prediction confidence

To validate a single AOViFT prediction, we perform inferences on 361 digitally rotated copies of \mathcal{E} through a range of 0–360 degrees and check if these predictions are self-consistent. For each Zernike mode $Z_n^{m \neq 0}$, there is a known rotational period, $\frac{2\pi}{m}$. Confidence in the prediction of each mode is established when the rotated inferences match the known Zernike modes’ rotational periods, (Supplementary Fig. S23) within a desired tolerance. For rotationally invariant modes (e.g., spherical aberration), the variance of the Zernike amplitude must remain within a tolerance. When the model predictions exceed tolerance, the typical cause is there is not enough information in the data to make an accurate prediction for that mode. This will occur when the underlying sample structure does not have visible puncta (e.g., high spatial frequency content) or the acquisition has too much noise.

Supplementary Fig. S23a shows an example of our pipeline for measuring prediction confidence. The subpanels show the predicted amplitudes for each digital rotation, and a regression fit between the digitally rotated angle and the predicted twin angle to evaluate the variance in the predictions for 360 digital rotations.

Particularly, we show the predicted amplitudes for:

- Supplementary Fig. S23b: Oblique astigmatism ($Z_{n=2}^{m=-2}$, blue), vertical astigmatism ($Z_{n=2}^{m=2}$, orange), and the magnitude for both twin modes in black.
- Supplementary Fig. S23d: Vertical trefoil ($Z_{n=3}^{m=-3}$, blue), oblique trefoil ($Z_{n=3}^{m=3}$, orange), and the magnitude for both twin modes in black.
- Supplementary Fig. S23f: Vertical coma ($Z_{n=3}^{m=-1}$, blue), horizontal coma ($Z_{n=3}^{m=1}$, orange), and the magnitude for both twin modes in black.
- Supplementary Fig. S23h: Oblique quadrafoil ($Z_{n=4}^{m=-4}$, blue), vertical quadrafoil ($Z_{n=4}^{m=4}$, orange), and the magnitude for both twin modes in black.
- Supplementary Fig. S23j: Oblique secondary astigmatism ($Z_{n=4}^{m=-2}$, blue), vertical secondary astigmatism ($Z_{n=4}^{m=2}$, orange), and the magnitude for both twin modes in black.
- Supplementary Fig. S23l: Predicted amplitudes of primary spherical for each digital rotation ($Z_{n=4}^{m=0}$, blue).

Supplementary Fig. S23[c, e, g, i, and k] show the result of our regression fits. If the mean residual error (MSE) of these predicted twin angles exceeds 700 and the magnitude of the mode is above $0.05 \mu \text{ RMS}$, then we flag that prediction as notconfident (e.g., Supplementary Fig. S23c, highlighted in red). We highlight confident predictions in green (e.g., Supplementary Fig. S23e, and Supplementary Fig. S23k). If our MSE for the digital rotations is high but the magnitude of the mode is below $0.05 \mu \text{ RMS}$, then we mark these modes in blue as confident zero predictions (e.g., Supplementary Fig. S23g and Supplementary Fig. S23i). We show the final prediction for each Zernike mode in Supplementary Fig. S23m, and the corresponding wavefront in Supplementary Fig. S23n.

B ARCHITECTURE BENCHMARK

B.1 Baseline models

We compared our model architecture with two widely used backbones, namely transformer-based ViT [20], and convolution-based ConvNeXt [41] as shown in Fig S8.

ViT [20] originally was used for 2D RGB images and later adopted to 2D RGB videos [22]. To compare with our model, we extended the ViT architecture to our use case (3 spatial dimensions) by replacing each transformer layer with a new building block to process 3D volumes. Following the configurations proposed in [48], we created the variants:

- ViT-Small (layers=12, heads=6, EMB=384, MLP=1536),
- ViT-Base (layers=12, heads=12, EMB=768, MLP=3072),
- ViT-Large (layers=24, heads=16, EMB=1024, MLP=4096),

trying both 16 and 32 as the fixed patch size for all transformer layers in the variant. We set the dropout rate to 0.1 for all variants [36, 37].

ConvNeXt [41, 49] was also designed for 2D RGB images and videos. To adopt the model backbone to 3D spatial data, we replaced each 2D convolutional layer with a 3D convolution, without any other modifications to the rest of the architecture. We used a kernel size of (1, 7, 7), a downscale ratio of (1, 2, 2) for each stage, and stochastic depth rate of 0.1 [37]. As described in [41], we create four variants of the model:

- ConvNeXt-Tiny (C=[96, 192, 384, 768], B=[3, 3, 9, 3]),
- ConvNeXt-Small (C=[96, 192, 384, 768], B=[3, 3, 27, 3]),
- ConvNeXt-Base (C=[128, 256, 512, 1024], B=[3, 3, 27, 3]),
- ConvNeXt-Large (C=[192, 384, 768, 1536], B=[3, 3, 27, 3]),

where C is the number of channels, and B is the number of inverted bottleneck blocks [50] for each stage in the model.

B.2 Cost analysis

To evaluate the performance of these models, we used a subsample of our testing dataset with single beads only (Sec. 4.6.3). Particularly, we use 10,000 samples with aberrations ranging between 0.1λ to $0.2\lambda \text{ RMS}$ —simulated with 50,000 to 200,000 photons. For each sample, we made three iterative corrections, measuring the RMS residuals of the aberration after each iteration. We show the median RMS residuals for all samples after two corrections in Supplementary Fig. S8a. All models tested here, except for ConvNeXt-T, were able to reduce the residuals down to the diffraction-limit (i.e., below $\approx 0.075\lambda \text{ RMS}$ or $\lambda/4$ peak-to-valley [10, 11]) using two corrections only. Supplementary Fig. S9 shows the results for all three corrections.

While equivalent accuracy is found between model variants, it is critical to choose the model with the optimal set of trade-offs, rather than using the model with marginally better loss (Supplementary Fig. S8B). Since all models are capable of reducing the aberration down to diffraction-limit with a reasonable number of iterations, we compare these models across three salient factors: floating point operations per second (FLOPs); model size (number of parameters and memory footprint); speed (training time, throughput, and latency).

While our models' FLOPs for training (Supplementary Fig. S8c) and inference (Supplementary Fig. S8i) are slightly higher than ViT/32 because of the overhead of our multistage design, FLOPs

of our models are still better than ViT/16 and ConvNeXt. A model with lower FLOPs does not necessarily mean a better model overall, because the measurement of FLOPs does not factor in relevant details encoded into the architecture like parallelizable operations and the cost of any individual operation for a given hardware [51]. Since all models are trained on the same hardware, we can look at training time to measure the efficiency of these architectures. Our models’ training hours (Supplementary Fig. S8d) are better because our design enables us to use a large batch size for training (Supplementary Fig. S8e), while maintaining a small memory footprint (Supplementary Fig. S8f), and a lower number of trainable parameters (Supplementary Fig. S8j).

ViT uses a fixed patch size for all of its transformer layers. Thus, using a smaller patch size (e.g., ViT/16) will increase the sequence length (i.e., number of patches) being processed by each layer, scaling the computational cost for self-attention quadratically for all transformer layers in the model. Our multistage architecture allows our models to converge faster by learning Fourier patterns from several scales, and also reduces the cost of our models by leveraging cheaper transformer layers with bigger patch sizes.

Unlike ViT, our embedding size ϵ_i changes based on the number of voxels per patch in each stage i . Our initial stage has a patch size $p_1 = 32$, resulting in an embedding size $\epsilon_1 = 1024$. While our second stage uses a smaller patch size $p_2 = 16$, our embedding size $\epsilon_2 = 256$ is significantly smaller, forcing the model to compartmentalize and compress the learnable parameters of deeper layers. Therefore, our transformer layers with smaller patch sizes have a smaller embedding size, instead of keeping the embedding size fixed throughout the model. This design scales particularly well as we increase the model size up by adding transformer layers (Supplementary Fig. S8k), and increasing the number of transformer heads (Supplementary Fig. S8l) for each layer.

In terms of inference speed, we see an advantage of using our models over the other models tested here. Our model variants perform exceptionally well *w.r.t.* throughput—maximum number of predictions per second using a batch size of 1024 (Supplementary Fig. S8g), and latency—average inference time (milliseconds) per image using a single NVIDIA A100 GPU (Supplementary Fig. S8h). Table S3 shows a breakdown of these cost indicators for all models tested here. Based on this analysis, we select our small model for use on experimental data.

C IN-SILICO EVALUATIONS

C.1 Sensitivity to SNR

To test our model’s sensitivity to SNR, we evaluated our Small model on 10,000 test samples using a single bead with a mixed distribution of aberrations of magnitudes up to 1λ RMS. Supplementary Fig. S10a shows the initial aberrations in the test dataset as a function of integrated photons. Supplementary Fig. S10b–f shows five rounds of corrections.

We also show first round corrections for specific single modes of aberrations under low SNR conditions (i.e., $\leq 100,000$ integrated photons) in Supplementary Fig. S24–S25.

Supplementary Fig. S24a shows the residual λ RMS after a single correction for vertical astigmatism $Z_{n=2}^{m=2}$, along with XY MIPs of the residual aberration for various aberration amplitudes and SNR (Supplementary Fig. S24b). Max counts is highlighted above each PSF.

For single mode aberrations of $\leq 0.2 \lambda$ RMS amplitude, the model can reach diffraction-limited performance for as low as 20,000 photons. However, it is exceptionally difficult to get good corrections for large aberrations at this SNR. We see similar trends for vertical trefoil $Z_{n=3}^{m=-3}$ (Supplementary Fig. S24c), vertical coma $Z_{n=3}^{m=-1}$ (Supplementary Fig. S24e), oblique quadrafoil $Z_{n=4}^{m=-4}$ (Supplementary Fig. S25a), oblique secondary astigmatism $Z_{n=4}^{m=-2}$ (Supplementary Fig. S25c), and primary spherical $Z_{n=4}^{m=0}$ (Supplementary Fig. S25e).

C.2 Generalization to other light sheets

To evaluate our model’s generalizability to other light-sheets, we created four synthetic datasets with 10,000 samples each having aberrations up to 1λ RMS—using a single bead with up to 500,000 integrated photons.

Supplementary Fig. S20a–c shows the residuals for three rounds of corrections using the same multi-Bessel LLS as used for generating the training data. The next row (Supplementary Fig. S20d–f) shows the results for a LLS of the same type but at higher NA. It achieves similar performance for the same training set, despite the higher NA.

However, the model’s performance degrades when applied to Sinc (Supplementary Fig. S20j–l), and Gaussian (Supplementary Fig. S20m–o) light sheets, as these have notably different cross-sectional profiles. Supplementary Fig. S20i–v show the excitation profile used to create each LLS *w.r.t.* the length of each LLS in microns. Supplementary Table S6 shows the LLS specifications we used for this test.

C.3 Sensitivity to the density of objects

Our model was trained with up to five simulated beads in any given FOV. However, most experimental data will have dozens if not hundreds of objects in a single volume. Therefore, we evaluated our model on a dataset of 10,000 samples simulated with up to 150 beads to understand its sensitivity to the density of objects (δ nm).

Supplementary Fig. S13 shows the residual λ RMS for five rounds of corrections as a function of the average distance to the nearest bead in that given FOV. The results suggest the model generalizes to a much larger number of objects than it was trained on. The

heatmaps (Supplementary Fig. S13b–f) show continuous improvement over 5 iterations provided there is not much overlap among the objects ($\delta \geq 200\text{nm}$).

C.4 Sensitivity to object size

As mentioned in Sec. 4.6, we simulated individual objects (beads) as Gaussian kernels. We uniformly chose the kernel’s full width at half max (FWHM) for each object between 100nm and 400nm to create our training dataset.

Here, we show a test of the extent to which our model can reliably correct individual aberration modes of 0.3λ RMS amplitude *w.r.t.* object size.

Supplementary Fig. S26a–b shows the residual λ RMS after a single correction using our Small model (S) for vertical astigmatism $Z_{n=2}^{m=2}$ simulated with 50,000 and 100,000 integrated photons, respectively.

We also show representative XY MIPs of these aberrations using bead kernels of FWHM 100nm, 200nm, 300nm, and 400nm, respectively (Supplementary Fig. S26I–IV). We find that as the objects get larger, the unique signature of these aberrations in real space and Fourier space is degraded. Better SNR helps improve correction by detecting smaller fringes in the Fourier embedded input images, but the ability to correct for non diffraction-limited objects still depends on the nature of the aberrations. As a rule of thumb, our model can detect aberrations as long as they are reasonably apparent in the real space images. Supplementary Fig. S26c–f show results for vertical trefoil $Z_{n=3}^{m=-3}$, and vertical coma $Z_{n=3}^{m=-1}$, respectively.

D GENOME EDITING OF AP2S1 FOR ZEBRAFISH

Genome editing of *ap2s1*, *ap2s1:ap2s1-mNeonGreen^{bk800}* in zebrafish was performed using a combination of previously described techniques [52–54]. First, a 2.4 kb DNA fragment that spanned the stop codon of *ap2s1* was cloned from AB wild type genomic DNA (genomic DNA from the AB population at UC Berkeley). The 2.4 kb PCR fragment was designed to include 1.2 kb of the end of *ap2s1* and 1.2 kb downstream of the stop codon that were the homology arms for homology dependent repair. The fragment was sequenced to ensure that the selected guide RNA target was present and lacked any SNPs. The target sequence of the guide RNA used to cut *ap2s1* was ACTGATTGACAGTTTACTCC (identified using the CRISPRscan [55] software, guide RNA synthesized by IDT). The donor did not require any mutations to prevent cutting because the guide target spanned the stop codon of *ap2s1*. The mNeonGreen used was designed and synthesized to minimize predicted RNA splicing donor and acceptor sequences without changing the protein [56]. Isothermal assembly was used to clone a linker and mNeonGreen green sequence before the stop codon of *ap2s1* [57]. The backbone we cloned the genomic fragment into and engineered the donor within contains a set of flanking sequences that we used for both isothermal assembly and PCR of the genome editing donor. These sequences come from the inDrops single-cell transcriptomics library preparation protocol and worked well for efficient PCR (GCATACGAGATCTCTTCCCTACACG, CACGGTCTCGGCATTCTGCTGAAC) [58]. For making an HDR donor for genome editing, oligos with biotin added to the 5’ ends were used to prevent oligomerization upon injection [54]. For embryo injections, 2 nl was injected into the 1–4 cell embryo of our injection recipe: 5 μM guide RNA (purchased from IDT), 50 ng/ μl clean cap Cas9 mRNA (from Trilink), 100 mM KCl, 0.1% phenol red, 0.1 mM EDTA, and 1 mM Tris, pH 7.5. Approximately 3000 embryos were injected by a group of 3–5 lab members. Injected embryos were screened and selected for health, and successful injections as indicated by broad fluorescence signal were raised to adulthood. After 2–3 months, zebrafish were screened for potential founders through germ-line transmission. Embryos with positive signal were established as a new allele once we confirmed by PCR that mNeonGreen had been inserted cleanly at the targeted site in *ap2s1*. Founders were out-crossed with Casper (*mitfa^{w2/w2}*; *mpv17^{a9/a9}*) [59] mutants, and their offspring were crossed with Roy Nacre mutants again to establish the heterozygous *ap2s1-mNeonGreen* and homozygous Casper alleles. These fish were in-crossed and screened for homozygous *ap2s1-mNeonGreen^{bk800/bk800}* embryos for imaging.

DNA Sequences used for zebrafish genome editing and labeling mitochondria

- GCATACGAGATCTCTTCCCTACACG –forward biotinylated primer for generating HDR template by PCR
- tgctaaagtgtactg... –left homology arm
- gggcGatccgggtgatccgggtgatct –GGS linker between Ap2s and mNG polypeptides
- gtTagCaaggcgc... –mNeonGreen through to stop codon
- actgtcaatcagtc... –right homology arm

- **G TTCAGCAGGAATGCCGAGACCGTG** —reverse biotinylated primer for generating HDR template by PCR

GCATACGAGATCTCTTTCCCTACACG tgctaaagttgactgttgagttt
 tacagtgtagtttagtgttttacactatcccaaaaaagctgatcattgttttactaaggcatgt
 gaaatatttattatcgactaaaatattgttattgtgtcaatatgtgagctcatgttttagtatgcc
 attcattttgtcaaaaaataatgaataaaaaaaacatgttttagagagtcagcaagaatatac
 tatgaaacttattagaagcagttaaaaagatcaattcaatatataaaagcaaaaaacatatac
 ggttgaagtcagaattattagcccccttgaattttttttcttttttaataatttcccaaatgatg
 ttaacagagcaaggaaactttcacatatgtctgattatatttttctctggaagagcttctt
 ttgtttatttccgctagaataaaagccatttttaatttttaaacacattttaagacaaaattat
 tagccccctaaaggttaatttttttttttacgatagctacagaacctgttatacaataactg
 gctaattaccctaacctgcctagtttaacctaaatacagcgcatacactctttaaacacg
 catacaaacacacacaattttatttccaaaaaatgttttgaatcccagagatgggttg
 cggccggaaggcctcatcgtgtgttaaaaaatgtctggaataagttggcggttcattccgctgt
 ggcgacccagataataaagggactaagccgacaagaaaatgaatgaacgaatga
 atgttttgaagtttaagttgtgtagaactgctttatagtaagaaatccccaaattgagt
 catgttgcaaacatacattgattaagtttaacttaattgttttgc aaatfaagttgattgga
 actaaagcaatttaatttctctcaaaaacttaagaattgatttagctcaactaacaataaata
 tttttgagtgcaaacacatgtaaaaaatgcacgaagcagcaagtttttagttgaaaacagcg
 gccctatatgtgaactgctattaaagaattgttgatgtgttccaggtgtatacgggtgtg
 acgagatgtttctagcaggagagatcagagaaccagccagcaggaaggtgtcaagcag
 ctctcatgctgcagctccctga **ggcgGatccgggtgatccgggtgatc** gtTagCa
 agggcgaggagGACAATATGGCCTCTCTGCCCGCAACACACGAG
 CTGCATATTTTCGGAAGCATCAAcGGcGTGGATTTTCGATATG
 GTiGGgCAaGGaACTGGAAACCCAAATGAcGGaTACGAGGAA
 CTGAATCTGAAGTCAACCAAGGCGACCTCCAaTTCaCCT
 TGGATTCTcGTiCCCCAtATTGGCTATGGaTTTCATCAaTATC
 TGCCaTAtCCTGAtGGAATGTCAACATTTCAaGCcGCTATGGT
 GGATGGATCTGGCTACCAaGTTCCAcGcACCATGCAaTTTGA
 GGACGGcGCCtccCTGACTGTGAACTACCGCTATACCTACGA
 GGGATCtCATATCAAGGGCGAAGCACAaGtTAAAGGaACAG
 GATTCCCAGCTGAcGGCCCCGTCATGACAAACTCTCTGACC
 GCCGCCGACTGGAGCCGGTCCAAGAAAACTTACCCTAACG
 ATAAGACCATCATCTCTACCTTCAaATGGAGTTATACCACc
 GGCAACGGaAAGCGcTACAGAAGCACAGCCCGAACTACCT
 ATACTTTTGCTAAGCCtATGGCTGCAAACTATCTGAAAAAT
 CAGCCTATGTAtGTcTTCcGAAAaACcGAattgAAGCACTCCAA
 AACAGAACTGAATTTCAAGGAgTGGCAGAAGGCTTTTACC
 GATGTtATGGGcatggagcagctgtacaaAtaaactgtcaatcagtcaaccaacca
 atcaacaaccaccattgtgtcagctccgcccccctgtcagccaagccatagattgt
 gtgtatgagttgtcatgctgaaaatcatccttaacattcaccttttctttacactcgcac
 cacctcacaggatgttgccttctgtctgcaactcatgaatttcgaggcagataagaattc
 gtaaaacttctcgggtatgtgacctgattatcttggcatagccagaattgaattctcagcg
 attttatagcacactagacttcagttttccgactggaagcctcccaagcctgttcattaacac
 taacatagataatagcgtcatgtggc caaaaaactgcatggcacgaaagtgcagtc
 aattgcaagattccgggctgactgcaatatgcaatgagaaaaactgattgtatgcat
 ttaagaaattcccatatgtactatataaaaaagaatcaaatgttaatatgctgactgca
 aataataattgttactgcttctgttttctggtacaagatccatattgttaaaactcaaa
 tacgtaaggtgatcttctgttggtgactatactttttatacaattaagatgttcataatgg
 tgcacaaaaagggttcgcaacaactgtggcacttttgagagtaaaaaaaacatacag
 gcaaaaccaataactgaccgtttcagatggagatgtcattaatccatgaacagttcctgct
 tgccttaactattctgaattgaaaggcgattcgggttaactaatgttaacatggctgctaa
 aaaaagtgtcaatatggaccttctgattctaataagattggaaatgaagataaaacag
 caaatacataaatacattgttattttacatccctcaaaaatggctaccactactgattcgg
 tgggtcctaagaagtgaattaaaattatgtcaacaaaaacatatttttagatccacagc
 ttggccaattgtattcttttggcctattatttttttttctactctaaaaagtaata

atcgggtaatcagcctaagtggaatttaagaaaaatgaaggagaaaacaaaatttcc
 ttgccatactttac **G TTCAGCAGGAATGCCGAGACCGTG**

COX8a-mChilada (mitochondria)

- **ATGCTGGACT...** —cDNA of N-terminal 34 amino acids of *Cox8a*
- **GACAATATGG...** —mChilada
- **ggcGGatccgggtgg** —linker

ATGCTGGACTTCTGAGGGGACTAGCTCGCGTCCGCGCCG
 CTCCGGTTCTGCGGGATCCACGATCACCAGCGAGCCAA
 CCTCGTTACGCGACCCCGGAAG **ggcGGatccgggtgatccgggtgga**
AGCgtTagcaagggcgaggag **GACAATATGGCTATTATCAAAGA**
ATATATGCGTTTTAAAGTtCATATGGAGGGCAGCGTCAATG
GACATGAATTTGAAATTGAGGGcGAGGGAGAGGGCAGGCC
ATTCGAAGGGACTCAGACAGCGAAGTTGAAAGTTACCAAG
GGGGGACCATTGCCATTTGCATGGCACATCTCCCGCCCA
aTTCAATATGGTTCTAAGGCATATGTAAAGCATCTCTGCTG
ATATACCCGATTACTTCAAaCTgTcATTTCCtGAgGGTTTTAC
CTGGGAACCGGAAATGAATTTTGAAGACGGCGGCGTtGTA
ACAGTCACACAGGACTCCAGTCTGCAaGACGGCGAGTTTAT
CTACAAAGTtAAACTTCGTGGAACCAACTTTCCCTCCGACG
GGCCTGTCTATGCAAAAAGAAGACAATGGGGAACACCGCTTC
AACcGAGCGtATGTACCCGGAAGATGGAGCTCTTAAgGGcG
AAACGAAGTGGCGTCTTAAAGTTGAAAGATGGTGGTCACTA
CGAGGCTGAAGTGAAGACCACGTATAAGGCGAAAAAGCC
CGTACAGCTGCCTGGAGCGTACAATGTGGATCGTAAATTG
AAGATAACCTACCATAATGAGGATTACCCATCGTGGAGC
AGTATGAACGAGCCGAGGCTCGGCACTCAACGGGTggcatg
acgagctgtacaagtaA

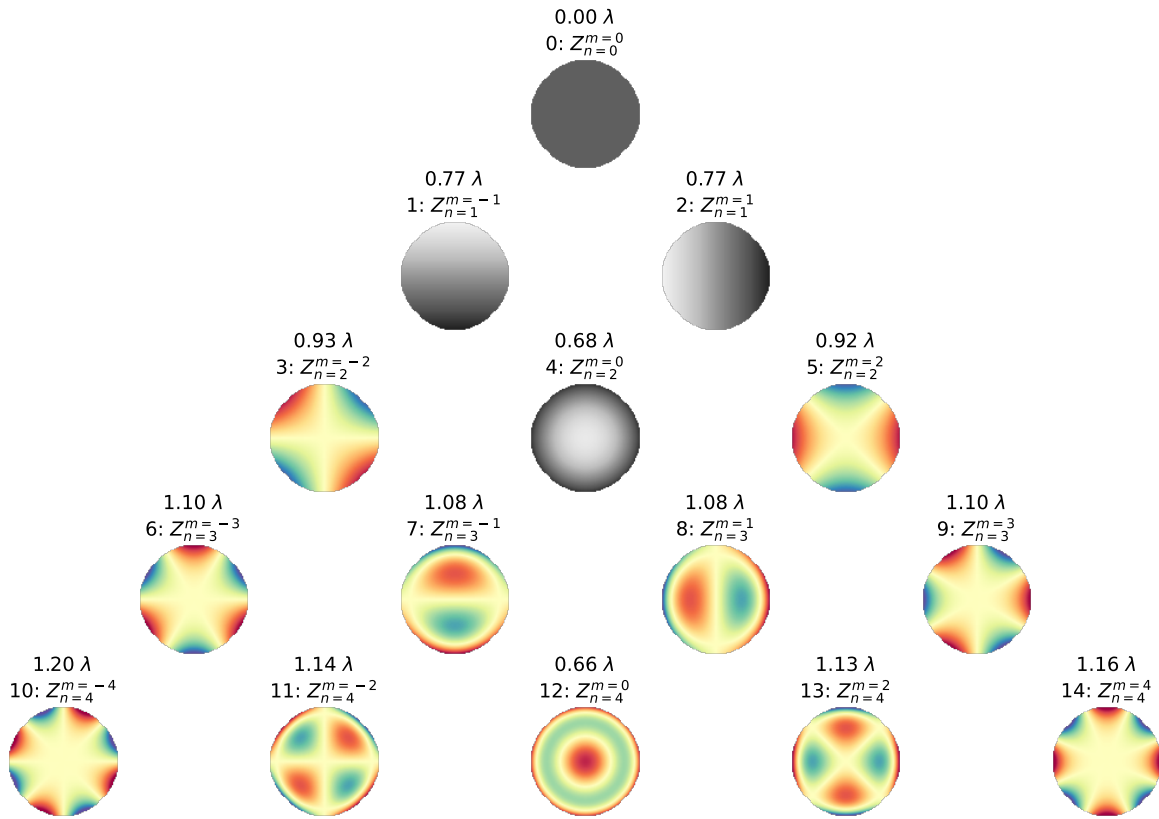


Figure S1: Zernike modes (OSA/ANSI standard indexing). Wavefronts for the first 15 Zernike modes (Z_0^0 through $Z_4^{\pm 4}$) with $0.1\ \mu\text{m}$ RMS applied to each mode. Undetectable modes (bias, tip, tilt, and defocus) are greyed out, and the measured peak-to-valley for each mode is reported in waves for a wavelength $\lambda = 510\text{nm}$.

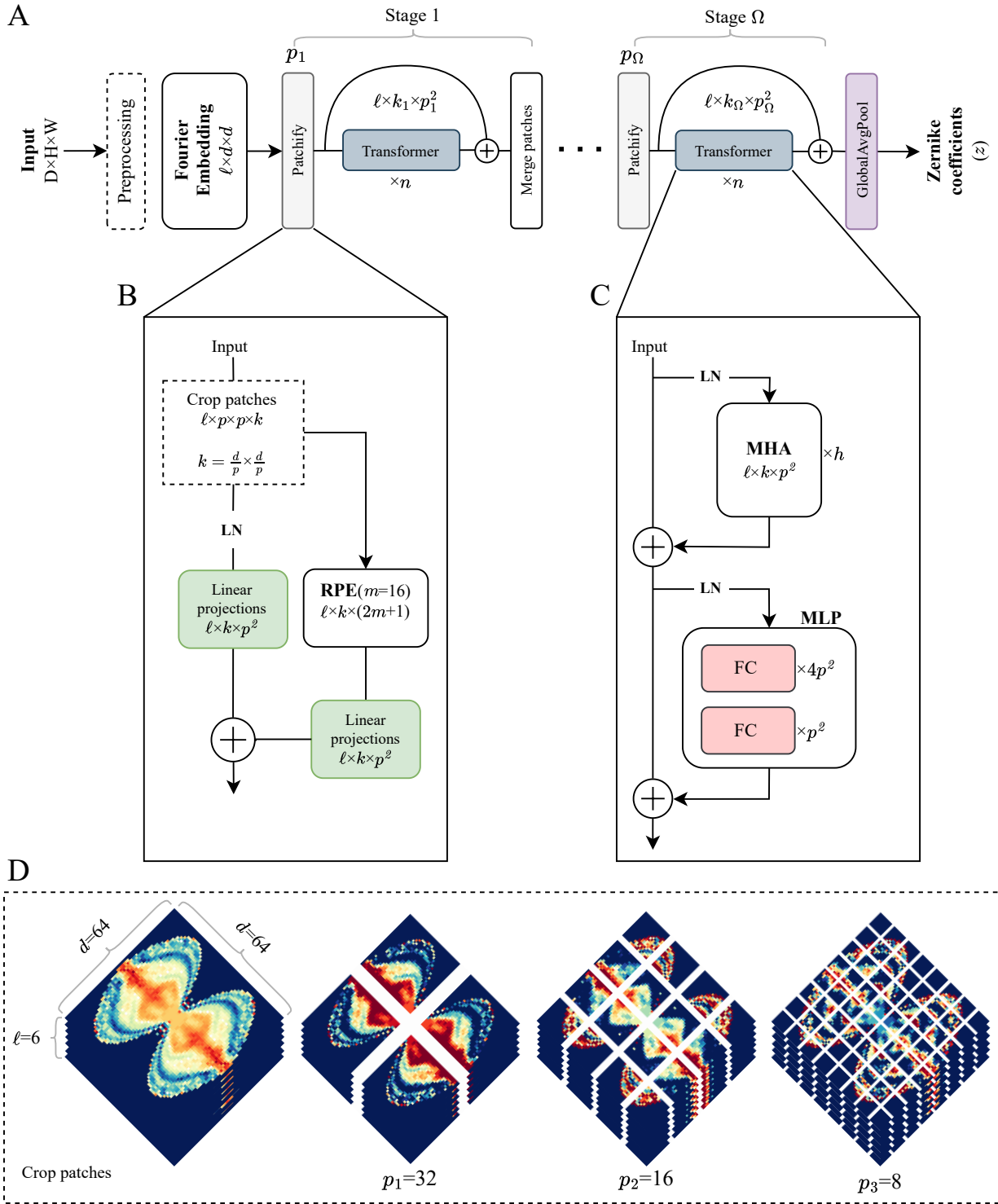


Figure S2: Multistage architecture. A. A schematic of the general form of our model with Ω stages. B. A breakdown of the patchify layer. C. A breakdown of the transformer layer. D. An example output of the crop patches block using a patch size of 32, 16, and 8, respectively.

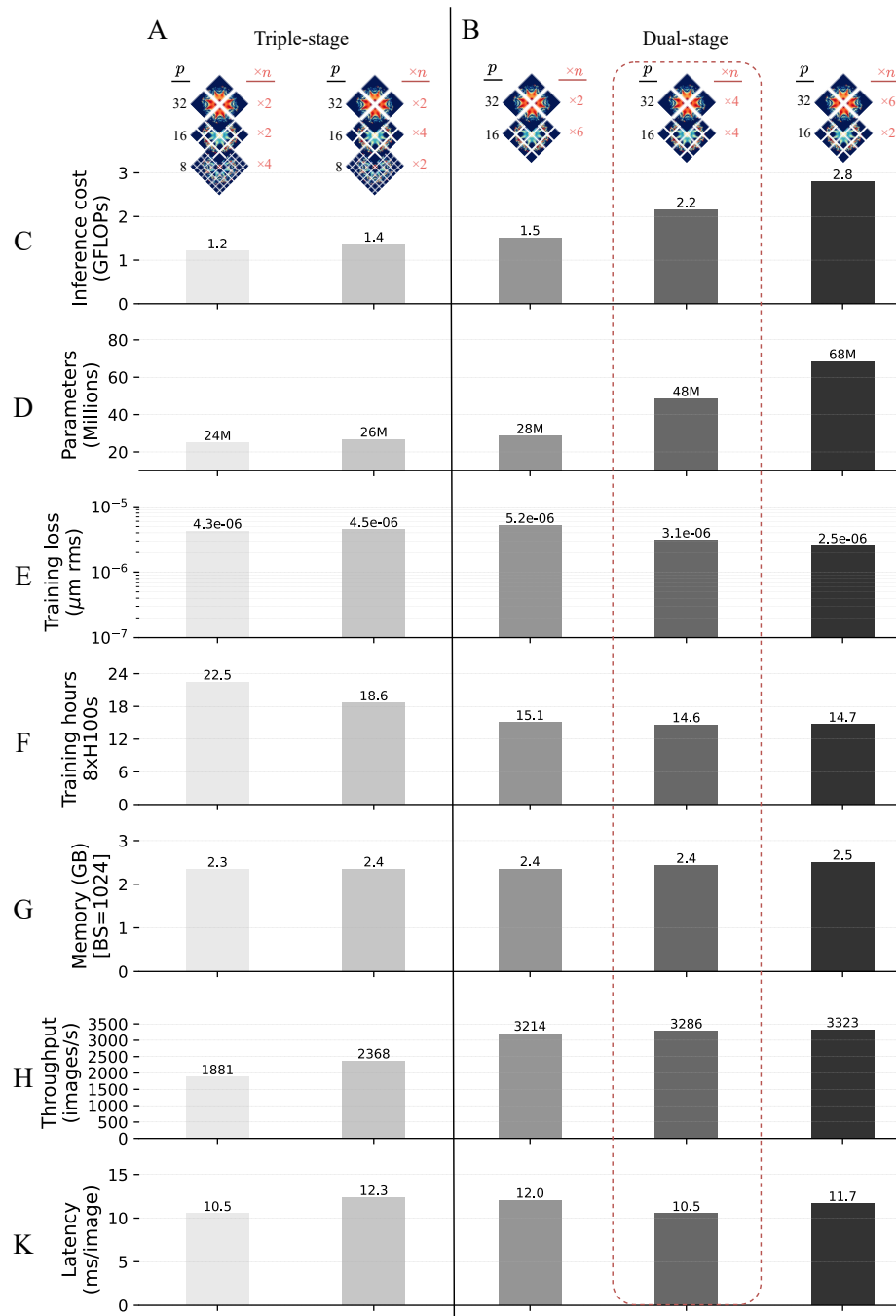


Figure S3: Performance analysis of our multistage design using a total of $n = 8$ transformer layers, and several patch sizes $p_1 = 32$, $p_2 = 16$, and $p_3 = 8$. **A.** Triple-stage design with a patch size of 32, 16, and 8 respectively. **B.** Dual-stage design with a patch size of 32 and 16. **C.** Inference cost per image measured in GFLOPs (10^9 FLOPs). **D.** Total number of trainable parameters. **E.** Training loss using a dataset of 2M synthetically generated samples. **F.** Training time using a single node with eight H100 GPUs. **G.** Memory footprint of each model with a batch of 1024 images using 16-bit floating point precision. **H.** Throughput (average number of predictions/images per second) using a batch size of 1024 on a single A100 GPU. **K.** Latency (average inference time per image) measured in milliseconds for a batch of 1024 examples using a single A100 GPU.

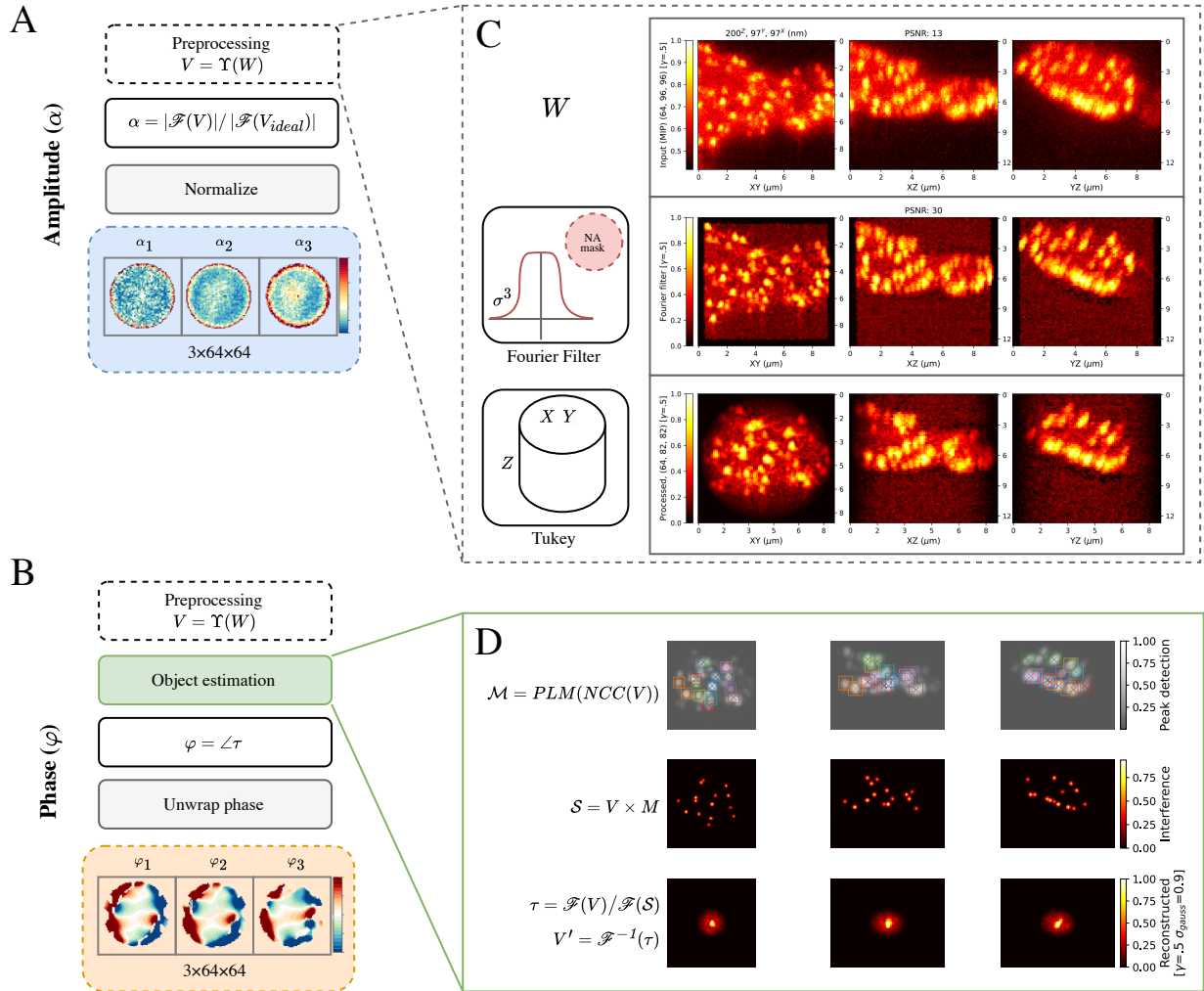


Figure S4: Conversion of raw image volumes to Fourier embeddings. The raw volume is first frequency filtered (Fourier Filter) and windowed (Tukey window, $\hat{x}\hat{y}$ only). The 3D FFT of the result is input into the Amplitude (α) and Phase (φ) Fourier Embedding calculations. **A.** A breakdown of the steps needed to create the amplitude embedding (α). **B.** A breakdown of the steps needed to create the phase embedding (φ). **C.** MIPs from a zebrafish embryo covering $9.3 \times 9.3 \times 12.8 \mu\text{m}^3$ FOV to illustrate the preprocessing modules we use to reduce noise and suppress edge artifacts. **D.** MIPs of the same FOV showing the intermediate steps to remove the interference patterns from the given volume.

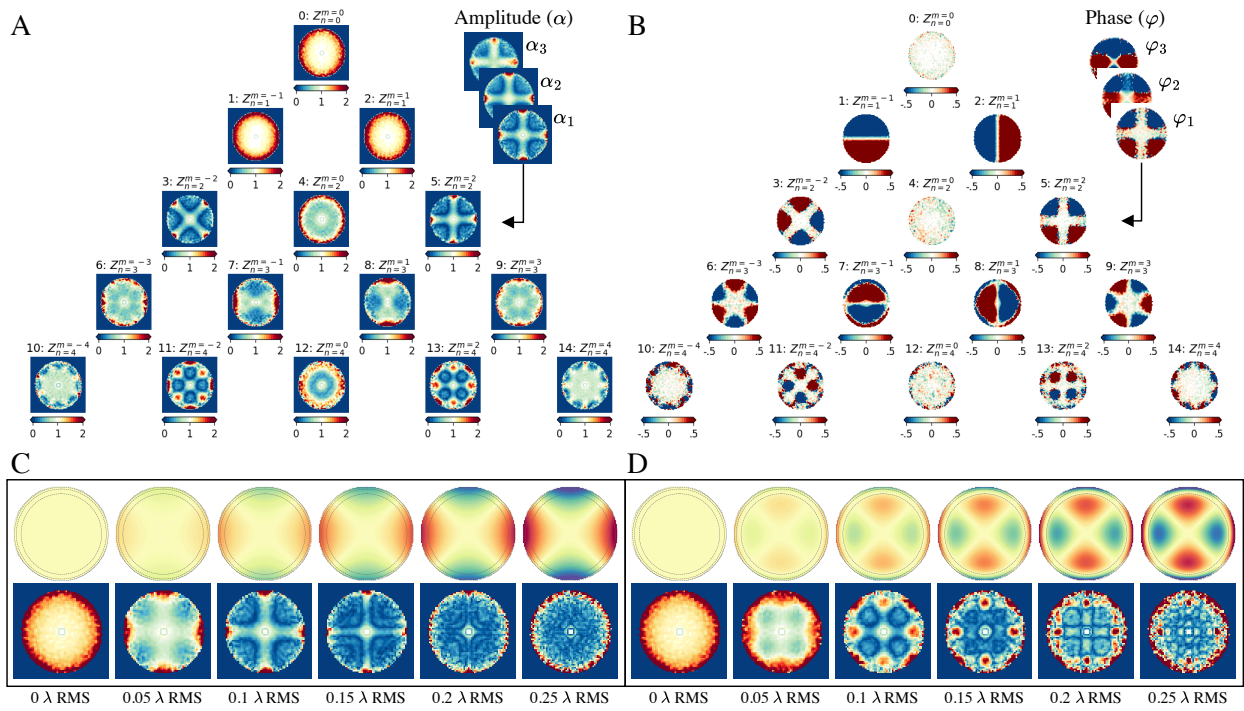


Figure S5: Aberration fingerprints. The principal Fourier plane of (A) amplitude (α_1) and (B) phase (φ_1) embeddings for the first 15 Zernike modes (Z_0^0 through Z_4^4) each at 0.1 λ RMS, shown for an ideal noise-free volume containing a single point emitter. The wavefronts and corresponding amplitude embeddings (α_1) for (C) Z_2^2 and (D) Z_4^2 as aberration magnitudes increase from 0 to 0.25 λ RMS.

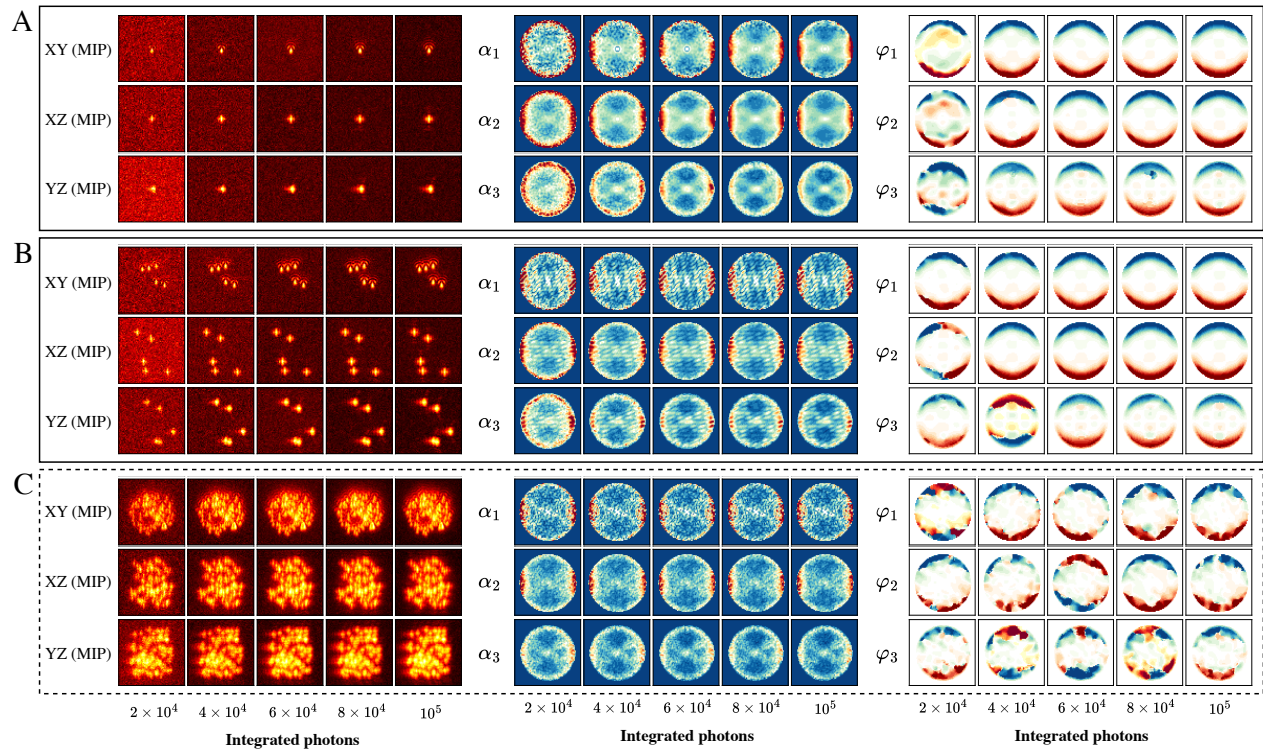


Figure S6: Generalized representations via Fourier embedding. Real-space (left) versus Fourier amplitude (middle) and phase (right) embeddings ($\alpha_1, \alpha_2, \alpha_3, \varphi_1, \varphi_2, \varphi_3$) for a $9.3 \times 9.3 \times 12.8 \mu\text{m}^3$ volume. An aberration of 0.1λ RMS in mode Z_3^{-1} is applied to volumes containing (A) a single bead, (B) five beads, and (C) one hundred beads.

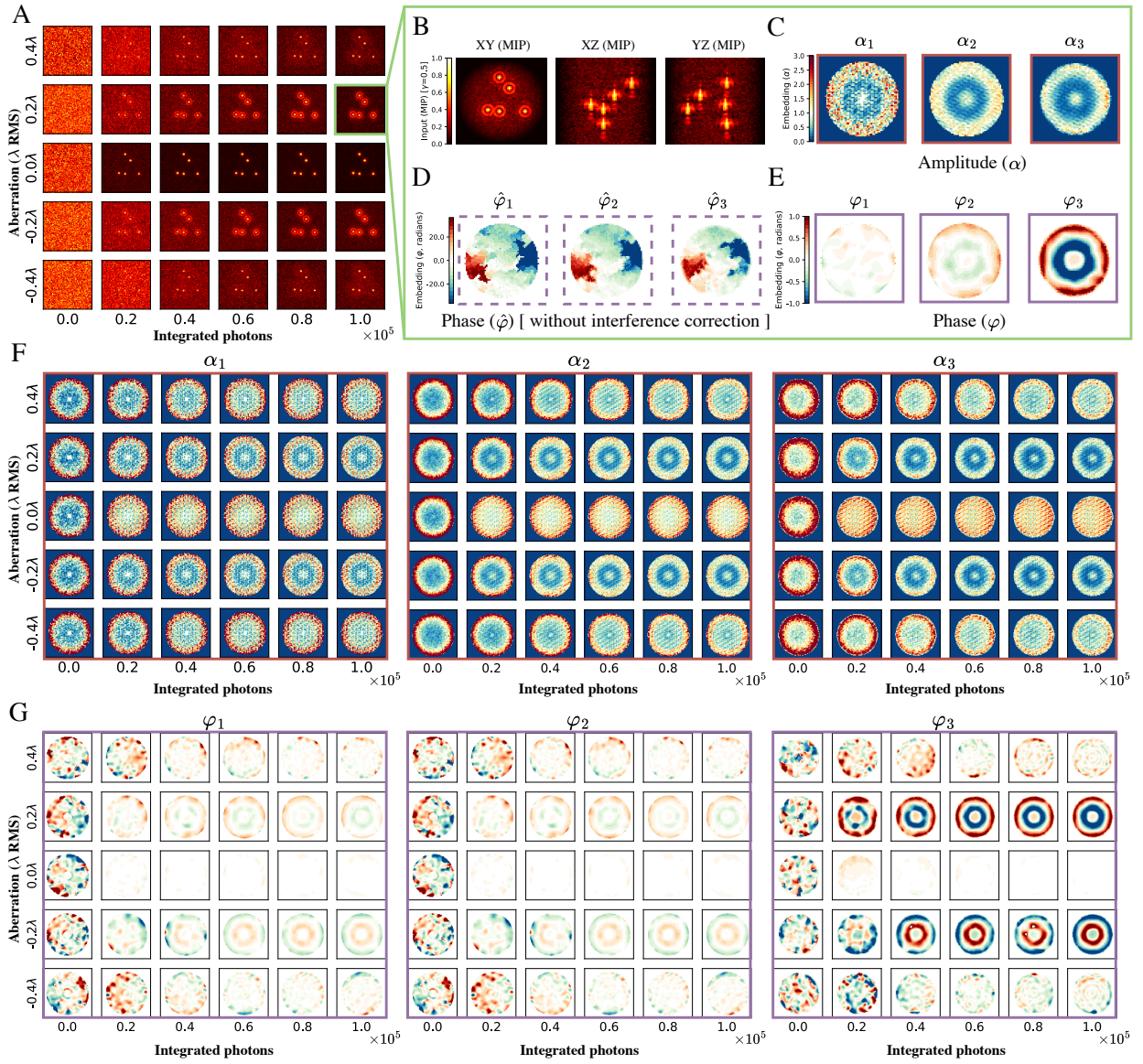


Figure S7: Fourier embedding composition. A. XY MIPs of five synthetic beads, each with an initial aberration ranging from -0.2λ RMS to 0.2λ RMS in mode $[Z_{n=4}^{m=0}]$ at different SNR levels. B. XY, XZ, and YZ MIPs of a single FOV simulated with 10^5 photons. C. Amplitude embedding ($\alpha_1, \alpha_2, \alpha_3$) for the FOV in B. D. Phase embedding ($\varphi_1, \varphi_2, \varphi_3$) for the same FOV in B, shown without interference correction. E. Phase embedding after after removing bead-induced interference patterns. F. Amplitude embeddings for all examples shown in A. G. Phase embeddings for all examples shown in A.

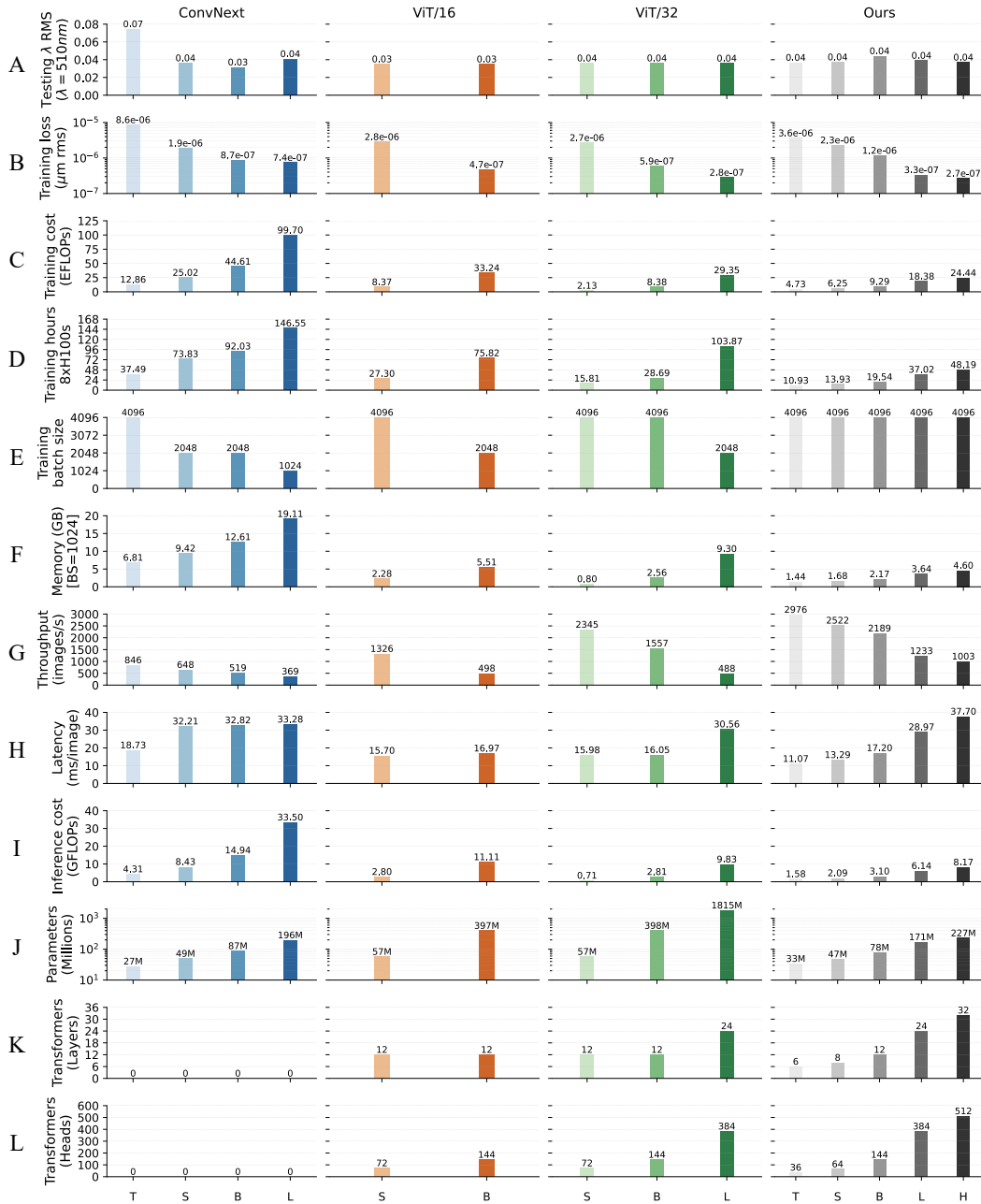


Figure S8: Comparison of the current state-of-the-art architectures applied to 3D aberration sensing across cost indicators of model efficiency. **A.** Median λ RMS residuals over 10K test samples after one correction for aberrations ranging between 0.1λ to 0.2λ simulated with 50K and up to 200K integrated-photons. **B.** Training loss over a dataset consisting of 2M synthetically generated samples. **C.** Training cost measured in exaFLOPs (10^{18} FLOPs) for 500 epochs of training. **D.** Training time using eight H100 GPUs. **E.** Optimal batch size used for training based on memory usage for each model. **F.** Memory footprint of each model with a batch of 1024 images using 16-bit floating point precision. **G.** Max number of predictions per second using a batch size of 1024 on a single A100 GPU. **H.** Average inference time (milliseconds) per image for a batch of 1024 examples using a single A100 GPU. **I.** Inference cost per image measured in gigaFLOPs (10^9 FLOPs). **J.** Total number of trainable parameters. **K.** Total number of transformer layers (not applicable for ConvNeXt models). **L.** Total number of heads in all transformer layers (not applicable for ConvNeXt models). Lower numbers are better for all cost indicators, except for E, G, K, and L.

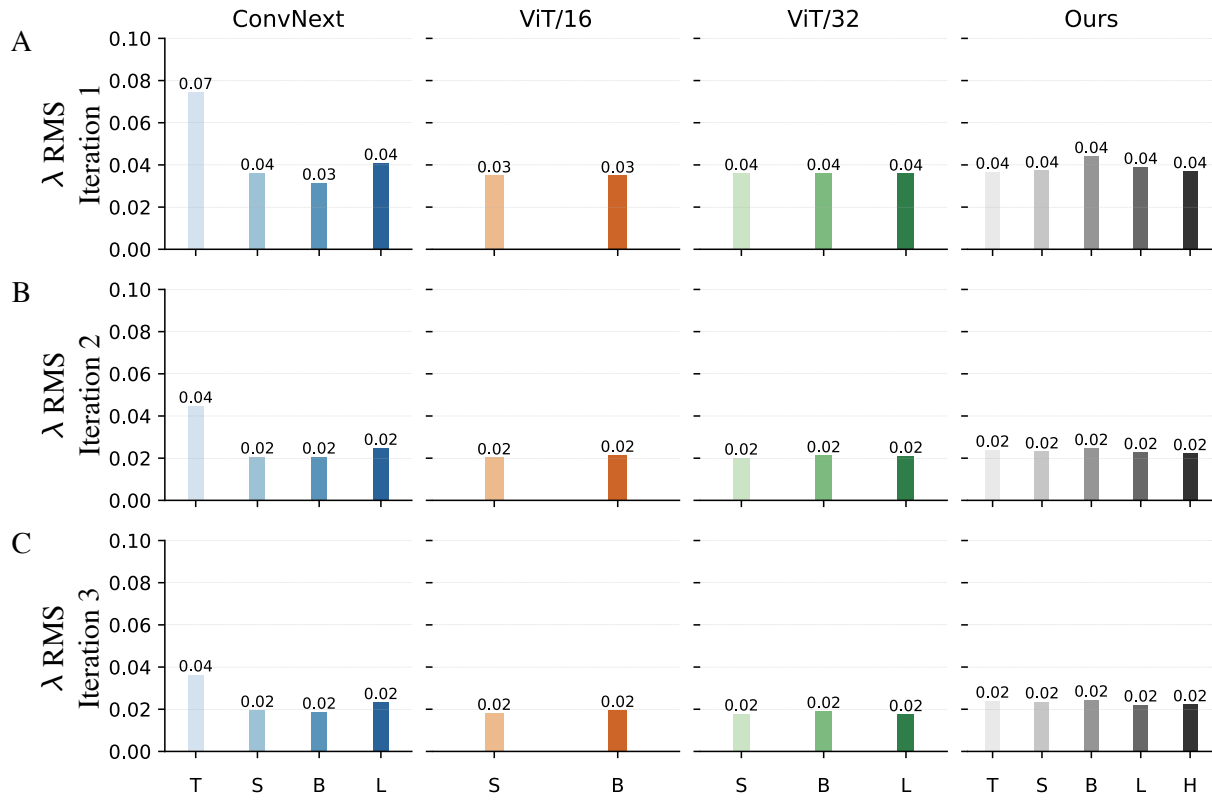


Figure S9: Median λ RMS residuals over 10K test samples with aberrations ranging between 0.2λ RMS to 0.4λ RMS, simulated with 50K and up to 200K integrated-photons. A. First iteration. B. Second iteration. C. Third iteration.

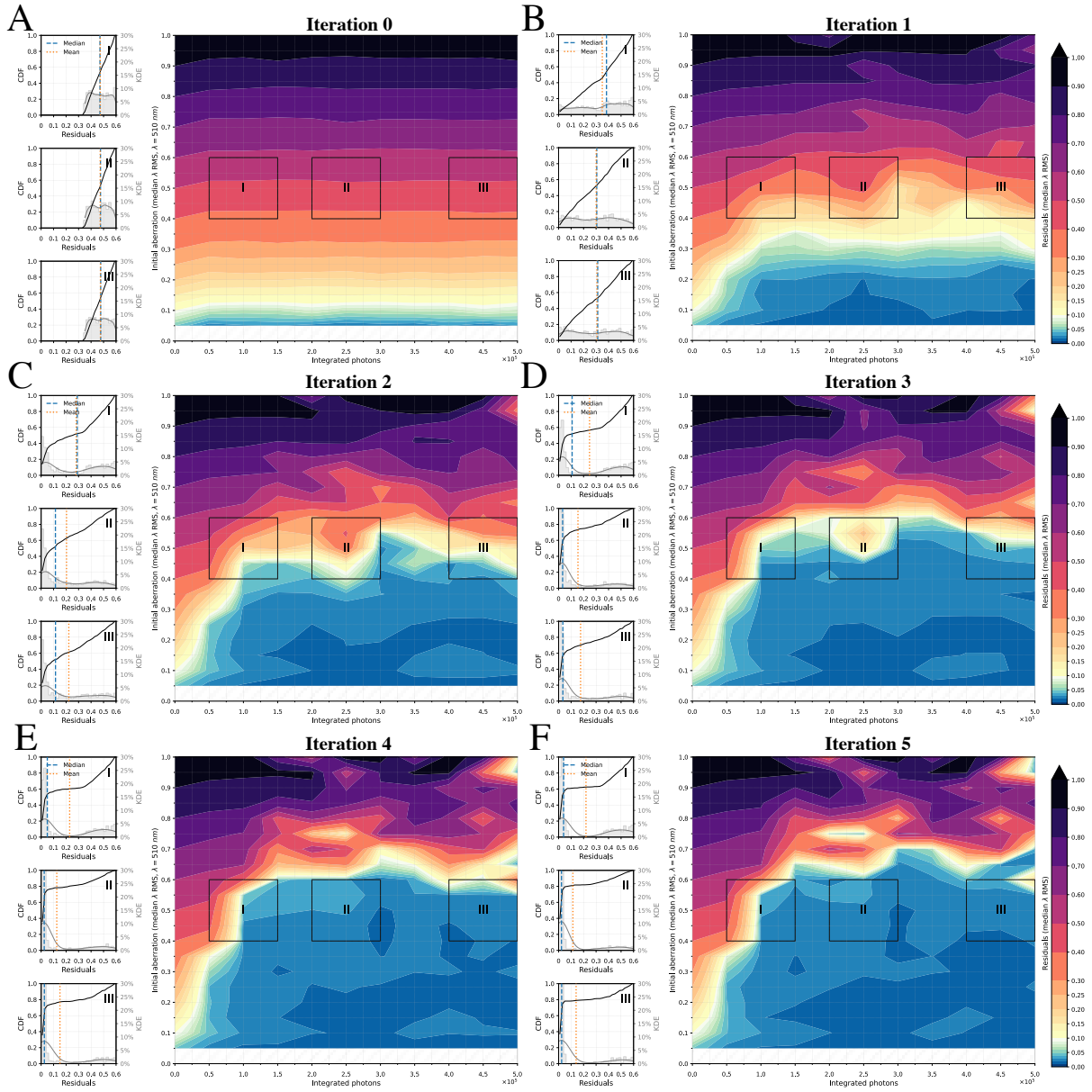


Figure S10: Sensitivity to SNR. Evaluation of our Small model (S) using simulated data of a single bead. **A.** The initial RMS distribution of test dataset as a function of SNR without AO. **B–F.** Residual λ RMS with five rounds of AO corrections.

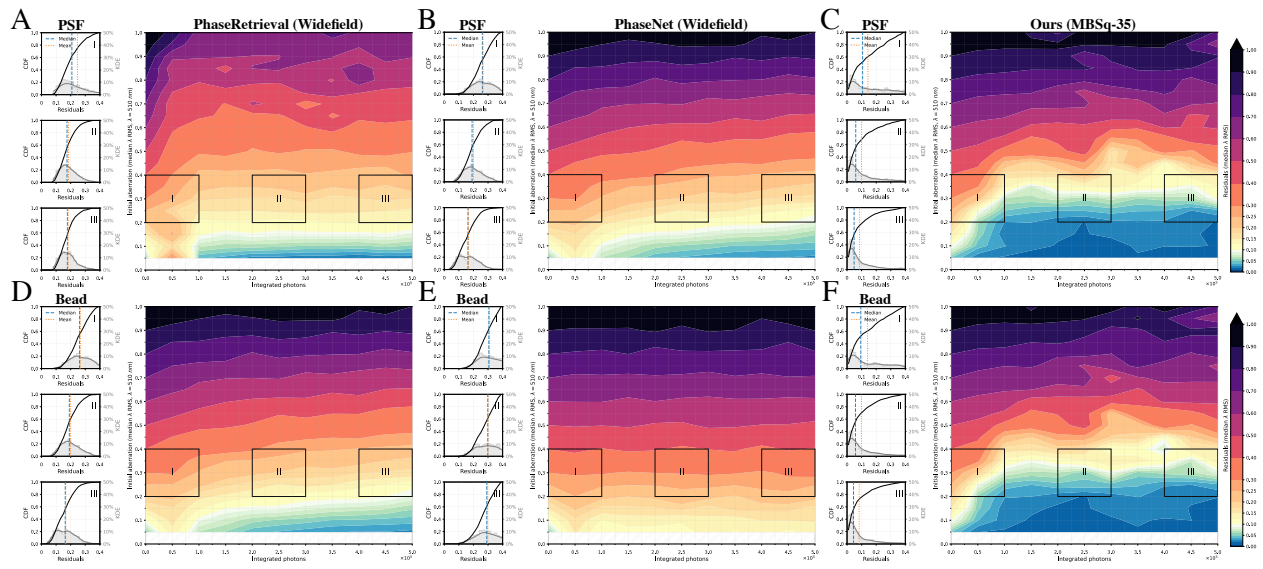


Figure S11: Singleshot evaluation of phase retrieval using 10K synthetic PSFs. A–C. Residual λ RMS for centered bead using PhaseRetrieval, PhaseNet, and our model, respectively. D–F. Residual λ RMS for a non-centered bead using the three methods mentioned above.

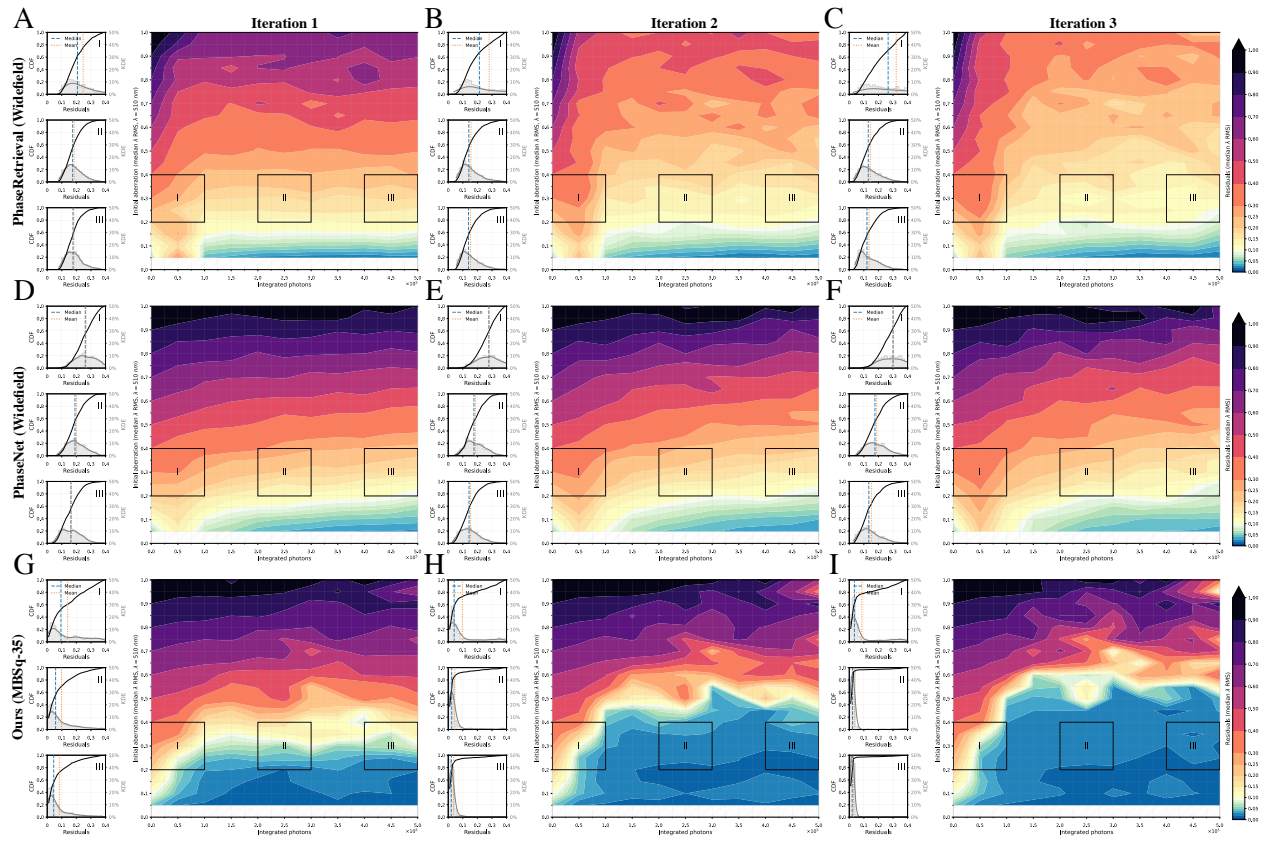


Figure S12: Iterative evaluation of phase retrieval using 10K synthetic PSFs. A–C. Residual λ RMS for widefield PSFs using PhaseRetrieval. D–F. Residual λ RMS for widefield PSFs using PhaseNet. G–I. Residual λ RMS for YuMB LLS PSFs using our Small model (S).

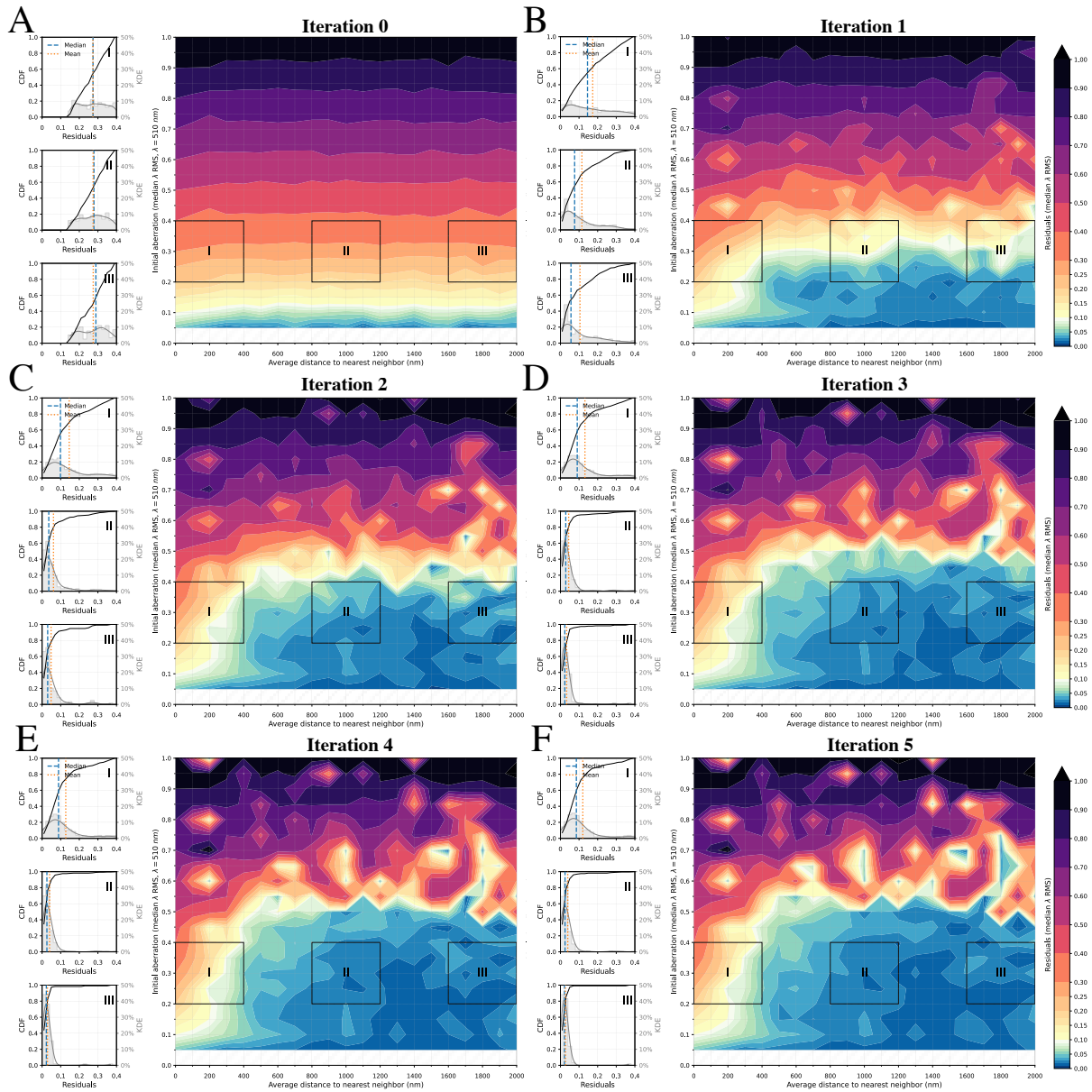


Figure S13: Sensitivity to the density of objects. Evaluation of our Small model (S) using simulated data with up to 150 beads in any given test sample. **A.** The initial RMS distribution of test dataset as a function of the average distance to the nearest neighbor (bead) without AO. **B-F.** Residual λ RMS with five rounds of AO corrections.

Fourier-Based 3D Multistage Transformer for Aberration Correction in Multicellular Specimens

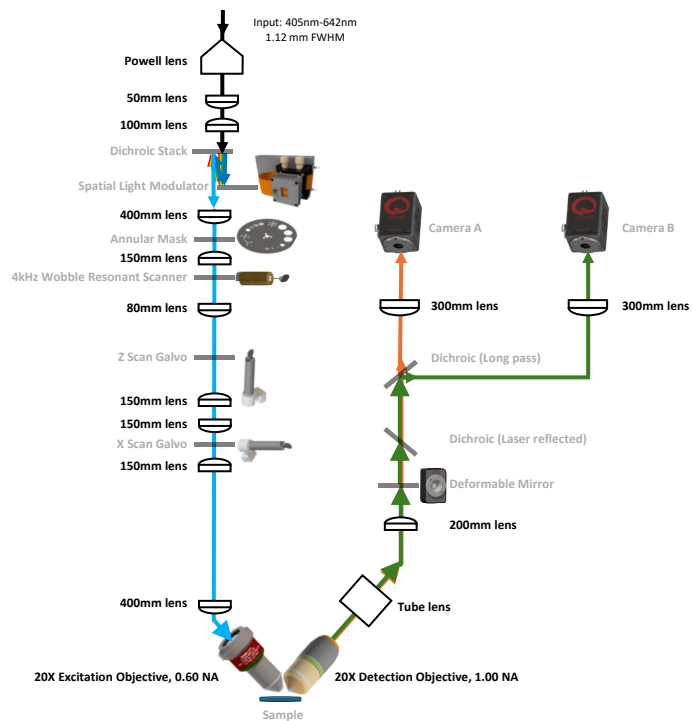


Figure S14: Schematic of AO-LLS microscope used for all experiments.

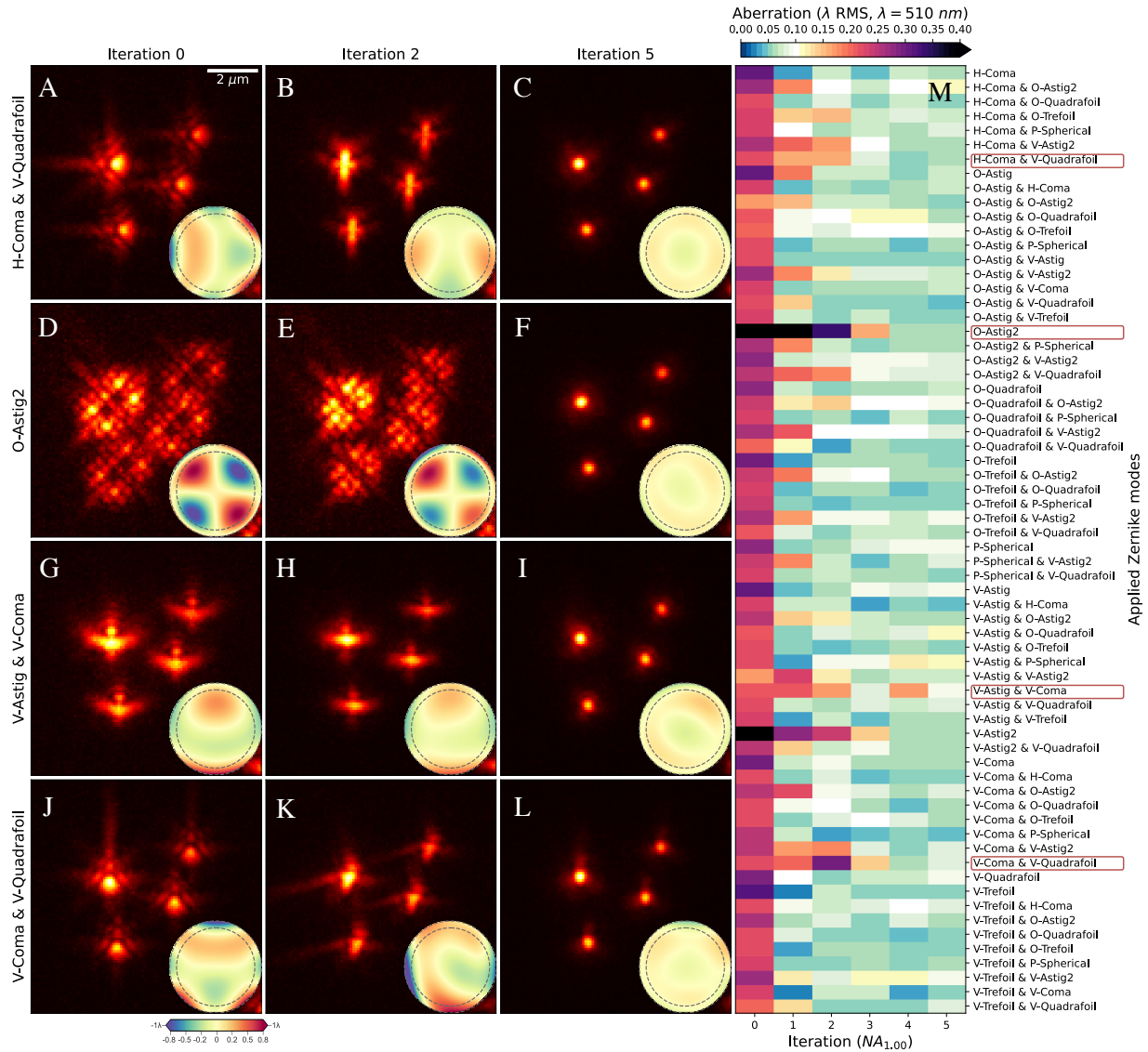


Figure S15: Correction of beads with initial artificial aberrations. Four examples, H-Coma & V-Quadrafoil ($Z_{n=3}^{m=1} + Z_{n=4}^{m=4}$), O-Astig2 ($Z_{n=4}^{m=2}$), V-Astig & V-Coma ($Z_{n=2}^{m=2} + Z_{n=3}^{m=-1}$), V-Coma & V-Quadrafoil ($Z_{n=3}^{m=-1} + Z_{n=4}^{m=4}$), where the initial aberration is artificially applied by the DM. *Iteration 0* shows XY maximum projection of four beads with initial aberration imaged using ILLS, upon which AOVIFT makes predictions. *Iteration 2* shows the resulting field of beads after applying AOVIFT prediction to the DM. *Iteration 5* shows the results after applying the AOVIFT prediction measured from *Iteration 4*. Insets show the AOVIFT predicted wavefront over the NA = 1.0 pupil with a dashed line at NA = 0.85 M. Heatmap of the residual aberration (as measured via phase retrieval on a well isolated bead) after application of AOVIFT predictions starting with a single Zernike mode up to Mode 14 ($Z_{n=4}^{m=4}$) for up to 5 iterations.

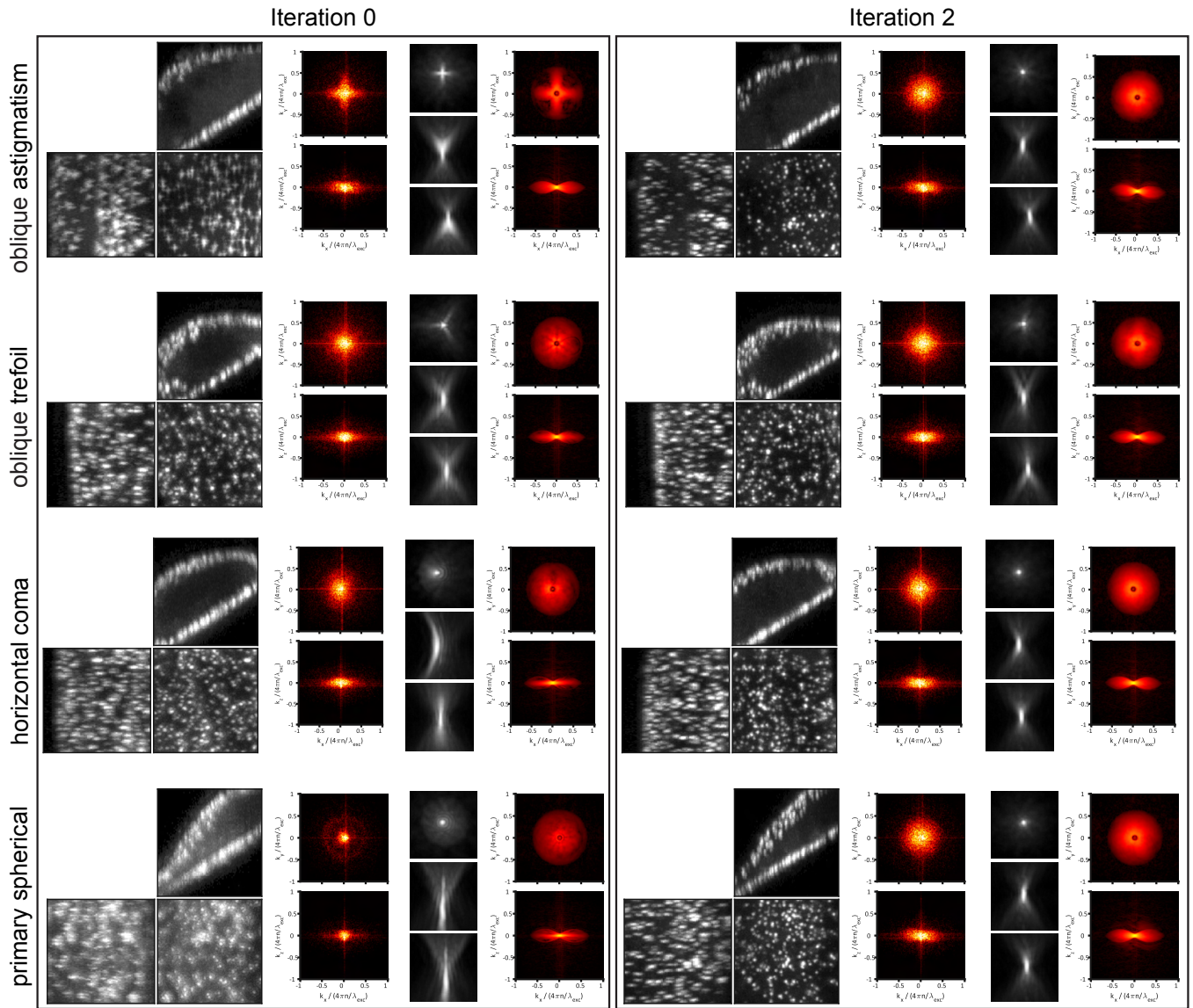


Figure S16: Experimental evaluation of AOVIFT on live SUM159 AP2 cells under single mode aberrations. Four different single-mode aberrations (top to bottom) were introduced via the microscope DM to test AOVIFT performance on live cells. Left panels show XY, XZ, YZ MIPs of a center-cropped region of cells; middle panels show the corresponding FFT of the cell volumes; and right panels show the widefield PSF and OTF MIPs. Each box depicts the cells, cell volume FFTs, and widefield PSF/ OTF pairs with applied single mode aberrations (Iteration 0), and after two rounds of iterative AOVIFT correction (Iteration 2).

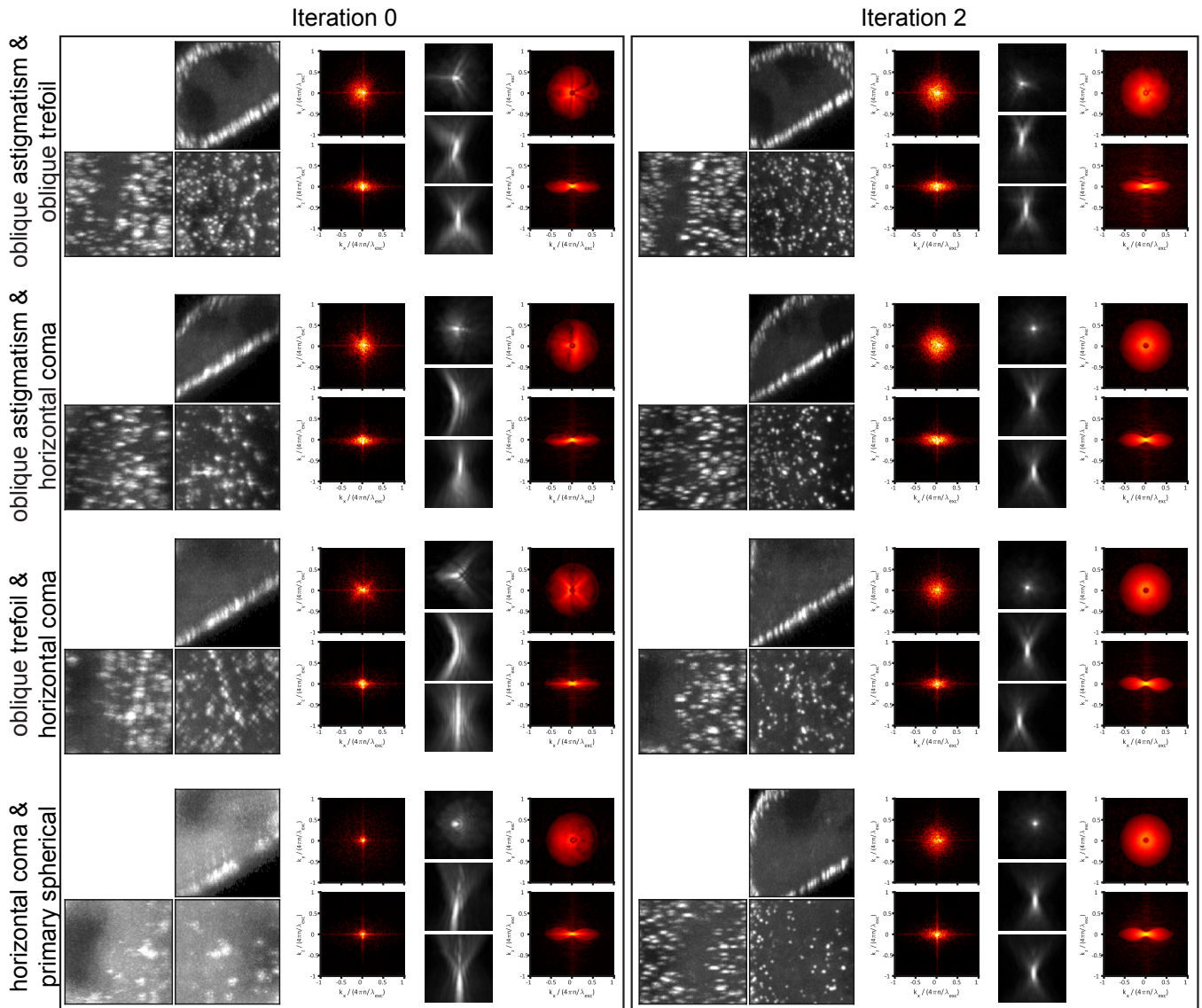


Figure S17: Experimental evaluation of AOVIFT on live SUM159 AP2 cells under multiple mode aberrations. Four different two-mode aberration (top to bottom) were introduced via the microscope DM to test AOVIFT performance on live cells. Left panels show XY, XZ, YZ MIPs of a center-cropped region of cells; middle panels show the corresponding FFT of the cell volumes; and right panels show the widefield PSF and OTF MIPs. Each box depicts the cells, cell volume FFTs, and widefield PSF/ OTF pairs with applied single mode aberrations (Iteration 0), and after two rounds of iterative AOVIFT correction (Iteration 2)

Fourier-Based 3D Multistage Transformer for Aberration Correction in Multicellular Specimens

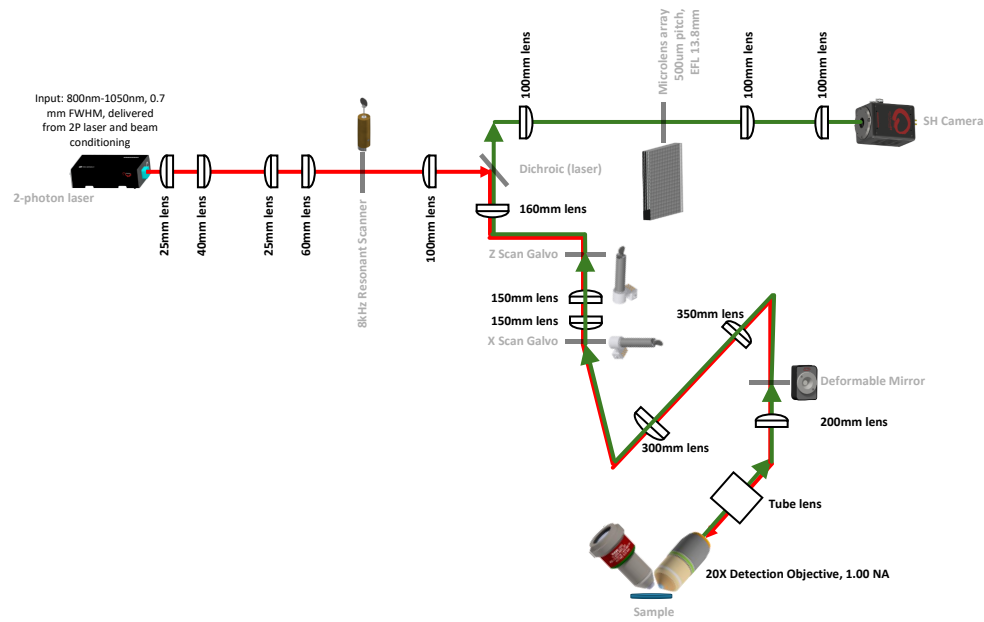


Figure S18: AO-LLS microscope schematic illustrating the Shack-Hartmann wavefront detection mode. Lenses are in 4f configuration. The X Scan Galvo, Z Scan Galvo, Annular Mask, and Deformable Mirror (DM) are at pupil conjugate planes. The Spatial Light Modulator (SLM), 4kHz wobble resonant scanner, and cameras are all at sample conjugate planes.

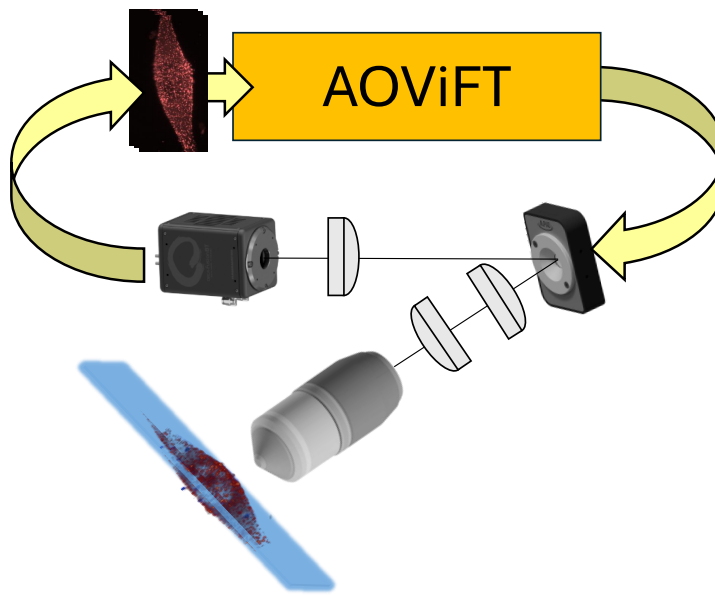


Figure S19: AOVIFT closed loop operation. Light-sheet excitation (blue), illuminates the focal plane of the detection objective causing emission from fluorescent markers (red) in the specimen. This emitted light is collected by the detection objective, relayed to a deformable mirror, and recorded by a camera. The acquired image stack is fed into AOVIFT which produces an update for the deformable mirror shape.

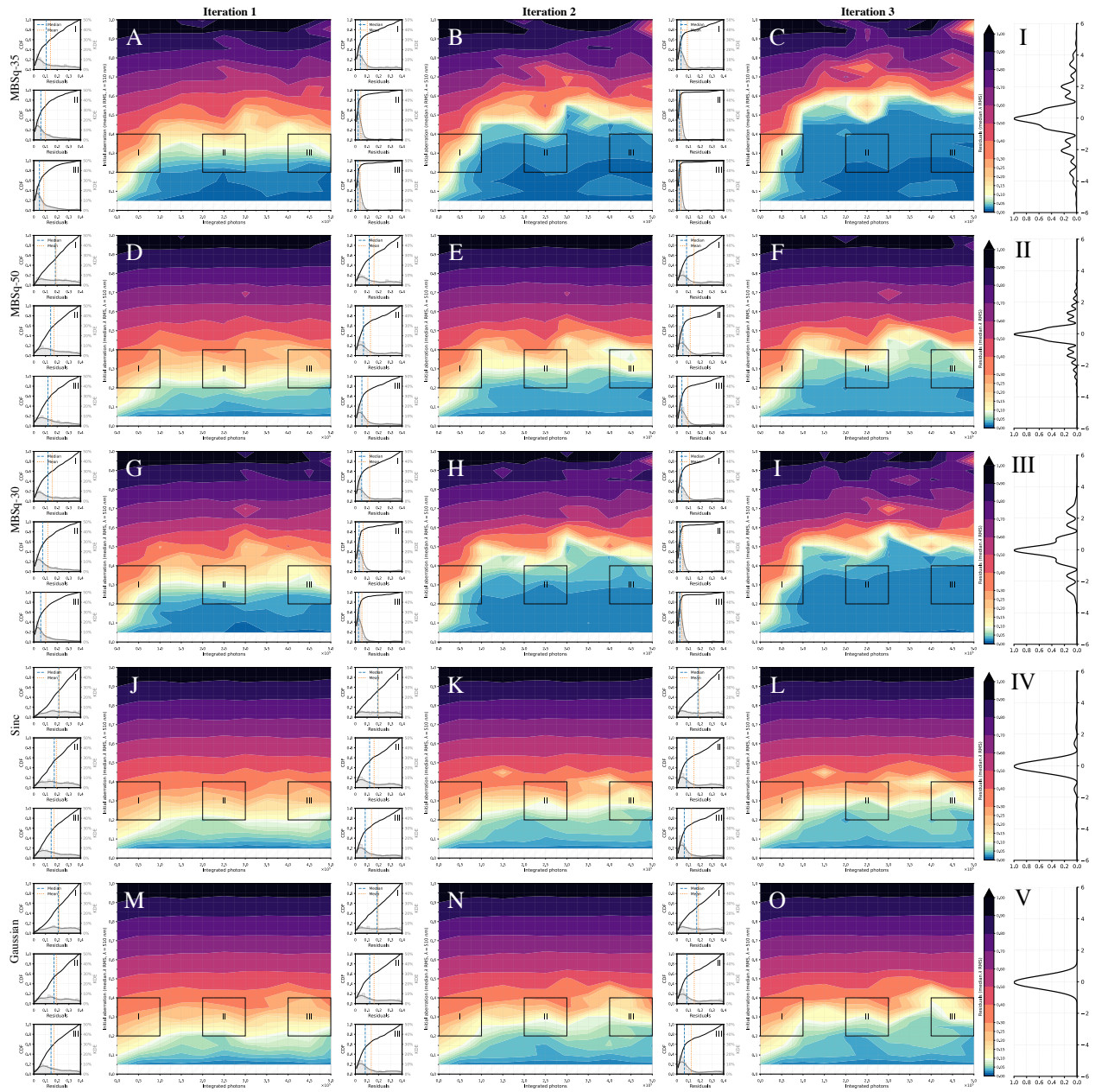


Figure S20: Evaluation of our Small model (S) using several different light sheet types over 10K synthetic samples of a single bead with aberrations up to 1.0λ RMS. A–C. MBSq-35 (the original LLS profile we used to simulate the training data). D–F. MBSq-50. G–I. MBSq-30. J–L. Sinc light sheet simulated by swept lateral standing wave. M–O. Gaussian light sheet. I–V. Excitation profiles. See Supplementary Table S6 for more details about the light sheets used for this test.

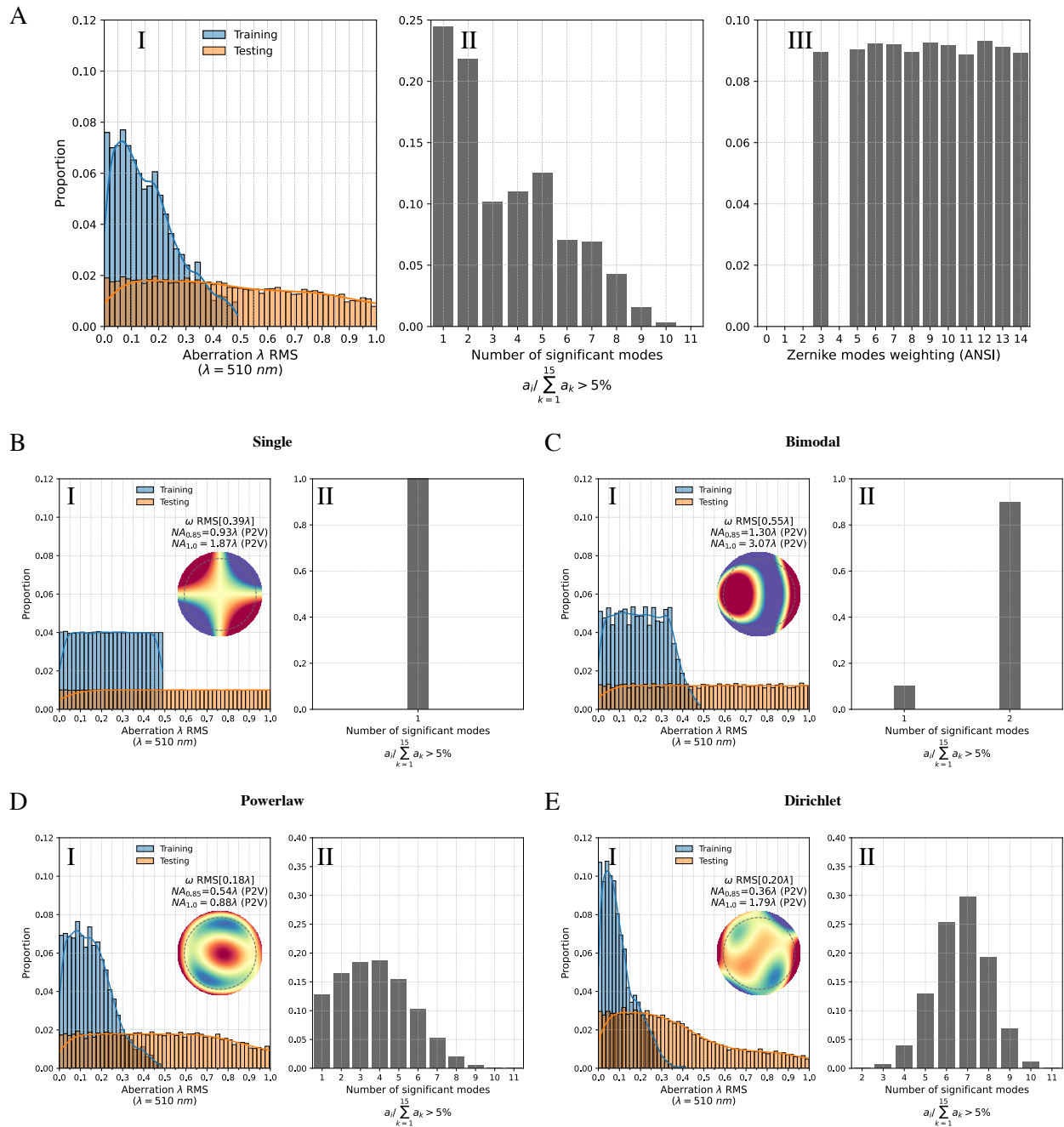


Figure S21: Zernike distributions. A. Statistics for the overall training and testing with four different mode distributions: single, bimodal, powerlaw, and Dirichlet. **A(I)**. Magnitude histogram for training (blue), and testing (orange) distributions. **A(II)**. A histogram showing the number of modes that contribute more than 5% of the total aberration for any given wavefront (i.e., dominant modes). **A(III)**. A histogram illustrating the probability of choosing any of the first 15 Zernike modes. **B**. Histograms for the single mode distribution along with example wavefronts. **C**. Same, but for the bimodal distribution. **D**. Same, powerlaw distribution. **E**. Same, dirichlet distribution.

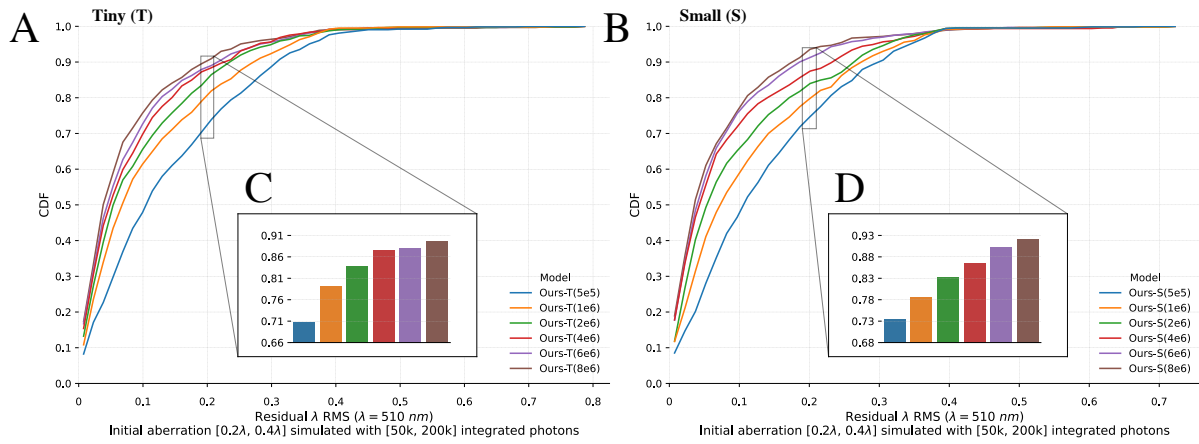


Figure S22: Scaling performance as a function of training dataset size. Residual RMS for a series of models trained with an increasing number of training samples: 500K (blue), 1M (orange), 2M (green), 4M (red), 6M (purple), and 8M (brown). To evaluate our models we show our residuals after a single correction over a test dataset of 10K samples with aberration ranging between 0.2λ RMS and 0.4λ RMS simulated using a single bead with 50K up to 200K integrated photons. **A–B.** Cumulative distribution functions for our *Tiny* model (**A**), and our *Small* model (**B**). **C–D.** Inset plots showing the percentage of data below 0.2λ RMS for each model.

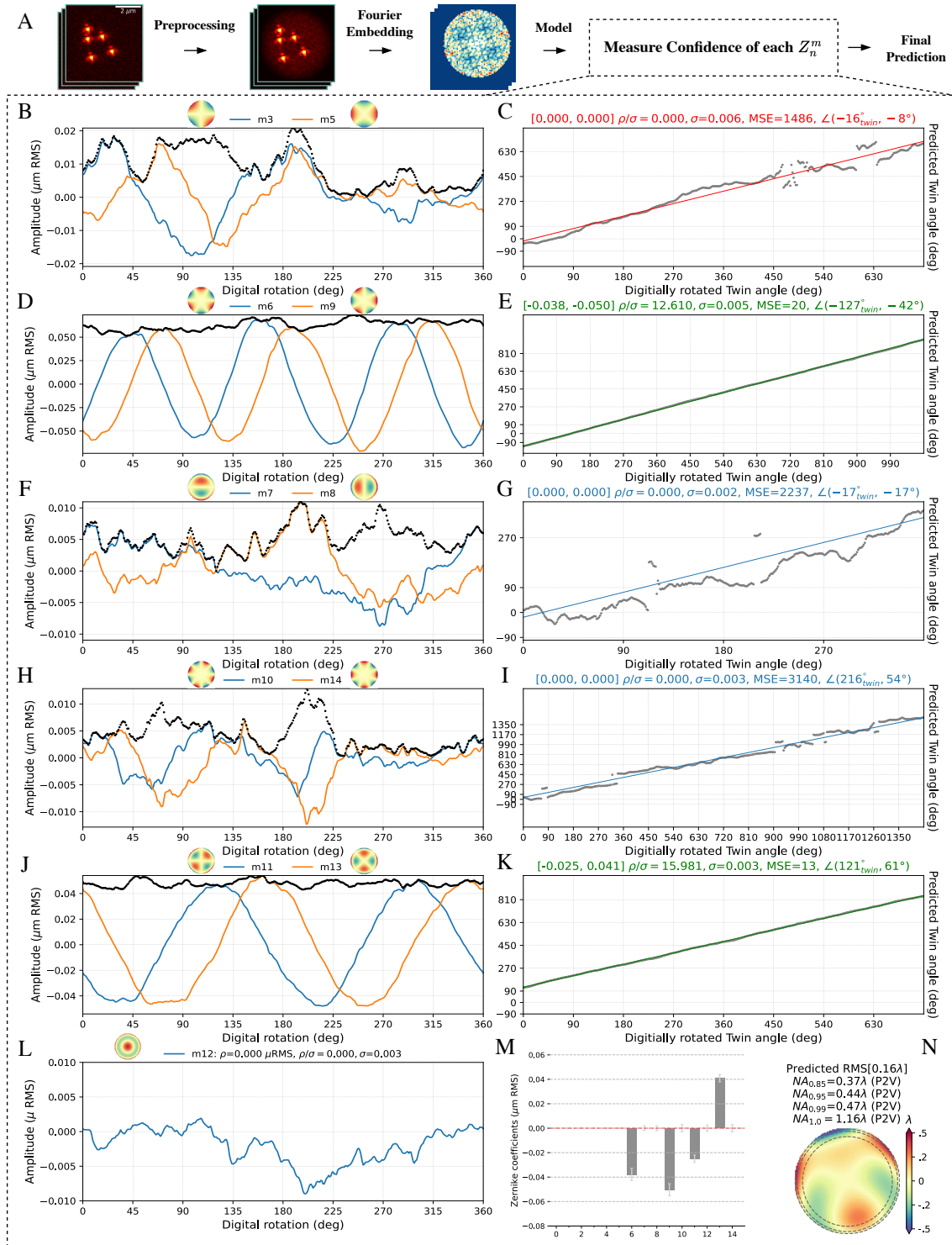


Figure S23: Predictions on rotated embeddings gives measure of confidence. **A.** Schematic of our prediction pipeline. **B.** Predicted amplitudes of astigmatism for each digital rotation: ($Z_{n=2}^{m=-2}$, blue), ($Z_{n=2}^{m=2}$, orange), and the magnitude for both twin modes in black. **C.** Regression fit between the digitally rotated angle and the predicted twin angle for astigmatism. **D–E.** Trefoil. **F–G.** Coma. **H–I.** Quadrafoil. **J–K.** Secondary astigmatism. **L.** Predicted amplitudes of primary spherical for each digital rotation. **M.** Final prediction for each Zernike mode. **N.** Predicted wavefront.

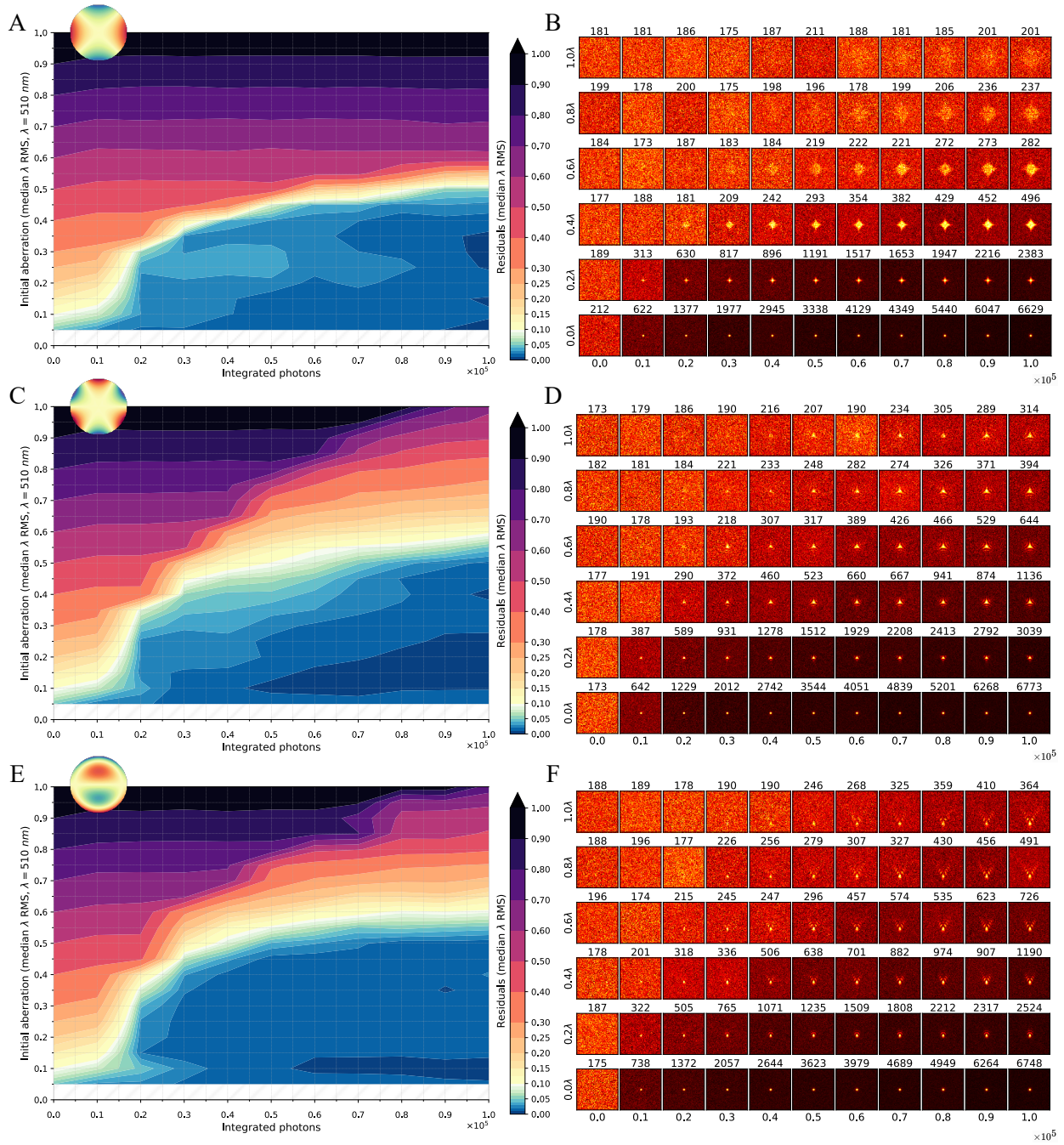


Figure S24: Single mode evaluation (I). A. Residual λ RMS after a single correction using our Small model (S) for vertical astigmatism $Z_{n=2}^{m=2}$. B. XY MIPs showing the initial aberration without correction for different amplitudes *w.r.t.* SNR, with the max counts highlighted above each PSF. C–D. Vertical trefoil $Z_{n=3}^{m=-3}$. E–F. Vertical coma $Z_{n=3}^{m=-1}$.

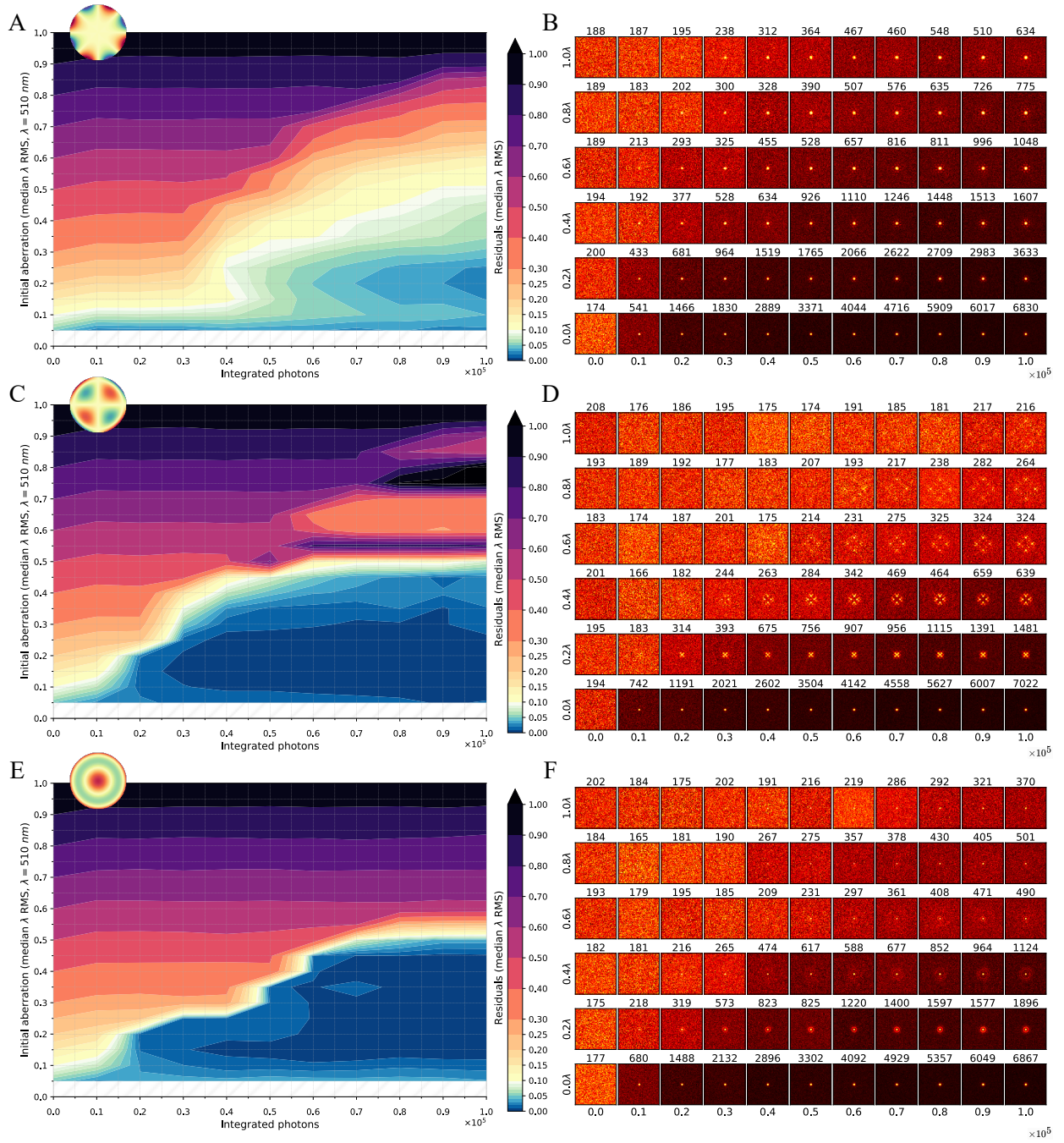


Figure S25: Single mode evaluation (II). A. Residual λ RMS after a single correction using our Small model (S) for oblique quadrafoil $Z_{n=4}^{m=-4}$. B. XY MIPs showing the initial aberration without correction for different amplitudes *w.r.t.* SNR, with the max counts highlighted above each PSF. C–D. Oblique secondary astigmatism $Z_{n=4}^{m=-2}$. E–F. Primary spherical $Z_{n=4}^{m=0}$.

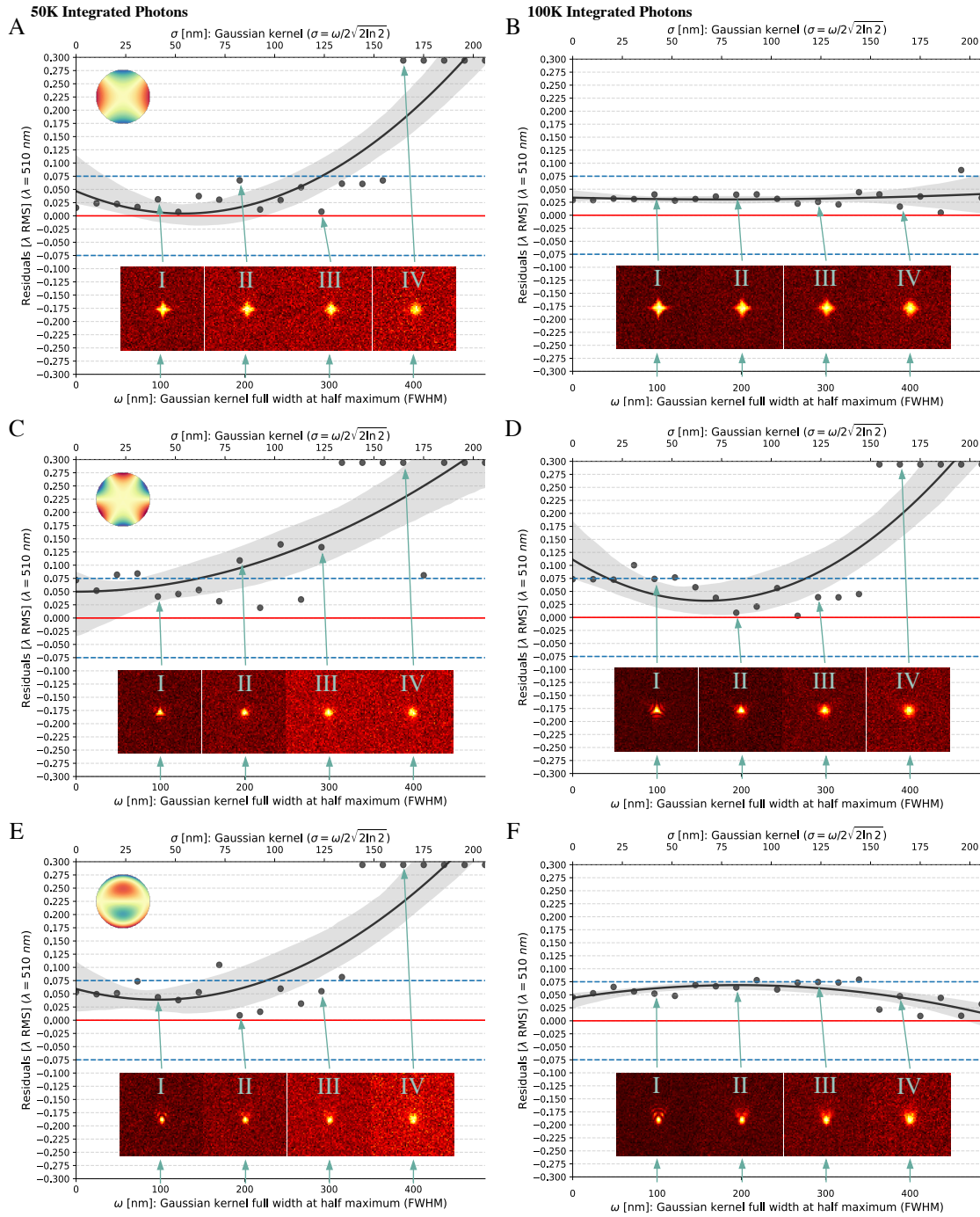


Figure S26: Sensitivity to object size. We use 0.3λ RMS to synthetically generate a single mode aberration, while increasing the size of the Gaussian kernel used to simulate the bead for each sample. **A.** Residual λ RMS after a single correction using our Small model (S) for vertical astigmatism $Z_{n=2}^{m=2}$ simulated with 50K integrated photons. **B.** Residual λ RMS using PSFs simulated with 100K integrated photons. **C–D.** Residual λ RMS for vertical trefoil $Z_{n=3}^{m=3}$. **E–F.** Residual λ RMS for vertical coma $Z_{n=3}^{m=1}$.

Table S1: Comparisons with other ML-based AO methods.

Paper	Speed (time/isoplanatic patch)	Accuracy and Robustness	Noninvasiveness (photobleaching)	Code Available?
[4]	$\leq 1s$.	3D widefield PSFs. (Fig. S11–S12)	No extra imaging.	✓
[5]	$\leq 5s$.	2D data. Samples that are sparse, cleared, fixed, and high SNR.	1 extra (defocused) image.	✗
[6]	$\leq 1s$.	3D data. Single Molecule Light Microscopy data only with small aberration. Kalman filter needed for robustness.	No extra imaging.	✓
[7]	Extra time needed to acquire M more extra images (M=2,4 or 2N, 4N).	2D data. Diverse sample types. Many manually-tuned parameters. Best at 0.15–0.3 λ RMS. Less accurate at 0.1–0.13 λ RMS.	Many extra images and motion correction recommended.	✗
[8]	~5 minutes per isoplanatic patch of 32 megavoxels (200×400×400).	3D data. Local thresholding required to remove hallucinations. Tested with beads and sparse neuronal structures. Aberration up to 0.3 λ RMS. Many manually-tuned parameters.	No extra imaging.	✓
Ours	$\leq 3s$ (Table. S5).	3D data with puncta. Aberration up to 1.0 λ RMS (Appendix C, Fig. S20). Confidence scores (Appendix A.6).	No extra imaging.	✓

Table S2: Hyperparameters for our model variants. A breakdown of the hyperparameters used for each stage i , where p_i is the patch size used to tile in the input tensor, n_i is the number of transformer layers, h_i is the number of heads for each transformer layer, ϵ_i is the embedding size, and x_i is the MLP size. Furthermore, we show the total number of trainable parameters based on the scheme used to derive each variant with the total number of transformer layers used across all stages (n) and the number of heads for each transformer layer (h).

Name	Stage 1					Stage 2					Scheme		Params millions
	Patch p_1	Layers n_1	Heads h_1	EMB ϵ_1	MLP x_1	Patch p_2	Layers n_2	Heads h_2	EMB ϵ_2	MLP x_2	Layers n	Heads h	
Tiny (T)	32	3	6	1024	4096	16	3	6	256	1024	6	6	33.9
Small (S)	32	4	8	1024	4096	16	4	8	256	1024	8	8	47.4
Base (B)	32	6	12	1024	4096	16	6	12	256	1024	12	12	78.3
Large (L)	32	12	16	1024	4096	16	12	16	256	1024	24	16	171.3
Huge (H)	32	16	16	1024	4096	16	16	16	256	1024	32	16	227.9

Table S3: Evaluation benchmark.

		Testing λ RMS (one shot)	RMS (two shot) \downarrow	Loss (μm RMS) \downarrow	Training hours \downarrow	Training EFLOPs \downarrow	Memory (GB) \downarrow	Throughput (img/s) \uparrow	Latency (ms/img) \downarrow	Inference Parameters GFLOPs \downarrow	Parameters (millions) \downarrow
ConvNext	T	0.07	0.04	$85.6e^{-7}$	37.5	12.9	6.8	846	18.7	4.3	27.9
	S	0.04	0.02	$18.8e^{-7}$	73.8	25.0	9.4	648	32.2	8.4	49.6
	B	0.03	0.02	$8.7e^{-7}$	92.0	44.6	12.6	519	32.8	14.9	87.7
	L	0.04	0.02	$7.4e^{-7}$	146.6	99.7	19.1	369	33.3	33.5	196.4
ViT/16	S	0.03	0.02	$28.4e^{-7}$	27.3	8.4	2.3	1326	15.7	2.8	71.2
	B	0.03	0.02	$4.7e^{-7}$	75.8	33.2	5.5	498	17.0	11.1	397.6
ViT/32	S	0.04	0.02	$26.8e^{-7}$	15.8	2.1	0.9	2345	16.0	0.7	71.5
	B	0.04	0.02	$5.9e^{-7}$	28.7	8.4	2.6	1557	16.1	2.8	398.2
	L	0.04	0.02	$2.8e^{-7}$	103.9	29.4	9.3	488	30.6	9.8	1815.0
Ours	T	0.04	0.02	$36.3e^{-7}$	10.9	4.7	1.4	2976	11.1	1.6	33.9
	S	0.04	0.02	$22.9e^{-7}$	13.9	6.3	1.7	2522	13.3	2.1	47.4
	B	0.04	0.02	$11.7e^{-7}$	19.5	9.3	2.2	2189	17.2	3.1	78.3
	L	0.04	0.02	$3.3e^{-7}$	37.0	18.4	3.6	1233	29.0	6.1	171.3
	H	0.04	0.02	$2.7e^{-7}$	48.2	24.4	4.6	1003	37.7	8.2	227.9

Table S4: Residual wavefront measured using phase retrieval with widefield on an isolated bead for Fig. 4.

Iteration	NA	Residual WF λ RMS	Residual WF λ P2V
Fig. 4a			
0	1.00	0.450701	2.940459
0	0.95	0.380205	2.425910
0	0.85	0.292638	1.435171
1	1.00	0.155836	1.032606
1	0.95	0.135578	0.927065
1	0.85	0.096931	0.705702
2	1.00	0.089000	0.479712
2	0.95	0.083749	0.370095
2	0.85	0.077435	0.336847
Fig. 4b			
0	1.00	0.536977	3.053908
0	0.95	0.465103	2.359822
0	0.85	0.425599	1.941650
1	1.00	0.071351	0.459885
1	0.95	0.061207	0.330569
1	0.85	0.054622	0.244614
2	1.00	0.068686	0.459620
2	0.95	0.059220	0.362715
2	0.85	0.048254	0.218788

Table S5: Performance of SH and AOViFT-S running on a single node with either one or four A100 GPUs. Benchmark for three modes of operations: default mode, smart ROI detection mode where a ROI containing diffraction-limited puncta are cropped from a scanned volume, and tiling mode. AOViFT-S measurement is done on the entire 3D volume ($z \times y \times x \mu\text{m}^3$), whereas SH measurement is done on 3 ($y \times x \mu\text{m}^2$) planes. Total time includes initialization and setup time (e.g., loading model onto each GPU), which may take between 5 and 10 seconds but is only needed at the very beginning of an imaging experiment. Since aberration measurement by SH is done serially, the SH [tile] values reported here represent the average measurement time for 288 ROIs based on the SH [default] measurement time for a single ROI. We also show a breakdown of the time needed for preprocessing & embedding, smart ROI detection, and model inference time.

Method	Predictions w/ 361 rotations	Preprocessing Time	ROI Detection Time	Inference Time	Total Time	GPUs (A100)
Beads $12.8 \times 9.3 \times 9.3 \mu\text{m}^3$						
AOViFT-S [default]	1	2s	N/A	3s	8.6s	1
AOViFT-S [default]	361	2s	N/A	3s	9.2s	1
AOViFT-S [default]	361	2s	N/A	9s	16.9s	4
Cells $25.6 \times 15.5 \times 55.9 \mu\text{m}^3$ (ROI = 12.8, 6.2, 6.2 μm^3)						
AOViFT-S [default]	1	3s	N/A	3s	8.9s	1
AOViFT-S [default]	361	3s	N/A	3s	9.3s	1
AOViFT-S [default]	361	3s	N/A	9s	18.1s	4
AOViFT-S [roi-1]	361	3s	3s	9s	25.3s	4
AOViFT-S [roi-10]	3610	6s	9s	15s	40.6s	4
Zebrafish small FOV $12.8 \times 12.4 \times 12.4 \mu\text{m}^3$ (ROI = 12.8, 6.2, 6.2 μm^3)						
SH [default]	1	N/A	N/A	N/A	5.1s	N/A
AOViFT-S [default]	1	3s	N/A	3s	8.8s	1
AOViFT-S [default]	361	3s	N/A	3s	9.2s	1
AOViFT-S [default]	361	3s	N/A	9s	17.0s	4
AOViFT-S [roi-1]	361	3s	3s	9s	23.7s	4
AOViFT-S [roi-10]	3610	6s	9s	15s	38.9s	4
Zebrafish large FOV $12.8 \times 49.7 \times 223.5 \mu\text{m}^3$ (TILE = 12.8, 9.3, 9.3 μm^3)						
SH [tile]	288 tiles	N/A	N/A	N/A	1,468.8s	N/A
AOViFT-S [tile]	103,968 (288 tiles \times 361)	30.6s	N/A	91.4s	139.8s	4

Table S6: Light sheet specifications. *MBSq-35* LLS excitation profile was used for simulating training data.

Name	Lattice type	$\text{NA}_{\text{lattice}}$	NA_{exc}	NA_{sinc}	$\text{NA}_{\text{annulus}}$	σ_{NA}	FWHM	Crop
MBSq-30	Multi-Bessel square LLS	0.30	-	-	0.375/0.225	0.10	48.5	-
MBSq-35	Multi-Bessel square LLS	0.35	-	-	0.40/0.30	0.10	-	-
MBSq-50	Multi-Bessel square LLS	0.50	-	-	0.40/0.30	0.10	-	-
Sinc	Simulated by swept lateral standing wave	-	0.32	0.24	0.40/0.20	-	51.5	-
Gaussian	Simulated by swept lateral standing wave	-	0.21	-	0.40/0.20	0.21	51.0	0.1

Table S7: Imaging configuration. All data was collected using *MBSq-35* light sheet described in Supplementary Table S6.

Figure Scan type	Voxel size (obj x, obj y, obj z)	Volume size [voxels] (obj x, obj y, obj z)	Excitation wavelength	Camera Exposure
Fig. 4 Widefield Scan	97, 97, 100 nm	96, 96, 128	488 nm	50 ms
Fig. 4 Cell Scan	97, 97, 200 nm	160, 576, 128	488 nm, 560 nm	50 ms
Fig. 5a No AO Full Chip Scan	97, 97, 200 nm	2304, 2304, 64	488 nm , 560 nm	50 ms
Fig. 5b No AO Scan 1	97, 97, 200 nm	128, 128, 64	488 nm, 560 nm	50 ms
Fig. 5b DSH 1	0.1, 6.2, 6.3 um	125, 3, 3	920 nm	500 ms
Fig. 5b DSH 2	0.1, 6.2, 6.3 um	125, 3, 3	920 nm	400 ms
Fig. 5b DSH 3	0.1, 6.2, 6.3 um	125, 3, 3	920 nm	400 ms
Fig. 5b SH AO Scan	97, 97, 200 nm	128, 128, 64	488 nm , 560 nm	50 ms
Fig. 5b No AO Scan 2	97, 97, 200 nm	128, 128, 64	488 nm , 560 nm	50 ms
Fig. 5b AOVIFT Iter 1 Scan	97, 97, 200 nm	128, 128, 64	488 nm , 560 nm	50 ms
Fig. 5b AOVIFT Iter 2 Scan	97, 97, 200 nm	128, 128, 64	488 nm , 560 nm	50 ms
Fig. 5c No AO Full Chip Scan	97, 97, 200 nm	2304, 2304, 64	488 nm, 560 nm	50 ms, 50 ms
Fig. 5c No AO Scan 1	97, 97, 200 nm	128, 128, 64	488 nm, 560 nm	50 ms, 50 ms
Fig. 5c DSH 1	0.1, 6.2, 6.3 um	125, 3, 3	920 nm	500 ms
Fig. 5c DSH 2	0.1, 6.2, 6.3 um	125, 3, 3	920 nm	500 ms
Fig. 5c DSH 3	0.1, 6.2, 6.3 um	125, 3, 3	920 nm	500 ms
Fig. 5c SH AO Scan	97, 97, 200 nm	128, 128, 64	488 nm, 560 nm	50 ms, 50 ms
Fig. 5c No AO Scan 2	97, 97, 200 nm	128, 128, 64	488 nm, 560 nm	50 ms, 50 ms
Fig. 5c AOVIFT Iter 1 Scan	97, 97, 200 nm	128, 128, 64	488 nm, 560 nm	50 ms, 50 ms
Fig. 5c AOVIFT Iter 2 Scan	97, 97, 200 nm	128, 128, 64	488 nm, 560 nm	50 ms, 50 ms
Fig. 5c AOVIFT Full Chip Scan	97, 97, 200 nm	2304, 2304, 64	488 nm, 560 nm	50 ms, 50 ms
Fig. 6b AOVIFT Full Chip Scan	97, 97, 200 nm	2304, 2304, 64	488 nm	50 ms
Fig. 6d AOVIFT Full Chip Scan	97, 97, 200 nm	2304, 2304, 64	560 nm	50 ms
Fig. S16–S17 No AO Full Chip Scan	97, 97, 200 nm	2304, 2304, 64	488 nm, 560 nm	50 ms, 50 ms
Fig. S16–S17 No AO Scan 1	97, 97, 200 nm	256, 256, 64	488 nm, 560 nm	50 ms, 50 ms
Fig. S16–S17 DSH 1	0.1, 6.2, 6.2 um	125, 3, 3	920 nm	400 ms
Fig. S16–S17 DSH 2	0.1, 6.2, 6.2 um	125, 3, 3	920 nm	400 ms
Fig. S16–S17 DSH 3	0.1, 6.2, 6.2 um	125, 3, 3	920 nm	400 ms
Fig. S16–S17 SH AO Scan	97, 97, 200 nm	256, 256, 64	488 nm, 560 nm	50 ms, 50 ms
Fig. S16–S17 No AO Scan 2	97, 97, 200 nm	256, 256, 64	488 nm, 560 nm	50 ms, 50 ms
Fig. S16–S17 AOVIFT Iter 1 Scan	97, 97, 200 nm	256, 256, 64	488 nm, 560 nm	50 ms, 50 ms
Fig. S16–S17 AOVIFT Iter 2 Scan	97, 97, 200 nm	256, 256, 64	488 nm, 560 nm	50 ms, 50 ms

Table S8: Training configuration.

Optical configuration	
Lattice type	<i>MBSq-35</i> (Supplementary Table S6)
NA_{exc}	0.35
$NA_{annulus}$	0.4/0.3
$NA_{detection}$	1.0
σ_{NA}	0.10
Refractive index	1.33
Excitation wavelength	488 nm
Detection wavelength (λ)	510 nm
Voxel size	$200^Z, 125^Y, 125^X$ nm
Training Dataset	
Dataset size	2M synthetic samples
Number of beads	$b \in \{1 \rightarrow 5\}$
Bead size	$FWHM \in \{100, 200, 300, 400\}nm$
Mode distribution(s)	$\mathcal{D} \in \{\text{Single, Bimodal, Powerlaw, Dirichlet}\}$
Mode weighting (Z_n^m)	Uniform $n \in \{2 \rightarrow 4\}$ & linear decay $n \in \{4 \rightarrow 10\}$ w.r.t. m
Magnitude range	$a \in \{0 \rightarrow 0.3\}\mu m \iff a \in \{0 \rightarrow 5\}\lambda$
Image size	$64^Z, 64^Y, 64^X$ voxels $\iff 12.8^Z, 8^Y, 8^X \mu m$
Hyperparameters	
Batch size	4096
Loss	MSE
Optimizer	AdamW [43]
Layerwise decay	LAMB [44]
Momentum β_1	0.9
Momentum β_2	0.99
Initial learning rate (LR)	0.0001
Weight decay	0.001
Training schedulers	
Total epochs	500
Warmup epochs	25
Warmup scheduler	Linear
Learning rate decay	Cosine [45]